Numerical Modelling of Multi-Material Interfaces

R. Hill

Supervisor: Dr J. Szmelter

29th November 2010

Abstract

Remapping (conservative interpolation), within arbitrary Lagrangian-Eulerian (ALE) schemes, requires the values of the scalar to be interpolated from one computational mesh to another which has differing geometry. Advection methods are typically utilised for the remapping stage, with fluxes being created by overlapping volumes between adjacent elements.

In the thesis, a second-order, conservative, sign-preserving remapping scheme is developed utilising concepts of the Multidimensional Positive Definite Advection Transport Algorithm (MPDATA). The basic non-oscillatory and non-oscillatory infinite gauge options are derived for remapping in volume co-ordinates. For the first time, an MPDATA based remapping has been successfully implemented into full ALE schemes. Inherent properties of MPDATA are exploited to reduce wall heating errors via the second-order filtering option. The resulting increase in accuracy and symmetry of numerical solutions is demonstrated. For material interfaces, an adaptive mixed cell approach is proposed which takes advantage of the efficient computational stencil of MPDATA. The proposed approach utilises all available data in the calculation of pseudo velocities in MDPATA in order to retain second-order accuracy and multidimensionality at material interfaces. The effectiveness of the adaptive mixed cell approach is highlighted via examples featuring artificial material interfaces.

Theoretical developments are supported by numerical testing. All test cases compare the accuracy of the MPDATA based schemes to a van Leer based scheme generalised to multiple dimensions via isotropic or Strang split remapping. The results demonstrate the advantages of the fully multidimensional MPDATA remapping.

Acknowledgements

I would gratefully like to thank Joanna Szmelter for all her help, support and patience throughout the course of the research.

Particular thanks to Andy Barlow and Robert Kevis for many useful discussions and considerations. Thanks also to Jenny Morrell for supplying the SALE code, and Robert Kevis for supplying the MMALE code in which the research has been implemented.

I would like to acknowledge the financial support from the Atomic Weapons Establishment (AWE), Aldermaston.

Thanks also to my parents for their continuing support.

Contents

List of Figures

List of Tables

Nomenclature

ψ	Scalar variable
Ψ	Scalar variable multiplied by volume
F	Flux function
u, v	Components of velocity
U, V	Courant numbers
C	Overlap volume based Courant number
$\hat{C}$	Monotonic overlap volume based Courant number
$\bar{C}$	Mean value of overlap volumes
$V^{(-)}$	Pre-remap element volume
$V^{(+)}$	Post-remap element volume
ΔV	Overlap volume
$\mathbf{v}$	Velocity vector
ξ	Monotonicity coefficient
ζ	FCT limiting coefficient
β	Second-order filtering coefficient
ξ, η	Tensor product mesh motion parameters
θ, ϕ	Mesh rezone parameters
ρ	Density
e	Internal energy
p	Pressure
$\mathbf{q}$	Artificial viscosity
c_l, c_q	Linear and quadratic terms of artificial viscosity

M	Mass
γ	Ratio of specific heats
κ	Flux coefficient
λ	Volume fraction
λ^f	Flux volume fraction
m	Material index
E	Error measure
$[\,]^+$	Function returning a positive value, zero otherwise
$[\,]^-$	Function returning a negative value, zero otherwise
$^{(1)}$	Superscript denoting a first pass value
f	Pseudo velocity parameter
$A^{(1)}, B^{(1)}$	Derivative approximations for pseudo velocities
$\delta x, \delta y$	Spatial discretisations
δt	Computational time step
F^L, F^H	Low and high order fluxes
T	Truncation error
$\tilde{T}$	Limited truncation error

1 Introduction

This research is concerned with the implementation of the Multidimensional Positive Definite Advection Transport Algorithm (MPDATA) advection scheme into the remapping phase of an arbitrary Lagrangian-Eulerian (ALE) hydrocode with the intention to improve conservation and symmetry of physical variables being transported.

A hydrocode may be described as a code for solving large deformation, finite strain transient problems that occur on a short timescale [1]. Hydrocodes differ from Computational Fluid Dynamics (CFD) codes in that they must be applicable to solid materials in addition to liquids and gases [2]. An efficient hydrocode must incorporate numerous physics models, such as shock physics and material strengths for example. With the introduction of multiple materials in a single model, the hydrocode and the numerical schemes implemented within the code, must conservatively be compatible with general equations of state, material boundaries and additional physics such as material strength [2].

Within an arbitrary Lagrangian-Eulerian (ALE) hydrocode implementation, a solution is discretised onto a computational mesh, and evolved in time from prescribed initial conditions via repeated applications of three calculation phases. A Lagrangian calculation advances the solution and computational mesh in time. A rezone phase defines a new computational mesh that will have improved computational properties compared to the post-Lagrangian calculation mesh. A remap phase will then interpolate the Lagrangian solution from the post-Lagrangian computational mesh to the rezoned mesh. The ALE procedure is discussed in greater detail in Section 4.

The remapping phase is the focus of this research. MPDATA is a proven advection scheme which is conservative, sign preserving, formally second-order

accurate in arbitrary directional flows and computationally robust [3]. Such properties are particularly desirable for remapping. The MPDATA implementation for remapping will be detailed and comprehensively tested for single scalar variables, and ALE calculations containing one or multiple materials. Comparisons will be drawn against a current benchmark remapping method - the second-order van Leer MUSCL algorithm.

This work is structured as follows. Chapter 2 begins by introducing the underlying definitions of a computational mesh used for remapping. The advection methods currently utilised for the remapping phase are then detailed, with novel extension of MPDATA to remapping specified. Single scalar variable remapping test cases are presented in Section 3 highlighting beneficial properties of MPDATA compared to the methods currently employed. These initial test cases also illuminate the benefits in utilising various options within the MPDATA remapping. A thorough definition of hydrocodes and the ALE approach is given in Section 4, together with a description of the ALE implementation used in this work, and how MPDATA remapping is employed within this implementation. Single material ALE test cases are presented in Section 5, again showing potential benefits of the MPDATA based remapping compared to the van Leer benchmark. In particular, an ability to repair the ALE solution via the utilisation of MPDATA properties is examined. Section 6 introduces considerations for ALE calculations operating with multiple materials. The extension of MPDATA to multimaterial ALE remapping is described, highlighting the potential increase in accuracy available at material interfaces compared to the benchmark. A description of the multimaterial ALE scheme used in this work is provided. Multimaterial test cases are examined in Section 7. Particular focus is given to the analysis of the behaviour of the benchmark and MPDATA remapping schemes at material interfaces. Conclusions are provided in Section 8.

2 Advection based Remapping

In order to numerically calculate an approximation of a simulation of fluid flow, the domain of interest is subdivided into a computational mesh comprised of nodes and elements (or cells). The physical properties of a material are then discretely represented on that mesh by being stored at either the cell centres or the vertices of the cells, i.e. the nodes. With the application of a flow field and the evolution of the solution in time via appropriate discrete time steps, the geometry of the mesh may change, with the associated variables following the mesh motion. This approach represents a Lagrangian calculation. Alternatively, the material variables may be transported through the computational mesh, with the mesh remaining fixed in space. This approach represents an Eulerian calculation.

In the Eulerian approach, advection methods are used to exchange the variables between neighbouring cells of a mesh according to the direction of flow acting upon that material. Within an ALE simulation, a Lagrangian calculation is performed which results in a deformed mesh. In order to remove, or reduce, the amount of deformation that the computational mesh experiences, the remapping phase is employed to return to the initial mesh, or to a relaxed mesh whose geometry is determined by a specified algorithm. In either case, the solution from the Lagrangian mesh must be interpolated back to the initial or relaxed, i.e. rezoned, mesh. The solution variables must then be exchanged between the elements of the post-Lagrangian mesh, to elements on the rezoned mesh. If the calculation time step is small enough such that the nodes of the elements do not leave the region covered by neighbouring elements, the exchange of variables will be determined by the intersections of an element on the post-Lagrangian mesh, and the same element on the rezoned mesh, together with its neighbouring elements.

Therefore the advection methods used to exchange variables between elements

of a mesh in an Eulerian calculation are ideal for use as a remapping (interpolation) tool in ALE schemes. By using advection methods to perform the remap step, the exchange of material is determined by the overlapping area or volume between two cells rather than the velocity or Courant number determining the direction that material moves between two cells. The overlap area or volume will be determined by the underlying mesh velocity and as such can be related to the classical advection methods. Identification of the link between the advection velocity or Courant number and overlapping volumes will allow the correct formulation of the advection based remapping methods.

2.1 The First-Order Upwind Scheme

The First-Order Upwind scheme (also known as Donor Cell), set out by Courant, Isaacson and Rees [4], is one of the most basic forms of numerical advection. The First-Order Upwind, henceforth referred to as 'Upwind', method transports material in the direction of the flow across cell interfaces. In this description, an 'upwind' cell donates material to the 'downwind' adjacent cell. The Upwind method is conservative - the total amount of material in the domain will remain constant because adjacent elements exchange finite quantities of material directly, with no loss or gain occurring in the exchanges. The method is also monotonic - so that it is free of oscillations; computationally efficient - due to the simplicity of the underlying equations and is first-order accurate, although higher order upwind schemes exist. Details of the standard formulation of the first-order Upwind scheme - whereby the exchange is determined directly by the velocity of the mesh are available in numerous texts [3, 5, 6]. The overlap volume based first-order Upwind scheme for remapping is detailed in references [1, 2, 7, 8], and due to its fundamental importance to this work, a brief description of the advective form,

and the corresponding remapping form are outlined below.

The transport equation of a single scalar variable in two dimensions is given as

$$\frac{\partial \psi}{\partial t} = -\frac{\partial}{\partial x}(u\psi) - \frac{\partial}{\partial y}(v\psi). \tag{1}$$

Equation (1) is approximated by the Upwind advection method by taking a forward difference approximation of the partial temporal derivative, and a central difference approximation of the spatial derivative. Adopting the notation of [3], the Upwind representation is given by

$$\begin{aligned} \psi_{i,j}^{n+1} = \psi_{i,j}^{n} - & \left[F(\psi_{i,j}^{n}, \psi_{i+1,j}^{n}, U_{i+1/2,j}) - F(\psi_{i-1,j}^{n}, \psi_{i,j}^{n}, U_{i-1/2,j})\right] \\ - & \left[F(\psi_{i,j}^{n}, \psi_{i,j+1}^{n}, V_{i,j+1/2}) - F(\psi_{i,j-1}^{n}, \psi_{i,j}^{n}, V_{i,j-1/2})\right] \end{aligned} \tag{2}$$

where F is defined in terms of Courant numbers U and V as the flux of the variables across element boundaries

$$F(\psi_L, \psi_R, U) \equiv [U]^{+}\psi_L + [U]^{-}\psi_R \tag{3}$$

with

$$U \equiv \frac{u\delta t}{\delta x}, \quad V \equiv \frac{v\delta t}{\delta y}. \tag{4}$$

Integer index values represent the centre of the cells where the transported variable is stored, and half integer values represent the nodes of a cell where the mesh velocities are stored.

The remapping form of the Upwind method utilises volume co-ordinates. Volume co-ordinates are used as a measure of spatial distance, with much greater flexibility when the underlying mesh geometry is complex [1]. By using volume co-ordinates, the element centroid is defined by taking the volume integral over the cell. The intersecting (overlapping) volumes between elements are then used

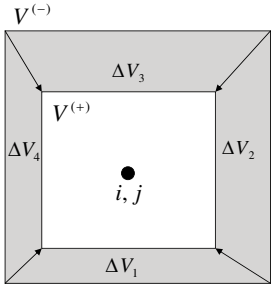

Figure 1: Definition of remapping volumes.

in flux calculations, with mean values of the scalar stored at the centroid of each volume component.

By exchanging quantities between the post-Lagrangian cell and the same cell on the rezoned mesh, the Upwind remapping scheme also requires the cell volume to be updated. The remap step does not advance the solution in time, therefore the post-Lagrangian and rezoned meshes represent the same time level. To distinguish between the values on the two different meshes, the post-Lagrangian grid values are denoted with superscript $^{(-)}$ and the post-remap grid values denoted with superscript $^{(+)}$. The volume of the cell on the rezoned grid is determined by the volume of the cell on the post-Lagrangian mesh, together with the changes in volume across each edge of the cell, as shown in Figure 1. The volume update of a cell in volume co-ordinates for arbitrary flows and configurations of Figure 1 is

$$V^{(+)} = V^{(-)} - \Sigma_{k=1}^{n} \Delta V_k, \tag{5}$$

where ΔV_k is the signed overlapping volume for the k^{th} face of the cell. The value of any scalar variable in this post-remap cell volume will then be equal to the value of the scalar within the post-Lagrangian cell combined with the value of the scalar in the overlapping volumes.

$$V^{(+)}\psi^{(+)} = V^{(-)}\psi^{(-)} - \Sigma_{k=1}^{n} \Delta V_k \psi_k, \tag{6}$$

where ψ_k is the scalar present in the cell overlapped by ΔV_k. The new value of the scalar on the post-remap grid is then given by the value of the scalar in the post-Lagrangian cell plus the fluxes of the remapped variable entering or leaving the cell.

$$\psi^{(+)} = \frac{V^{(-)}\psi^{(-)}}{V^{(+)}} - \frac{1}{V^{(+)}}\Sigma_{k=1}^{n}\Delta V_k\psi_k. \tag{7}$$

To reveal the connection between the remapping and advection forms of the Upwind method, it is useful to define $\Psi = V\psi$. Substituting Ψ into (6) and multiplying both sides by $V^{(-)}/V^{(-)}$, the scalar update becomes

$$\Psi^{(+)} = \Psi^{(-)} - \Sigma_{k=1}^{4}\frac{\Delta V_k}{V^{(-)}}\Psi_k^{(-)}, \tag{8}$$

which is now in the form of Upwind advection (2), with $\Delta V_k/V^{(-)}$ being akin to the Courant number evaluated at edge k of an element. For consistency, the volume in the denominator of (8) is obtained by averaging over element volumes on either side of the edge.

The Upwind method is a simple technique with good stability characteristics and features many of the properties an advection scheme should include. However first-order schemes are highly dissipative, resulting in a heavily smoothed solution. This may not be an accurate representation for many practical examples, and leads to higher order accuracy schemes utilised in practical hydrocodes. As a result of the positive features of the first-order Upwind scheme, numerous higher order schemes use Upwind as a basis in an attempt to gain greater accuracy while retaining the inherent desirable properties. The two key methods employed in this work utilise the Upwind scheme in different ways. The van Leer Monotone Upwind Schemes for Conservation Laws (MUSCL) approach - as currently employed by most ALE schemes [1, 2] achieves higher order accuracy by performing the Upwind remap with an alternative approximation of the distribution of variables within a cell, resulting in additional terms in the flux function.

The MPDATA scheme performs iterations of the standard Upwind calculation, calculating an estimate of the leading error introduced in the first pass to be used in a second Upwind calculation to obtain second-order accuracy. The identification of the dimensionless quantity which takes the role of the Courant number for remapping is particularly useful for the extension of MPDATA advection to MPDATA-based remapping.

2.2 The van Leer MUSCL Schemes

The Upwind scheme assumes a piecewise constant distribution of a scalar variable ψ within a particular cell by taking the mean value of the variable over the cell. Van Leer's MUSCL schemes [9] obtain second-order accuracy by constructing a piecewise linear distribution of the variable by utilising a larger computational stencil. The distribution created may be unstable. Stability is obtained by applying a monotonic limiter to the distribution.

The MUSCL schemes are one-dimensional methods that are extended to multiple dimensions on Cartesian grids by performing multiple one-dimensional sweeps of the mesh. This technique may readily be used for Cartesian grids because there are clearly defined directions to perform the sweeps, although a lag, or corner coupling error, is introduced. Corner coupling [10] describes the situation where advection takes place indirectly between diagonal elements. For example, on an orthogonal mesh, material travelling to diagonal elements must first pass through faces of an intermediate element and as a result will occur over two time steps. Consequently an incorrect amount of material will be advected when compared to a direct exchange over one time step. Lag effects may be reduced by using the Strang operator splitting method [11]. This method alternates the execution of the one dimensional sweeps at each time step. In the case that

a sweep is performed in the x-direction followed by a sweep in the y-direction in the current time step, the subsequent time step will perform a sweep in the y-direction first, followed by the x-direction sweep. The second one-dimensional sweep will also utilise the updated values of the volume and transported variable from the first one-dimensional sweep. This allows the transported variable to be exchanged between diagonal cells in one time step, however the symmetry of an axisymmetric solution may not be perfectly preserved [11].

Alternatively, for unstructured meshes (and also equally applicable to structured meshes), an isotropic application of the scheme may be applied. In this case, fluxes of the transported variables will be accumulated from the surrounding cells that share a common cell face in one update. This allows the one-dimensional method to be applied in multiple dimensions without needing predefined sweep directions, however material will not be exchanged between adjacent cells that do not share a cell face. An advection method which does not impinge upon the solution due to dimension restrictions is therefore an advantage.

Full details of the van Leer schemes customised for ALE hydrocodes are given in references [2, 7], however a brief explanation of the one-dimensional second-order van Leer scheme in volume co-ordinates is useful. The update of the transported variable takes the same structure as the Upwind scheme described in equations (5-7), however the values of the solution in the overlap volume fluxes are altered due to the different scalar distribution constructed in the cells. The first step of the scheme therefore replaces the mean valued initially piecewise constant distribution, with a linear distribution of the variable ψ within the cell. Given the factors affecting ALE meshes [2] the slope of the linear distribution is obtained by fitting a parabola to the variable ψ over three adjacent cells in the

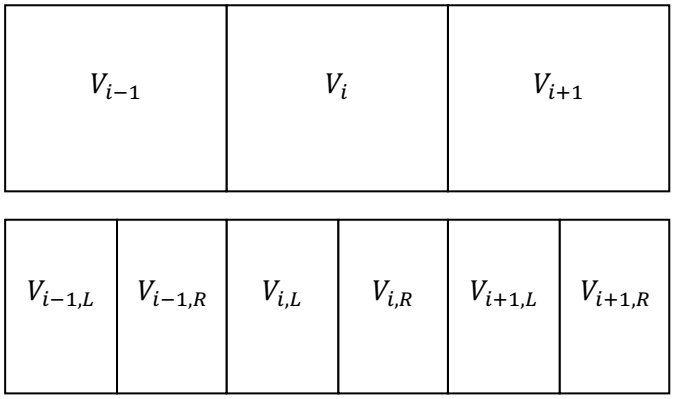

Figure 2: Indexing of elements and subdivision of element volumes in 1D.

direction of the advection sweep. The slope is given as:

$$\frac{\partial \psi_i}{\partial x} = \frac{(\psi_{i+1} - \psi_i)\,\Delta x_i^2 + (\psi_i - \psi_{i-1})\,\Delta x_{i+1}^2}{\Delta x_i \Delta x_{i+1}\,(\Delta x_i + \Delta x_{i+1})}, \tag{9}$$

where x is the direction of the sweep and $\Delta x_i = x_i - x_{i-1}$.

This slope cannot be guaranteed to be free of oscillations. In order to regain monotonicity, the slope (9) is applied to Benson's limiter [7]:

$$\psi_i' = \frac{1}{2}\left(sgn\left(\Delta\psi_i\right) + sgn\left(\Delta\psi_{i+1}\right)\right) min\left(\left|\frac{\partial \psi_i}{\partial x}\right|, \left|\Delta\psi_i\right|, \left|\Delta\psi_{i+1}\right|\right); \tag{10}$$

$$\Delta\psi_i = \frac{\psi_i - \psi_{i-1}}{x_i - x_{i-1}}, \tag{11}$$

where

$$x_i = V_{i-1,R}^{(-)} + V_{i,L}^{(-)}, \qquad x_{i+1} = V_{i,R}^{(-)} + V_{i+1,L}^{(-)}, \tag{12}$$

as shown in Fig. 2.

The fluxes in equation (6) are now defined as

$$\left(\Delta V \psi\right)_{i,L} \equiv \Delta V_{i,L}\left(\psi_i^- - \psi_{i,L}'\left(V_{i,L}^- + \frac{1}{2}\Delta V_{i,L}\right)\right) \tag{13}$$

$$(\Delta V\psi)_{i,R} \equiv \Delta V_{i,R}\left(\psi_i^- - \psi'_{i,R}\left(V_{i,R}^- + \frac{1}{2}\Delta V_{i,R}\right)\right) \tag{14}$$

corresponding to fluxes on the left and right hand faces of an element respectively, and $\psi'_{i,L}$ and $\psi'_{i,R}$ are the limited slopes of the variable ψ's distribution on the left and right hand faces of the cell, respectively. The updated solution is then given as

$$\begin{aligned}\psi_i^{(+)} &= \frac{V_i^{(-)}\psi^{(-)}}{V_i^{(+)}} \\ &- \frac{1}{V_i^{(+)}}\left((\Delta V\psi)_{i,L} + (\Delta V\psi)_{i+1,R} + (\Delta V\psi)_{i-1,L} + (\Delta V\psi)_{i,R}\right)\end{aligned} \tag{15}$$

In the case of a Strang split implementation, the variable ψ would be updated by a sweep in the x-direction as detailed in equations (5,9-15). A second sweep would then take place in the y-direction, where the cell volumes V are those following the update of the first sweep, and the overlap volumes ΔV calculated from this intermediate volume. If an unstructured mesh based update were used, where fluxes over all edges of the cell are dealt with at once, the terms in equation (15) would remain the same, but now also include flux terms in both the x- and y-directions.

2.3 The MPDATA Method

The Multidimensional Positive Definite Advection Transport Algorithm (MPDATA) [3, 5, 12, 13, 14] scheme executes iterations of the first-order Upwind scheme. Within the first iteration, or pass, standard Upwind advection is performed. Prior to the second pass, an estimation of the first-order truncation error of the first pass is made. This diffusive term is compensated by substituting it with an advection term representing an antidiffusive velocity advecting the transported variable. The antidiffusive (pseudo) velocity field has no physical

representation and is used to perform a second Upwind advection step. The two-pass MPDATA scheme is second-order accurate, conservative, sign preserving and computationally efficient [3] due to the iterative nature of reusing a simple advection function. Further passes are also possible, with each pass further reducing the second-order truncation error.

The formulation of MPDATA does not restrict its application to any number of dimensions. For example, on a Cartesian grid in the x,y plane, when calculating the exchange of a transported variable in the x-direction, information from the first-order pass in the y-direction of adjacent cells is included in the calculation of the error for the second pass. In this way, information is exchanged between the diagonal cells at each time step.

Although the underlying ideas of MPDATA formed the basis of a scheme developed by Margolin and Shashkov [15, 16] for prescribed mesh movement remapping, MPDATA has not previously been used for ALE remapping. Therefore, a description of the derivation of MPDATA as an advection method, and considerations required to convert the scheme to volume coordinates is useful before presenting MPDATA in a form that is useful for remapping within an ALE code.

2.3.1 MPDATA Advection

Similarly to the Upwind advection scheme MPDATA approximates the transport equation (1). The key idea of MPDATA is to compensate for the truncation error of the Upwind scheme by reusing (2), but with a pseudo Courant number defined on the dissipative truncation error of the first pass in (2). Following the derivation of [3], and adopting the notation therein, the truncation analysis is performed by expanding (2) in a Taylor series about a point (i, j) at time level n to obtain an advection equation with diffusive terms. The velocities u,v are

assumed to be constant for simplicity in performing a truncation analysis.

$$\begin{aligned}\frac{\partial\psi}{\partial t} = &- \frac{\partial}{\partial x}(u\psi) - \frac{\partial}{\partial y}(v\psi) + \frac{|U|(\delta x)^2}{2\delta t}(1-|U|)\frac{\partial^2\psi}{\partial x^2} \\ &+ \frac{|V|(\delta y)^2}{2\delta t}(1-|V|)\frac{\partial^2\psi}{\partial y^2} - \frac{UV\delta x\delta y}{\delta t}\frac{\partial^2\psi}{\partial x\partial y}.\end{aligned} \tag{16}$$

By writing the advective-diffusive equation in a form using pseudo velocities $u^{(1)}$, $v^{(1)}$, and noting that the cross term permits a degree of freedom in the choice of pseudo velocities, (16) becomes

$$\frac{\partial\psi}{\partial t} = -\frac{\partial}{\partial x}(u\psi) - \frac{\partial}{\partial y}(v\psi) + \frac{\partial}{\partial x}(u^{(1)}\psi) + \frac{\partial}{\partial y}(v^{(1)}\psi), \tag{17}$$

where $u^{(1)}$, $v^{(1)}$ may be chosen as

$$u^{(1)} = \frac{|U|\,(\delta x)^2}{2\delta t}(1-|U|)\frac{1}{\psi}\frac{\partial\psi}{\partial x} - f\frac{UV\delta x\delta y}{\delta t}\frac{1}{\psi}\frac{\partial\psi}{\partial y}, \tag{18}$$

$$v^{(1)} = \frac{|V|\,(\delta y)^2}{2\delta t}(1-|V|)\frac{1}{\psi}\frac{\partial\psi}{\partial y} - (1-f)\frac{UV\delta x\delta y}{\delta t}\frac{1}{\psi}\frac{\partial\psi}{\partial x}, \tag{19}$$

where $f \in [0,1]$ is a real number which may be specified arbitrarily. The choice of the value f is useful when deriving advanced options of MPDATA [17], however, regarding implementation of (18),(19) the choice of f within the range $0 \le f \le 1$ bears no significant importance. Here, $f = 0.5$ is used as a default value in all MPDATA schemes.

As with the velocity components in the first Upwind pass, the pseudo velocities (18),(19) must be considered at the element faces and transformed into dimensionless pseudo Courant numbers

$$U^{(1)} \equiv \frac{u^{(1)}\delta t}{\delta x} = |U|\,(1-|U|)A^{(1)} - 2fUVB^{(1)} \tag{20}$$

$$V^{(1)} \equiv \frac{v^{(1)}\delta t}{\delta y} = |V|\,(1-|V|)B^{(1)} - 2(1-f)UVA^{(1)}, \tag{21}$$

where $A^{(1)}$ and $B^{(1)}$ are numerical estimates from the scalar field at a particular edge. For example, on the right face of element (i, j):

$$A^{(1)} \equiv \left[\frac{\delta x}{2\psi}\frac{\partial \psi}{\partial x}\right]^{n+1}_{i+1/2,j} = \frac{\left|\psi^{(1)}_{i+1,j}\right| - \left|\psi^{(1)}_{i,j}\right|}{\left|\psi^{(1)}_{i+1,j}\right| + \left|\psi^{(1)}_{i,j}\right|}, \tag{22}$$

$$B^{(1)} \equiv \left[\frac{\delta x}{2\psi}\frac{\partial \psi}{\partial x}\right]^{n+1}_{i+1/2,j} = \frac{1}{2}\frac{\left|\psi^{(1)}_{i+1,j+1}\right| + \left|\psi^{(1)}_{i,j+1}\right| - \left|\psi^{(1)}_{i+1,j-1}\right| - \left|\psi^{(1)}_{i,j-1}\right|}{\left|\psi^{(1)}_{i+1,j+1}\right| + \left|\psi^{(1)}_{i,j+1}\right| + \left|\psi^{(1)}_{i+1,j-1}\right| + \left|\psi^{(1)}_{i,j-1}\right|}, \tag{23}$$

with $\psi^{(1)}$ being the solution of the first Upwind pass and absolute values indicating that non-negativeness of the scalar field is not required. Although different approximations are possible, (22), (23) are bounded given the stability and positive definiteness of the Upwind scheme. This property aids the stability of MPDATA.

The second pass of the Upwind scheme is then performed to obtain the solution at the new time level

$$\begin{aligned}\psi^{(2)}_{i,j} = \psi^{(1)}_{i,j} - & \left[F(\psi^{(1)}_{i,j}, \psi^{(1)}_{i+1,j}, U^{(1)}_{i+1/2,j}) - F(\psi^{(1)}_{i-1,j}, \psi^{(1)}_{i,j}, U^{(1)}_{i-1/2,j})\right] \\ - & \left[F(\psi^{(1)}_{i,j}, \psi^{(1)}_{i,j+1}, V^{(1)}_{i,j+1/2}) - F(\psi^{(1)}_{i,j-1}, \psi^{(1)}_{i,j}, V^{(1)}_{i,j-1/2})\right].\end{aligned} \tag{24}$$

2.3.2 Volume Co-ordinate Considerations

The volume co-ordinate form of MPDATA follows from the advection derivation, with the volume overlap form of Upwind (8) utilised rather than the advection form (2). In order to use (8) however, a number of considerations must first be made.

When calculating the overlap volume, ΔV will inherently be either positive or negative due to the velocity used to determine the position of the post-remap nodes or face. Convention retains only the positive values of the overlap volume because each overlap volume will be calculated twice - once for each cell that

shares the common edge. Therefore one cell will view the overlap volume as positive, and one cell will view the overlap volume as negative. By setting the negative overlap volume to zero, the donor cell and receiving cell are inherently defined which has the effect of performing the flux function F. As a result, the summation of overlap quantities in (8) and the balancing of flux functions in (2) perform the same action.

The overlap volumes are not uniquely defined, and the definition used must be consistent with the derivation of MPDATA, and the use of Courant numbers for transport. Benson [8] details numerous methods to calculate an overlap volume including clipping, swept regions and average normal displacements. Clipping takes any overlapping area and cuts the area into pieces overlapping any adjacent cell on the post-remap mesh. Although this method allows transport between any element sharing a common node or edge, which is desirable for preservation of symmetry and corner coupling issues, the method is difficult to implement and so is rarely used in practice. Swept regions create an overlap volume by using the nodal velocities of the edge in question together with the computational time step to determine the position of each node after the remap. The positions of the nodes before and after the remap therefore determine the swept area. This allows the overlap area to be determined precisely regardless of the individual behaviour of the nodes, however this method does not allow transport between cells that only share a common node. The average normal displacement method is similar to the swept region method, however the nodal velocities are not used independently, but rather averaged prior to the utilisation of the calculation time step to determine the position of the edge after the remap. This may not give the same accuracy as the swept regions method, and will also not permit transport between cells only sharing a common node. However this method will be very easy to implement because the overlap area will always be rectangular due to

the use of a normal velocity, whereas the swept regions method will permit any quadrilateral as the overlap area.

Due to the practical difficulties inherent in the clipping method, only the swept regions and average normal displacement methods shall be considered further.

The swept region overlap volume ΔV_{SR} is calculated by determining the position of the nodes of a face after the remap. Prior to the remap, the nodes will have positions (x_1, y_1) and (x_2, y_2). Post remap, the nodes will have positions $(x_1 + u_1\delta t, y_1 + v_1\delta t)$ and $(x_2 + u_2\delta t, y_2 + v_2\delta t)$ respectively. The area defined by these four nodal positions may then be calculated by various methods so that

$$\begin{aligned}\Delta V_{SR} = \quad area \quad & [(x_1, y_1), (x_2, y_2), \\ & (x_1 + u_1\delta t, y_1 + v_1\delta t), (x_2 + u_2\delta t, y_2 + v_2\delta t)]. \end{aligned} \tag{25}$$

The average normal displacement overlap volume ΔV_{AND} is calculated by multiplying the length of the face, l_f, by the length obtained by moving the face with average normal velocity $\mathbf{v}$ and calculation time δt:

$$\Delta V_{AND} = l_f \mathbf{v} \delta t. \tag{26}$$

With regards to the application of the two described methods to determine the overlap area into an MPDATA remap scheme, $\Delta V_{SR}/V^{(-)}$ or $\Delta V_{AND}/v^{(-)}$ will replace the dimensionless Courant numbers (4) in the first-order Upwind steps and the calculation of the pseudo Courant number for the compensation of the second-order truncation error.

Depending on the form of overlap volume used, the dimensionless quantity used in (8) may or may not reduce exactly to the Courant number used in (2). For illustration, if a Cartesian grid is assumed, the average normal displacement overlap volumes (26) in the x and y directions are defined as

$$\Delta V_x = \delta y^{(-)} \mathbf{v}_1 \delta t,$$

$$\Delta V_y = \delta x^{(-)} \mathbf{v}_2 \delta t, \tag{27}$$

so that

$$\frac{\Delta V_x}{V^{(-)}} = \frac{\delta y^{(-)} \mathbf{v} \delta t}{V^{(-)}} = \frac{\delta y^{(-)} \mathbf{v} \delta t}{\delta x^{(-)} \delta y^{(-)}} = \frac{\vec{v}_1 \delta t}{\delta x^{(-)}}, \tag{28}$$

$$\frac{\Delta V_y}{V^{(-)}} = \frac{\delta x^{(-)} \mathbf{v} \delta t}{V^{(-)}} = \frac{\delta x^{(-)} \mathbf{v} \delta t}{\delta x^{(-)} \delta y^{(-)}} = \frac{\mathbf{v} \delta t}{\delta y^{(-)}}, \tag{29}$$

which are exactly the Courant numbers used in equation (2). In this case, the remap form of MPDATA utilising $\Delta V_{AND}/V^{(-)}$ is identical to the Courant number used in the advection form.

When the swept region overlap volume is used, the dimensionless quantity used to determine the flux will depend on the function *area* used in (25). One method particularly suited to the overlap volumes generated by arbitrary flows is the formula for the area of an arbitrary polygon, p, [2]:

$$A_p = \frac{1}{2} \Sigma_s \sigma_s^p \left(x_1^s y_2^s - x_2^s y_2^s \right), \tag{30}$$

where the summation occurs over sides s defined by the points (x_1^s, y_1^s) and (x_2^s, y_2^s). The value of σ_s^p is +1 if the polygon lies to the left of the side s, and -1 if the polygon lies to the right of the side s. The overlap volume for the right hand face of an element will be a quadrilateral, with the sides evaluated in the order shown in Fig. 3

The swept region overlap volume ΔV_{SRx} is then given by:

$$\begin{aligned} \Delta V_{SRx} &= \frac{1}{2} \left[x_1 \left(y_1 + v_1 \delta t \right) - \left(x_1 + u_1 \delta t \right) y_1 + \left(x_1 + u_1 \delta t \right) \left(y_2 + v_2 \delta t \right) \right. \\ &- \left(x_2 + u_2 \delta t \right) \left(y_1 + v_1 \delta t \right) + \left(x_2 + u_2 \delta t \right) y_2 - x_2 \left(y_2 + v_2 \delta t \right) \\ &+ \left. x_2 y_1 - x_1 y_2 \right], \end{aligned}$$

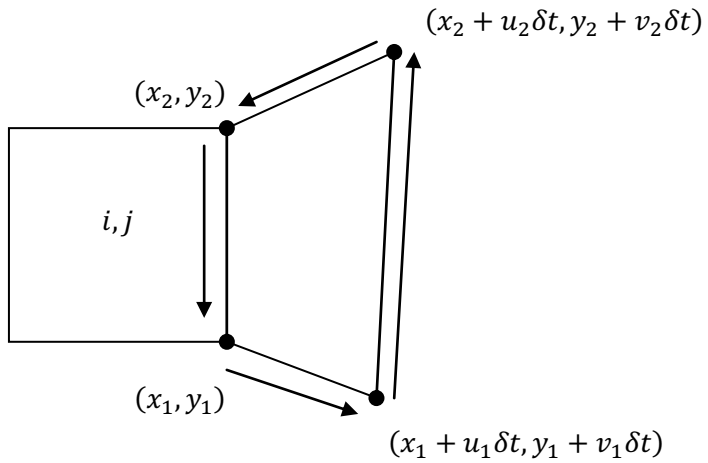

Figure 3: Direction of calculation for determining the overlap volume.

which becomes

$$\begin{aligned}\Delta V_{SRx} &= \frac{1}{2}\left[x_1v_1\delta t - y_1u_1\delta t + x_1v_2\delta t + y_2u_1\delta t\right.\\ &+ \left. u_1v_2\delta t^2 - x_2v_1\delta t - y_1u_2\delta t - u_2v_1\delta t^2 + y_2u_2\delta t - x_2v_2\delta t\right],\end{aligned}$$

$$\begin{aligned}\Delta V_{SRx} &= \frac{1}{2}\left[-\left(x_2 - x_1\right)v_1\delta t + \left(y_2 - y_1\right)u_1\delta t\right.\\ &- \left.\left(x_2 - x_1\right)v_2\delta t + \left(y_2 - y_1\right)u_2\delta t + \left(u_1v_2 - u_2v_1\right)\delta t^2\right],\end{aligned}$$

and because $x_1 = x_2$ on the vertical edges of a Cartesian grid, ΔV_{SRx} becomes

$$\Delta V_{SRx} = \frac{1}{2}\left[\delta y^{(-)}u_1\delta t + \delta y^{(-)}u_2\delta t + \left(u_1v_2 - u_2v_1\right)\delta t^2\right] \tag{31}$$

and defining $u = (u_1 + u_2)/2$

$$\Delta V_{SRx} = \delta y^{(-)}u\delta t + \left(u_1v_2 - u_2v_1\right)\delta t^2 \tag{32}$$

The dimensionless quantity $\Delta V_x/V^{(-)}$ then becomes

$$\frac{\Delta V_{SRx}}{V^{(-)}} = \frac{\delta y^{(-)}u\delta t}{\delta x^{(-)}\delta y^{(-)}} + \frac{\left(u_1v_2 - u_2v_1\right)\delta t^2}{\delta x^{(-)}\delta y^{(-)}} = \frac{u\delta t}{\delta x^{(-)}} + \frac{\left(u_1v_2 - u_2v_1\right)\delta t^2}{\delta x^{(-)}\delta y^{(-)}}. \tag{33}$$

Comparing (33) with (28) it is clear that both forms of overlap volume are similar and produce the required Courant number, with the swept region method including extra terms that arise because of the independence of the nodal velocities. An analogous value is also available for $\Delta V_{SRy}/V^{(-)}$ with $\delta y^{(-)}$ replacing $\delta x^{(-)}$, and v replacing u in (33). The additional term that arises in (32) should provide greater accuracy in the volume update because it is utilising the information provided by the independent nodal velocities rather than smearing the information as is the case with the average normal displacement method. However, the effects of the additional term in (33) when calculating the pseudo velocity for MPDATA are unknown because MPDATA is derived to operate with a single normal velocity per edge. The swept region method would also be preferable for general and unstructured grids within a remap step because the new cell volume would be completely represented by the old cell volume and the swept volumes.

2.3.3 MPDATA Remapping

The formulation of MPDATA in volume co-ordinates is now presented. The first step of the MPDATA remapping scheme is an initial pass of the first-order Upwind scheme in volume co-ordinates, detailed in Section 2.1. Defining $C = \Delta V/V^{(-)}$, (8) may be written in flux form as

$$\begin{aligned}\Psi^{(1)}_{i,j} = \Psi^{(-)}_{i,j} - \quad & [F(\Psi^{(-)}_{i,j}, \Psi^{(-)}_{i+1,j}, C_{i+1/2,j}) - F(\Psi^{(-)}_{i-1,j}, \Psi^{(-)}_{i,j}, C_{i-1/2,j})] \\ - \quad & [F(\Psi^{(-)}_{i,j}, \Psi^{(-)}_{i,j+1}, C_{i,j+1/2}) - F(\Psi^{(-)}_{i,j-1}, \Psi^{(-)}_{i,j}, C_{i,j-1/2})], \end{aligned} \quad (34)$$

where the superscript $^{(1)}$ denotes values after the first Upwind pass, $^{(-)}$ denotes the pre-remap value and $^{(+)}$ denotes the post-remap value.

The flux form of the Upwind scheme is given rather than the standard form of the volume co-ordinate Upwind scheme due to the need to retain information about positive and negative overlap volumes for the pseudo velocity calculation.

When calculating the pseudo velocity, advection velocities - or overlap volumes in the remap case - are required in both the normal direction and the direction parallel to the cell face being dealt with. For each cell face however, there is only one associated overlap volume, which will act in the direction normal to the face. In order to obtain an overlap volume acting in the parallel direction to the cell face, an average of the surrounding overlap volumes acting in that direction must be taken, as shown in Fig. 4.

In order to utilise this information within a straightforward implementation, all overlap volumes must be available, regardless of the sign of the overlap volume. If negative overlap volumes were set to zero, the calculated average of the overlap volume in the parallel direction would not be correct. Overlap volumes may still only be calculated once for an efficient implementation, with the value for the other cell sharing the common cell edge being set to the same value but with the opposite sign.

By using the defined Courant number-like quantity C, equation (20) becomes

$$C^{(1)}_{i+1/2,j} \equiv \left|C_{i+1/2,j}\right| (1 - \left|C_{i+1/2,j}\right|) A^{(1)} - 2 f \bar{C}_{i,j+1/2} C_{i+1/2,j} B^{(1)}, \tag{35}$$

where

$$\bar{C}_{i,j+1/2} = \frac{1}{4} \left(C_{i,j+1/2} + C_{i,j-1/2} + C_{i+1,j+1/2} + C_{i+1,j-1/2} \right), \tag{36}$$

and (21) becomes

$$C^{(1)}_{i,j+1/2} \equiv \left|C_{i,j+1/2}\right| (1 - \left|C_{i,j+1/2}\right|) B^{(1)} - 2 (1 - f) \bar{C}_{i+1/2,j} C_{i,j+1/2} A^{(1)}, \tag{37}$$

$$\bar{C}_{i+1/2,j} = \frac{1}{4} \left(C_{i+1/2,j} + C_{i-1/2,j} + C_{i+1/2,j+1} + C_{i-1/2,j+1} \right). \tag{38}$$

The quantities $A^{(1)}$ and $B^{(1)}$ remain in the same form as in (22) and (23), with the exception that each ψ is replaced by Ψ.

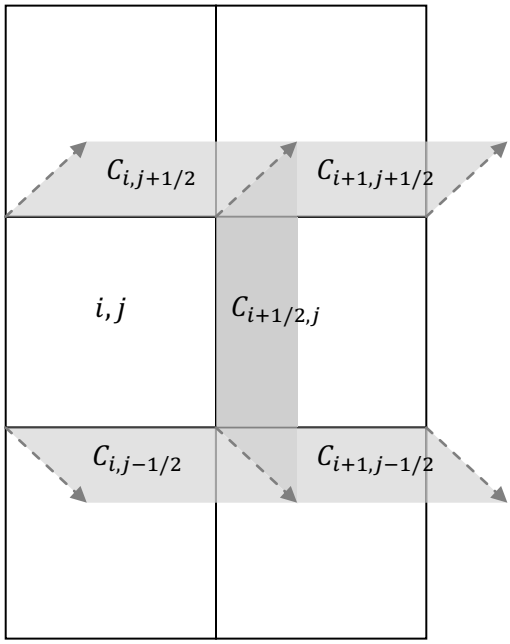

Figure 4: Averaging of surrounding overlap volumes acting the direction parallel to the cell face.

Finally, a second Upwind pass is performed to give the remapped solution:

$$\begin{aligned}\Psi^{(+)}_{i,j} = \Psi^{(1)}_{i,j} - & \quad [F(\Psi^{(1)}_{i,j}, \Psi^{(1)}_{i+1,j}, C^{(1)}_{i+1/2,j}) - F(\Psi^{(1)}_{i-1,j}, \Psi^{(1)}_{i,j}, C^{(1)}_{i-1/2,j})] \\ - & \quad [F(\Psi^{(1)}_{i,j}, \Psi^{(1)}_{i,j+1}, C^{(1)}_{i,j-1/2}) - F(\Psi^{(1)}_{i,j-1}, \Psi^{(1)}_{i,j}, C^{(1)}_{i,j+1/2})]. \qquad (39)\end{aligned}$$

The scalar $\psi^{(+)}_{i,j}$ may be recovered by dividing (39) by $V^{(+)}$. Further details of the proposed MPDATA based remapping scheme are available in [18].

2.4 Non-Oscillatory extension of MPDATA

As with the unlimited form of the higher order van Leer schemes, the basic form of MPDATA (referred to herein as basic MPDATA) described above permits the formation and growth of oscillations. This feature arises because the approximation of the truncation error by MPDATA may be over- or under-estimated. The combination of over- and under-estimates results in the formation of oscillations. This feature reveals that although MPDATA is sign preserving (historically referred to as positive definite) it is not monotonic. Imposing monotonicity reduces the magnitude of the dissipative error and may be attained by introducing the non-oscillatory option of MPDATA. This option applies a limit to the pseudo velocity field to ensure that the truncation error is compensated without introducing new maxima or minima. This approach is achieved by applying the formalism of the Flux Corrected Transport (FCT) algorithm to the iterative nature of MPDATA. The derivation of the FCT scheme is therefore given. In contrast to the FCT algorithm which limits fluxes, MPDATA uniquely limits the anti-diffusive velocities. A description of the application of FCT to the pseudo velocities in MPDATA advection is then provided followed by the extension to MPDATA remapping.

2.4.1 Flux Corrected Transport (FCT) Scheme

The Flux Corrected Transport (FCT) [19, 20, 21, 22] scheme operates with a predictor-corrector style, where a first-order non-oscillatory scheme advances the solution forward in time. An estimate of the dissipative error is then removed with the purpose of attaining higher order accuracy. Limiting in FCT schemes is achieved by comparing the higher order solutions of the scheme to the lower order solutions. This allows new extreme values, which will be a source for oscillations, to be identified. Growth of the extreme values is avoided by limiting the magnitude of the fluxes. This ensures that the fluxes are not overestimated to the point where the maximum or minimum value is exceeded when the fluxes are collected for each element.

The derivation of FCT, as given in [23], follows from the definition of a general higher order one-dimensional advection scheme

$$\psi_i^{n+1} = \psi_i^n - F_{i+1/2}^H + F_{i-1/2}^H, \tag{40}$$

the high order flux F^H may be written as a combination of a low order non-oscillatory flux, F^L, and a flux compensating at least the first-order truncation error, T, i.e.

$$F_{i+1/2}^H \equiv F_{i+1/2}^L + T_{i+1/2}. \tag{41}$$

As a result of the definition of T this flux may be considered as an antidiffusive flux. Combining (40) and (41) gives

$$\psi_i^{n+1} = \psi_i^{n+1} - T_{i+1/2} + T_{i-1/2}, \tag{42}$$

where ψ represents the solution of the low order scheme using F^L which satisfies

$$\psi_i^{\mathrm{MAX}} \geq \psi_i^{n+1} \geq \psi_i^{\mathrm{MIN}} \tag{43}$$

by the assumption that the low order scheme is nonoscillatory.

The quantities ψ_i^{MAX} and ψ_i^{MIN} represent the maximum and minimum values of the local scalar field surrounding the i^{th} cell edge. These values are used to help preserve the monotonicity of the scheme, however monotonicity is fully achieved by removing the overestimates of the antidiffusive fluxes. This is achieved by applying limiting coefficients based upon the values of ψ_i^{MAX} and ψ_i^{MIN} to the antidiffusive fluxes

$$\widetilde{T}_{i+1/2} = \zeta_{i+1/2} \cdot T_{i+1/2}, \tag{44}$$

where the ζ coefficients are determined according to the constraints

$$0 \leq \zeta_{i+1/2} \leq 1 \tag{45}$$

and

$$\psi_i^{\mathrm{MAX}} \geq \widetilde{\psi}_i^{n+1} = \psi_i^{n+1} - \widetilde{T}_{i+1/2} + \widetilde{T}_{i-1/2} \geq \psi_i^{\mathrm{MIN}}. \tag{46}$$

It is worth noting that in the case where ζ is equal to zero, the original low order scheme is recovered, and when ζ is equal to one, the original higher order scheme is recovered. The explicit form of ζ is obtained by separating the antidiffusive fluxes into incoming and outgoing fluxes

$$-\widetilde{T}_{i+1/2} + \widetilde{T}_{i-1/2} = \widetilde{T}_i^{\mathrm{IN}} - \widetilde{T}_i^{\mathrm{OUT}}, \tag{47}$$

where

$$\widetilde{T}_i^{\mathrm{IN}} \equiv \zeta_{i-1/2} \left[T_{i-1/2}\right]^+ - \zeta_{i+1/2} \left[T_{i+1/2}\right]^-, \tag{48}$$

$$\widetilde{T}_i^{\mathrm{OUT}} \equiv \zeta_{i+1/2} \left[T_{i+1/2}\right]^+ - \zeta_{i-1/2} \left[T_{i-1/2}\right]^-. \tag{49}$$

Replacing (47) in (46) gives

$$\psi_i^{\mathrm{MAX}} \geq \widetilde{\psi}_i^{n+1} = \psi_i^{n+1} + \widetilde{T}_i^{\mathrm{IN}} - \widetilde{T}_i^{\mathrm{OUT}} \geq \psi_i^{\mathrm{MIN}}, \tag{50}$$

where it can be seen that $\widetilde{\psi}_i^{n+1}$ can only be increased by $\widetilde{T}_i^{\mathrm{IN}}$ and only be decreased by $\widetilde{T}_i^{\mathrm{OUT}}$. Therefore, to ensure (46) it is sufficient to satisfy

$$\psi_i^{\mathrm{MAX}} - \psi_i^{n+1} \geq max(\zeta_{i-1/2}, \zeta_{i+1/2}) T_i^{\mathrm{IN}}, \tag{51}$$

$$\psi_i^{n+1} - \psi_i^{\mathrm{MIN}} \geq max(\zeta_{i-1/2}, \zeta_{i+1/2}) T_i^{\mathrm{OUT}}, \tag{52}$$

where T_i^{IN} and T_i^{OUT} are now defined as

$$T_i^{\mathrm{IN}} \equiv \left[T_{i-1/2}\right]^+ - \left[T_{i+1/2}\right]^-, \tag{53}$$

$$T_i^{\mathrm{OUT}} \equiv \left[T_{i+1/2}\right]^+ - \left[T_{i-1/2}\right]^-. \tag{54}$$

The new constraints (51), (52) imply

$$max(\zeta_{i-1/2}, \zeta_{i+1/2}) \leq \xi_i^{\mathrm{IN}} \equiv \frac{\psi_i^{\mathrm{MAX}} - \psi_i^{n+1}}{T_i^{\mathrm{IN}} + \epsilon}, \tag{55}$$

$$max(\zeta_{i-1/2}, \zeta_{i+1/2}) \leq \xi_i^{\mathrm{OUT}} \equiv \frac{\psi_i^{n+1} - \psi_i^{\mathrm{MIN}}}{T_i^{\mathrm{OUT}} + \epsilon}, \tag{56}$$

with ϵ, $\mathcal{O}(10^{-10})$ included for computational efficiency in the case where division would otherwise be by zero.

Constraints (55), (56) further yield

$$\zeta_{i\pm1/2} \leq min(\xi_i^{\mathrm{IN}}, \xi_i^{\mathrm{OUT}}) \tag{57}$$

and noting that $\zeta_{i\pm1/2} \equiv \zeta_{(i\pm1)\mp1/2}$ leads to the additional constraint

$$\zeta_{i\pm1/2} \leq min(\xi_{i\pm1}^{\mathrm{IN}}, \xi_{i\pm1}^{\mathrm{OUT}}), \tag{58}$$

so that

$$\zeta_{i+1/2} \leq min(1, \xi_i^{\mathrm{IN}}, \xi_i^{\mathrm{OUT}}, \xi_{i+1}^{\mathrm{IN}}, \xi_{i+1}^{\mathrm{OUT}}). \tag{59}$$

Unity is included in the condition to ensure that the limited antidiffusive flux does not exceed the original higher order scheme antidiffusive flux, as noted for (44).

The final condition is sufficient for the monotonicity of the higher order scheme to be obtained. However, it can also be seen that ξ^{IN} and ξ^{OUT} control the over- and under-estimates respectively. Furthermore, $T_{i+1/2}$ in (44) is either positive or negative, and so it will either contribute to an overshoot to element i or to an undershoot at element $i+1$. Condition (59) may be separated into

$$\zeta_{i+1/2} = min(1, \xi_i^{OUT}, \xi_{i+1}^{IN})\ if\ T_{i+1/2} \geq 0, \tag{60}$$

$$\zeta_{i+1/2} = min(1, \xi_i^{IN}, \xi_{i+1}^{OUT})\ if\ T_{i+1/2} < 0. \tag{61}$$

Conditions (60), (61) may then be applied to (44) to complete the final step in the higher order FCT scheme.

2.4.2 Application of FCT to MPDATA Advection

The non-oscillatory extension to MPDATA advection is performed throughout the first Upwind pass and calculation of the pseudo velocities. Therefore, before and after the first pass of the Upwind scheme, the local maximum and minimum values of the transported variable around each element edge are stored. This ensures that the limited pseudo velocity does not allow the creation of new maxima or minima. Prior to being limited, the pseudo velocities must be created in the same manner as with the basic form of MPDATA. The basic pseudo velocities are used to calculate the initial second pass corrective fluxes. It is these fluxes, together with the local maximum and minimum values for each edge that are used to calculate coefficients which will limit the pseudo velocities. Once the limiting coefficients are calculated, limited pseudo velocities are calculated and

the corrective fluxes for the second pass re-evaluated. Finally, the second pass of the Upwind scheme is performed resulting in the non-oscillatory (monotonic) solution.

Similarly to the description of the standard form of MPDATA given in Section 2.3.1, the advection based method is first described, followed by the adaption of the scheme to a volume co-ordinate based remap MPDATA scheme. The non-oscillatory option of MPDATA is formulated directly from the previous discussion of the FCT scheme. The anti-diffusive fluxes used in the second (and further) passes are analogous to the T fluxes in the general FCT scheme. Furthermore, MPDATA is sign preserving, and the lower order F^L fluxes used are from the Upwind scheme which is monotonic. These features allow the specific MPDATA conditions corresponding to (55) and (56) for the monotonic pseudo velocity to be directly obtained as [23]

$$\xi_{i,j}^{\mathrm{IN}} = \frac{\psi_{i,j}^{\mathrm{MAX}} - \psi_{i,j}^{(1)}}{\sum_{k=1}^{N} \left[F_k^{(1)}\right]^{-} + \epsilon}, \tag{62}$$

$$\xi_{i,j}^{\mathrm{OUT}} = \frac{\psi_{i,j}^{(1)} - \psi_{i,j}^{\mathrm{MIN}}}{\sum_{k=1}^{N} \left[F_k^{(1)}\right]^{+} + \epsilon}, \tag{63}$$

where $F_k^{(1)}, k = 1..N$ represents the summation of the unlimited pseudo velocity fluxes across all edges of element. In the two dimensional orthogonal case described above, $N = 4$, i.e. the left, right, top and bottom edges.

The local maximum and minimum values around each edge are calculated from the cells used in the calculation of $A^{(1)}$ and $B^{(1)}$. For example, on the right face of an element

$$\psi_{i,j}^{MAX} = max(\psi_{i,j}^n, \psi_{i+1,j}^n, \psi_{i,j+1}^n, \psi_{i,j-1}^n, \psi_{i+1,j+1}^n \psi_{i+1,j-1}^n), \tag{64}$$

$$\psi_{i,j}^{MIN} = min(\psi_{i,j}^n, \psi_{i+1,j}^n, \psi_{i,j+1}^n, \psi_{i,j-1}^n, \psi_{i+1,j+1}^n \psi_{i+1,j-1}^n), \tag{65}$$

in addition, the *max* and *min* functions may be taken over $\psi^{(1)}$ in each of the spatial locations as used for ψ^n. In test cases shown here, values are taken exclusively from the $^{(1)}$ values.

The conditions may then be applied to the pseudo velocities to give the limited pseudo velocities. The explicit form of the monotonic pseudo velocity on the right face of an element is given as

$$\begin{aligned}
\widehat{U}^{(1)}_{i+1/2,j} = \quad & \left[U^{(1)}_{i+1/2,j}\right]^+ (min(1, \xi^{IN}_{i+1,j}, \xi^{OUT}_{i,j}) \left[sgn(\psi^{(1)}_{i,j})\right]^+ \\
+ \quad & min(1, \xi^{OUT}_{i+1,j}, \xi^{IN}_{i,j}) \left[sgn(-\psi^{(1)}_{i,j})\right]^+) \\
+ \quad & \left[U^{(1)}_{i+1/2,j}\right]^- (min(1, \xi^{OUT}_{i+1,j}, \xi^{IN}_{i,j}) \left[sgn(\psi^{(1)}_{i+1,j})\right]^+ \\
+ \quad & min(1, \xi^{IN}_{i+1,j}, \xi^{OUT}_{i,j}) \left[sgn(-\psi^{(1)}_{i+1,j})\right]^+), \qquad (66)
\end{aligned}$$

where the *sgn* function returns the sign of its parameter and $[sgn(\pm\ldots)]^+$ factors are used as logical switch operators so that the limiting is not restricted to non-negative or non-positive fields only, [5].

The limited second pass Upwind scheme then takes the form

$$\begin{aligned}
\widehat{\psi}^{(2)}_{i,j} = \psi^{(1)}_{i,j} \quad & - \quad [F(\psi^{(1)}_{i,j}, \psi^{(1)}_{i+1,j}, \widehat{U}^{(1)}_{i+1/2,j}) - F(\psi^{(1)}_{i-1,j}, \psi^{(1)}_{i,j}, \widehat{U}^{(1)}_{i-1/2,j})] \\
& - \quad [F(\psi^{(1)}_{i,j}, \psi^{(1)}_{i,j+1}, \widehat{V}^{(1)}_{i,j+1/2}) - F(\psi^{(1)}_{i,j-1}, \psi^{(1)}_{i,j}, \widehat{V}^{(1)}_{i,j-1/2})]. \qquad (67)
\end{aligned}$$

2.4.3 Non-Oscillatory MPDATA remapping

Applying volume co-ordinates to equations (62) to (67) is straightforward due to the considerations made during the formulation of the standard MPDATA remap scheme. Equations (62) and (63) remain unchanged, noting that $F^{(1)}_k$ in the denominators is defined as:

$$F^{(1)}_k \equiv F(\Psi^{(1)}_L, \Psi^{(1)}_R, C^{(1)}_k), \qquad (68)$$

where $C^{(1)}$ is defined in (35) or (37) depending on the required direction.

Equations (64) and (65) utilise Ψ rather than ψ, and equation (66) becomes

$$\begin{aligned}\widehat{C}^{(1)}_{i+1/2,j} = \quad & \left[C^{(1)}_{i+1/2}\right]^{+} (min(1, \xi^{IN}_{i+1,j}, \xi^{OUT}_{i,j}) \left[sgn(\Psi^{(1)}_{i,j})\right]^{+} \\ + \quad & min(1, \xi^{OUT}_{i+1,j}, \xi^{IN}_{i,j}) \left[sgn(-\Psi^{(1)}_{i,j})\right]^{+}) \\ + \quad & \left[C^{(1)}_{i+1/2,j}\right]^{-} (min(1, \xi^{OUT}_{i+1,j}, \xi^{IN}_{i,j}) \left[sgn(\Psi^{(1)}_{i+1,j})\right]^{+} \\ + \quad & min(1, \xi^{IN}_{i+1,j}, \xi^{OUT}_{i,j}) \left[sgn(-\psi^{(1)}_{i+1,j})\right]^{+}) \end{aligned} \tag{69}$$

for an overlap volume over the right hand edge of cell, and equation (67) becomes

$$\begin{aligned}\widehat{\Psi}^{(+)}_{i,j} = \Psi^{(1)}_{i,j} \quad & - \quad [F(\Psi^{(1)}_{i,j}, \Psi^{(1)}_{i+1,j}, \widehat{C}^{(1)}_{i+1/2,j}) - F(\Psi^{(1)}_{i-1,j}, \Psi^{(1)}_{i,j}, \widehat{C}^{(1)}_{i-1/2,j})] \\ & - \quad [F(\Psi^{(1)}_{i,j}, \Psi^{(1)}_{i,j+1}, \widehat{C}^{(1)}_{i,j+1/2}) - F(\Psi^{(1)}_{i,j-1}, \Psi^{(1)}_{i,j}, \widehat{C}^{(1)}_{i,j-1/2})], \end{aligned} \tag{70}$$

where the caret above the remapped variable indicates that the variable has been limited to impose monotonicity.

Finally, $\widehat{\psi}^{(+)}_{i,j}$ may be recovered by dividing (70) by $V^{(+)}$.

2.5 Infinite Gauge extension of MPDATA

The basic form of MPDATA presented in previous sections allows the transportation of scalar fields that are not required to be non-negative or non-positive. This is permissible due to the inclusion of absolute values of ψ in the calculation of (22), (23) for the pseudo velocities. This feature arose due to the relationship detailed in Reference [14]:

$$\frac{1}{\psi}\frac{\partial \psi}{\partial x^I} \equiv \frac{1}{2\mu}\frac{1}{(\psi^2)^\mu}\frac{\partial (\psi^2)^\mu}{\partial x^I}\bigg|_{\mu=1/2} = \frac{1}{|\psi|}\frac{\partial |\psi|}{\partial x^I}, \tag{71}$$

where the superscript I denotes the spatial direction so that

$$A^{(1)} \triangleq \frac{1}{\psi}\frac{\partial \psi}{\partial x^{I=1}}, \qquad B^{(1)} \triangleq \frac{1}{\psi}\frac{\partial \psi}{\partial x^{I=2}}. \tag{72}$$

An alternative approach to deal with the transportation of fields with variable signs is achieved by the infinite gauge option of MPDATA. This option linearises

MPDATA around an arbitrary large constant [3, 6]. Performing this linearisation leads to a two-pass scheme that differs to the basic scheme only in the calculation of the pseudo velocity and execution of the second Upwind pass. The calculation of the pseudo velocities is altered due to the formulation of the numerical estimates of the gradients (22) and (23). The linearised formulation removes the application of absolute values, and replaces each value of ψ in the denominator by unity to become:

$$A^{(1)} = \frac{1}{2}\left(\psi^{(1)}_{i+1,j} - \psi^{(1)}_{i,j}\right), \tag{73}$$

$$B^{(1)} = \frac{1}{8}\left(\psi^{(1)}_{i+1,j+1} + \psi^{(1)}_{i,j+1} - \psi^{(1)}_{i+1,j-1} - \psi^{(1)}_{i,j-1}\right). \tag{74}$$

The execution of the second Upwind pass is altered by replacing each ψ argument in the flux function (3) by unity so that the flux function becomes:

$$F\left(1, 1, U\right) \equiv U. \tag{75}$$

The remapping extension is updated in a similar fashion, with each ψ in (73),(74) replaced by Ψ, and U in (75) by C.

The infinite gauge option is particularly useful as it preserves the gradients across zero for fields of variable sign [6]. This option has been found to perform better than the basic MPDATA advection scheme at capturing shocks, but unlike the basic MPDATA scheme, it is neither sign preserving nor monotonic. Monotonicity may be enforced as per the basic MPDATA scheme by again applying the FCT concept. The non-oscillatory scheme applied to the infinite gauge option differs to the basic FCT application in the calculation of ξ values, and within the limiter itself.

The ξ values differ due to the flux function used in the accumulation of fluxes in the denominators of (62) and (62). These fluxes are calculated using (75) so

that again the values of ψ are replaced by unity. The limiter now changes on the same basis. The values of ψ in (66) are also replaced by unity so that the values of $\left[sgn(\pm\psi^{(1)})\right]^{+}$ are now explicit. These values operate as switches to deal with fields which contain positive and negative values. Such switches are no longer required as the fields are now taken over an arbitrarily large constant which means the field will not cross zero in the calculation. The limiting function for MPDATA remapping will then become:

$$\begin{aligned} \widehat{C}^{(1)}_{i+1/2,j} &= \left[C^{(1)}_{i+1/2,j}\right]^{+} min(1, \xi^{IN}_{i+1,j}, \xi^{OUT}_{i,j}) \\ &+ \left[C^{(1)}_{i+1/2,j}\right]^{-} min(1, \xi^{OUT}_{i+1,j}, \xi^{IN}_{i,j}). \end{aligned} \tag{76}$$

The limited pseudo velocities are utilised to update the variable onto the post-remap grid using the Upwind step given as:

$$\widehat{\Psi}^{(+)}_{i,j} = \Psi^{(1)}_{i,j} - \left[\widehat{C}^{(1)}_{i+1/2,j} - \widehat{C}^{(1)}_{i-1/2}\right] - \left[\widehat{C}^{(1)}_{i,j+1/2} - \widehat{C}^{(1)}_{i,j-1/2}\right]. \tag{77}$$

Further details of the infinite gauge option the proposed MPDATA remapping are available in [24].

2.6 MPDATA Second-Order Filtering Option

The second-order filtering option of MPDATA [6] allows a controlled application of additional diffusion within the MPDATA based schemes. By design, MPDATA relies on the iterative application of the Upwind scheme, where subsequent iterations compensate for the implicit viscosity of the preceding steps. MPDATA therefore bears an analogy to generalised similarity models, where an estimate of the full unfiltered Navier-Stokes velocity (that enters the subgrid-scale stress tensor) is obtained by an approximate inversion of the filtering operation, i.e. deconvolution [6]. Building upon this concept, and in the spirit of the Flux Corrected Transport methods detailed in Section 2.4.1, additional diffusion may be

explicitly added to the first Upwind iteration to remove oscillations in the first-order solution. The second Upwind iteration then compensates the truncation error of the first step, which includes the added dissipation.

Additional diffusion is added to the flux functions in (34) by a small explicit flux so that the first pass becomes

$$\begin{aligned}\Psi_{i,j}^{(1)} = \; & \Psi_{i,j}^{(-)} - \Big[F\left(\Psi_{i,j}^{(-)}, \Psi_{i+1,j}^{(-)}, C_{i+1/2,j}\right) - \beta_{i+1/2,j}\left(\Psi_{i+1,j}^{(-)} - \Psi_{i,j}^{(-)}\right) \\ & - F\left(\Psi_{i-1,j}^{(-)}, \Psi_{i,j}^{(-)}, C_{i-1/2,j}\right) - \beta_{i-1/2,j}\left(\Psi_{i,j}^{(-)} - \Psi_{i-1,j}^{(-)}\right)\Big] \\ & - \Big[F\left(\Psi_{i,j}^{(-)}, \Psi_{i,j+1}^{(-)}, C_{i,j+1/2}\right) - \beta_{i,j+1/2}\left(\Psi_{i,j+1}^{(-)} - \Psi_{i,j}^{(-)}\right) \\ & - F\left(\Psi_{i,j-1}^{(-)}, \Psi_{i,j}^{(-)}, C_{i,j-1/2}\right) - \beta_{i,j-1/2}\left(\Psi_{i,j}^{(-)} - \Psi_{i,j-1}^{(-)}\right)\Big], \end{aligned} \tag{78}$$

where β is a small positive coefficient. With $\delta t \propto \delta x$, the explicit diffusion enters (78) as an $\mathcal{O}(\delta x)$ correction, whereupon its reversal in the corrective step leaves an $\mathcal{O}(\delta x^2)$ residual; see [25] for a thorough exposition. The pseudo Courant number calculations (35) and (37) become

$$\begin{aligned} C_{i+1/2,j}^{(1)} \; \equiv \; & \left(\left|C_{i+1/2,j}\right| - \left(C_{i+1/2,j}\right)^2 + 2\beta_{i+1/2,j}\right) A^{(1)} \\ - \; & C_{i+1/2,j}\bar{C}_{i+1/2,j}B^{(1)}, \end{aligned} \tag{79}$$

and

$$\begin{aligned} C_{i,j+1/2}^{(1)} \; \equiv \; & \left(\left|C_{i,j+1/2}\right| - \left(C_{i,j+1/2}\right)^2 + 2\beta_{i,j+1/2}\right) B^{(1)} \\ - \; & \bar{C}_{i,j+1/2}C_{i,j+1/2}A^{(1)}, \end{aligned} \tag{80}$$

respectively.

Within the second-order filtering option, $\beta = 0.02$ is the default value, but may vary in space or be set to zero upon the detection of a shock (discontinuity). The effective level of diffusion is an order of magnitude lower than that reported in [22]. Similarly to MPDATA, this treatment is fully multidimensional.

2.7 Multiple Pass MPDATA

The basic MPDATA scheme, and the non-oscillatory and infinite gauge options, use two passes of the first-order Upwind scheme to achieve second-order accuracy. This is achieved by compensating the truncation error introduced by the first-order scheme with a second pass of the same first-order scheme. In this case, the diffusive error introduced in the first pass is transformed into an advection term to be removed in the second pass. In much the same way, the second pass will also introduce a diffusive error term in its application, so that the second-order truncation error will not be completely removed.

The second-order truncation error may be further compensated by repeating the process of calculating pseudo velocities to compensate the errors introduced in the previous pass. The pseudo velocity calculation will remain identical, with the exception that values from a given pass $^{(p)}$ being replaced by the values at pass $^{(p+1)}$. There is therefore no limit to the number of passes that may be applied, however subsequent passes will only reduce the magnitude of the error, with the solution maintaining second-order accuracy. With an increase in the number of iterations performed, the imposed computational cost will be greater than the benefit in solution accuracy. A maximum number of four passes has been shown to be practical in terms of accuracy and computational cost [13].

Further options are available for MPDATA which may improve accuracy ("Third-Order-Accurate") or computational efficiency (Recursive pseudo velocities) [3]. Such options are not within the focus of this work.

3 Remapping Test Cases

To test the performance of the MPDATA based remapping scheme, a number of simple test cases are proposed for a single scalar variable. These test cases allow an examination of the conservation, symmetry preservation and accuracy properties for both MPDATA remapping, and for a comparison with the van Leer based remapping scheme. Properties of the MPDATA options are also looked at.

3.1 Fixed Mesh Test Cases

A standard solid body rotation test [26, 27] is performed to evaluate the performance of the MDPATA based remapping scheme.

In order to evaluate the MPDATA based remapping scheme, the test is executed using both MPDATA advection and MPDATA based remapping. MPDATA advection uses the velocity field to determine the direction of material exchange, whereas MPDATA remapping uses the velocity field to create overlap volumes based upon the positions of the nodes before and after the computational time step. Nodal positions are not updated. This comparison allows the impact of the additional terms in the swept region overlap volume calculation to be identified, as discussed in Section 2.3.2. Two van Leer based remapping schemes are also included to compare the performance of the current remap methods to the MPDATA based remap scheme. The van Leer based schemes are extended to multiple dimensions by isotropic [2] and Strang split [11] remapping. This test case will primarily allow a comparison of the multidimensional MPDATA scheme compared to the dimensionally extended van Leer based schemes.

The solid body rotation test, [26], is a classical advection test modified for remapping. Although the test does not update the spatial location of the nodes which would form meshes akin to the post-Lagrangian and post-remap meshes,

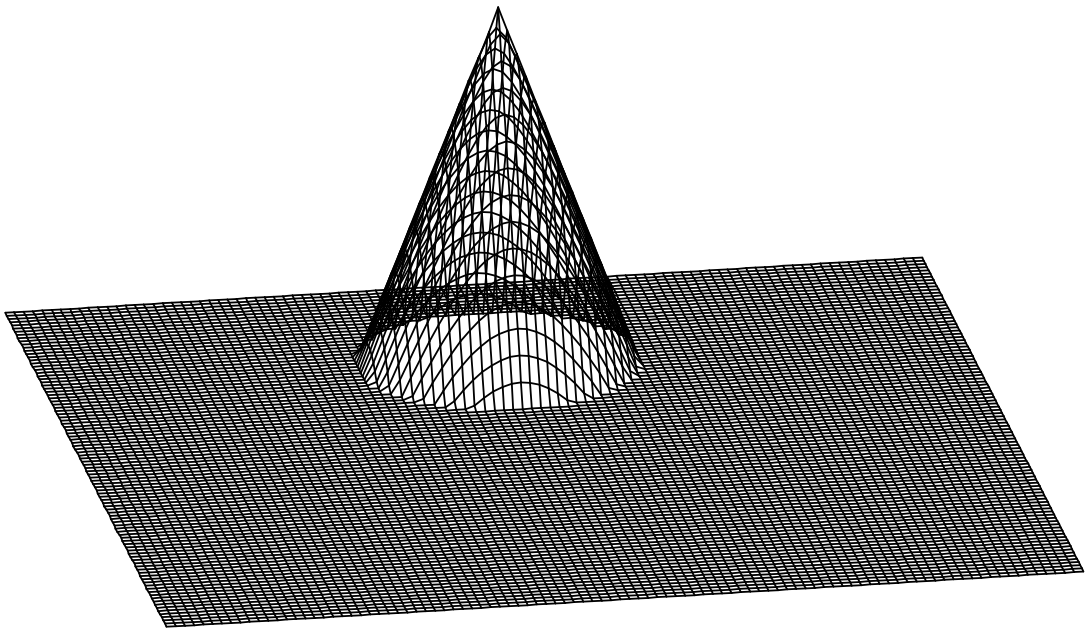

Figure 5: Initial cone for solid body rotation test.

the nodal velocities are sufficient to calculate the swept region overlap volumes.

A cone is placed on an orthogonal grid of size $[0,1]\times[0,1]$. The cone is initially located at $(0.75, 0.50)$ with a height of four units and base radius of 0.15. The cone is then rotated about the point $(0.50, 0.50)$ with angular velocity $\omega = 0.1$ and velocity components $(u, v) = -\omega\,(y - y_0, x - x_0)$. Six rotations of the cone are completed to fully test the performance of the remapping methods. When simulated on a mesh with 10,000 square elements, the six rotations are performed with a computational time step of $\delta t = 0.1$. The initial condition of the cone is shown in Figure 5.

To highlight the importance of monotonicity compared to sign preservation, the test is undertaken with a positive background of one unit. Comparisons of the cone structures after six rotations using the basic, non-oscillatory and non-

oscillatory infinite gauge MPDATA advection and remapping schemes are shown in Figs. 6, 7 and 8.

The positive definite aspect of MPDATA is highlighted by the oscillations appearing in the basic option of MPDATA, shown in Figs. 6. The benefit of the non-oscillatory option of MPDATA is clearly shown by the removal of oscillations at the base, although conversely, the suppression of over shoots at the peak is also highlighted by a small increase in smoothing. The non-oscillatory infinite gauge MPDATA scheme shows the best result. The results are qualitatively similar for both the advection and remapping MPDATA schemes. The conclusions are highlighted by Table 1 which details the maximum and minimum values of the transported scalar after six rotations. All schemes with monotonicity conditions retain the correct unit background value as the minimum, whereas the sign preserving basic MPDATA schemes drop below the exact minimum value. Both the finite difference advection and volume co-ordinate remapping versions of MPDATA retain a more accurate maximum value compared to the isotropic van Leer method. In all MPDATA remapping schemes, the maximum value is reduced compared to the advection value, which is an anticipated manifestation of the additional terms included in the swept region overlap volumes compared to the exact Courant number.

The isotropic and Strang split van Leer remapping results are shown in Figures 9 and 10, respectively. Both options show significant deformation of the cone. The isotropic van Leer scheme results in a cone that has been unrealistically deformed by elongation in the radial direction, while the top of the cone has been flattened. The elongation is a result of the angular velocity profile requiring transport between diagonal elements and thus introducing corner coupling errors in the remapping. The flattening of the cone's peak likely results from the construction of one dimensional monotonic slopes, as detailed in Section 2.2. As a

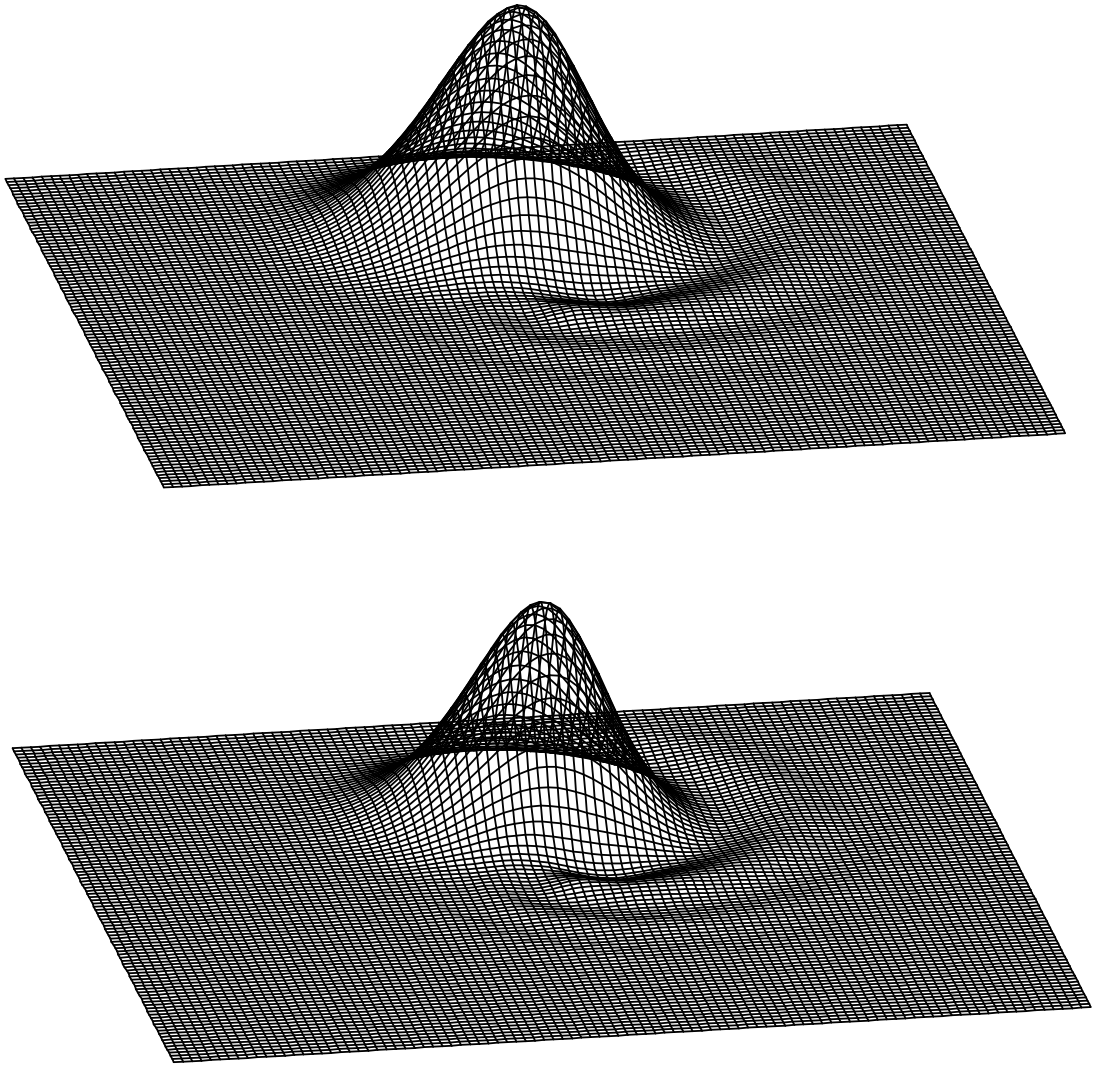

Figure 6: Basic MPDATA. Top: advection, bottom: remapping.

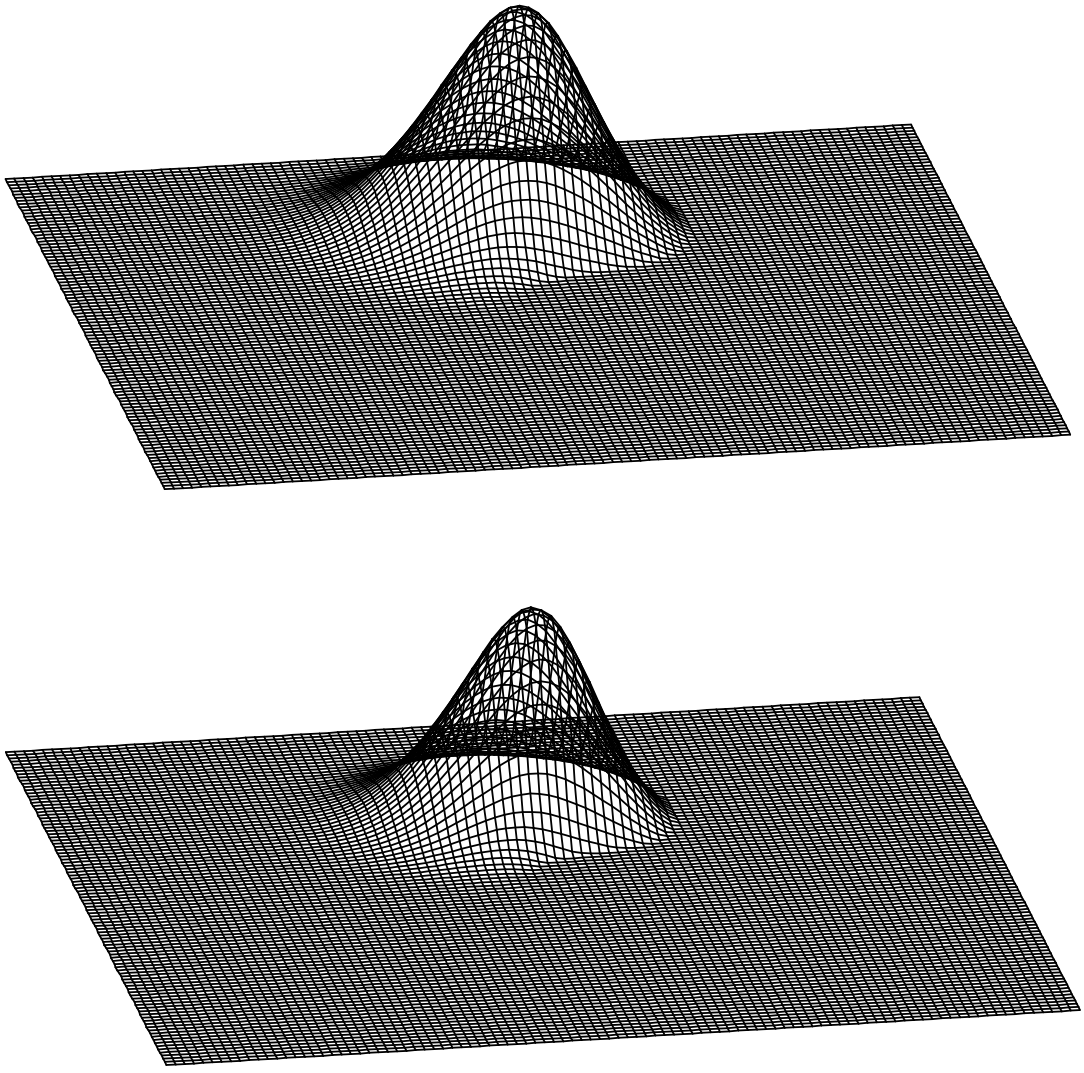

Figure 7: Non-oscillatory MPDATA. Top: advection, bottom: remapping.

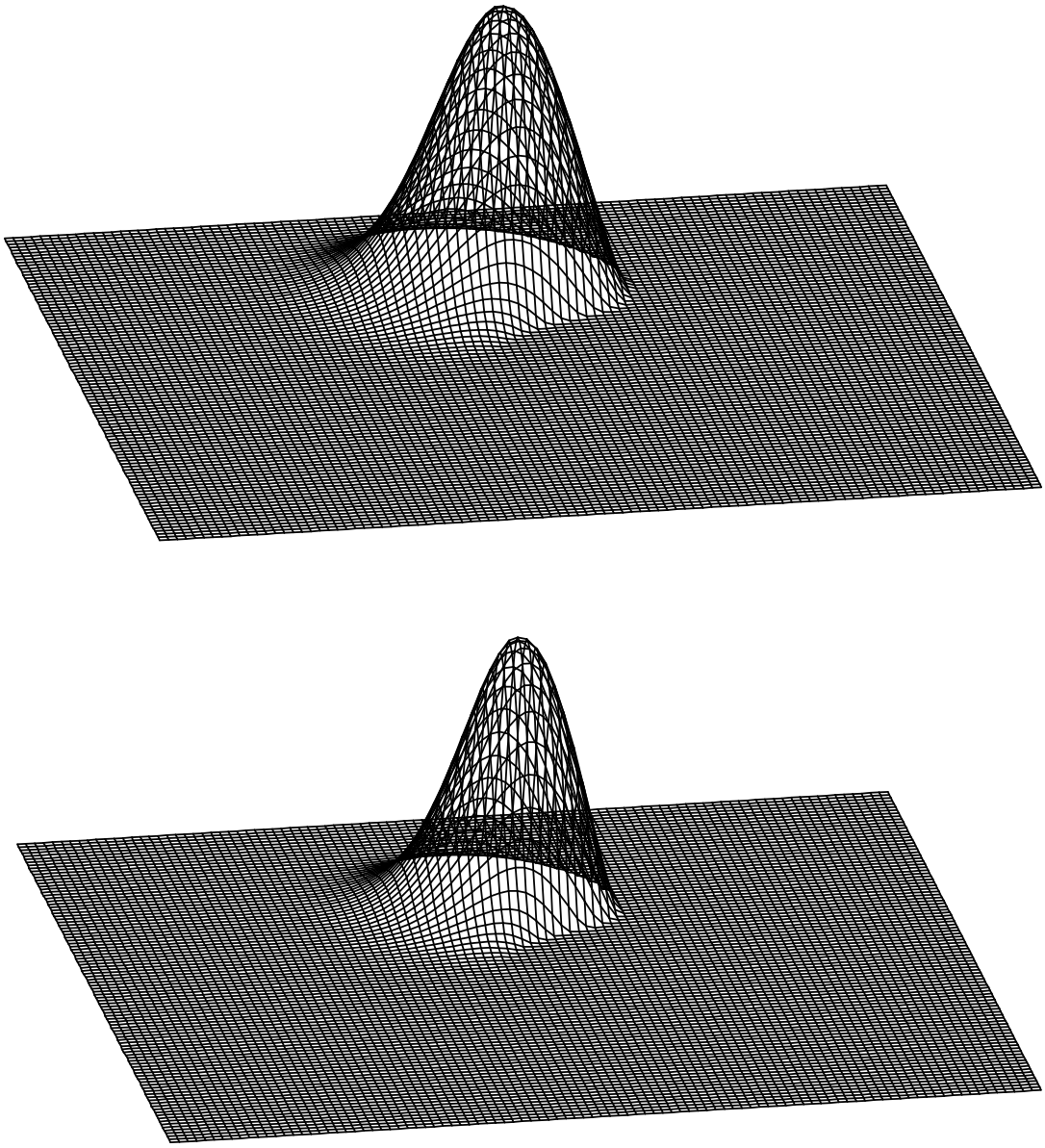

Figure 8: Non-oscillatory infinite gauge MPDATA. Top: advection, bottom: remapping.

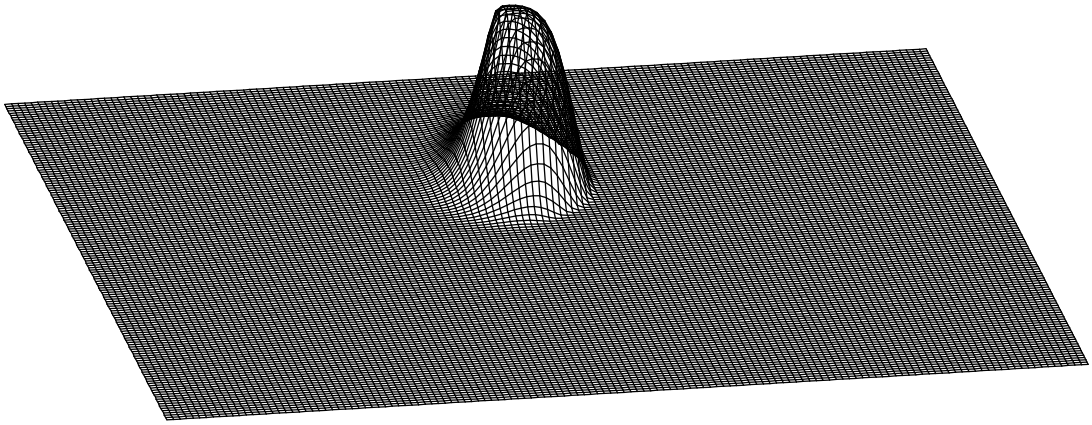

Figure 9: Solid body rotation test - van Leer isotropic remapping. Note: due to the strong deformation of the cone, a larger computational grid is required.

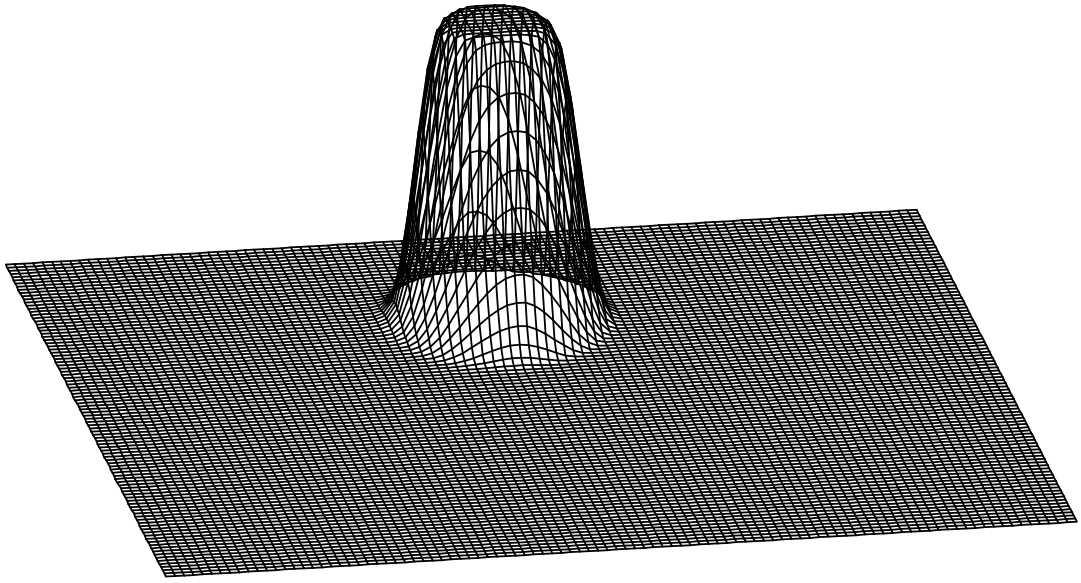

Figure 10: Solid body rotation test - van Leer Strang Split remapping.

result, the correct maximum and minimum values surrounding the element may not be employed if they lie in a diagonal element. An analogous result is obtained by disabling cross terms in MPDATA, see [12, 13] for an illustration and thorough discussion. Due to the significant elongation seen in the cone, the isotropic van Leer solution requires a reduced time step of $\delta t = 0.05$, and a larger domain of $[0, 1.4] \times [0, 1.4]$ so that the solution does not impinge upon the computational boundary. The solution of the van Leer scheme implemented with Strang splitting shows good preservation of symmetry, but exhibits severe deformation, and after six rotations, resembles a cylinder. In this case, the rate of corner transport is increased, however the one dimensional nature of the monotonic slopes still results in a flattened peak to the cone. By the design of the Strang splitting approach, this solution uses average normal displacement overlap volumes.

Isolines of the cone remapped through six rotations using van Leer isotropic and Strang splitting, and the (non-oscillatory) infinite gauge MPDATA are shown in Figure 11. This comparison highlights the overall improved performance of the MPDATA based schemes compared to the van Leer implementations. While the Strang split van Leer scheme shows reasonable preservation of the circular contours, the contours are too close together, indicating a sharp slope. The infinite gauge MPDATA solution shows a satisfactory preservation of the circular shape, with a contour interval similar to the exact solution. Only a slight bias to the direction of flow is visible, and is ideally undesirable.

Both the van Leer and MPDATA based schemes are theoretically second-order accurate for advection. An asymptotic mesh convergence test is carried out to examine the accuracy of the schemes for remapping. The convergence test repeats the solid body rotation test on a sequence of meshes with increasing spatial and temporal resolution. For each solution, the L_2 error norm is calculated. The ratio between the L_2 values for consecutive meshes indicates the accuracy of the remap-

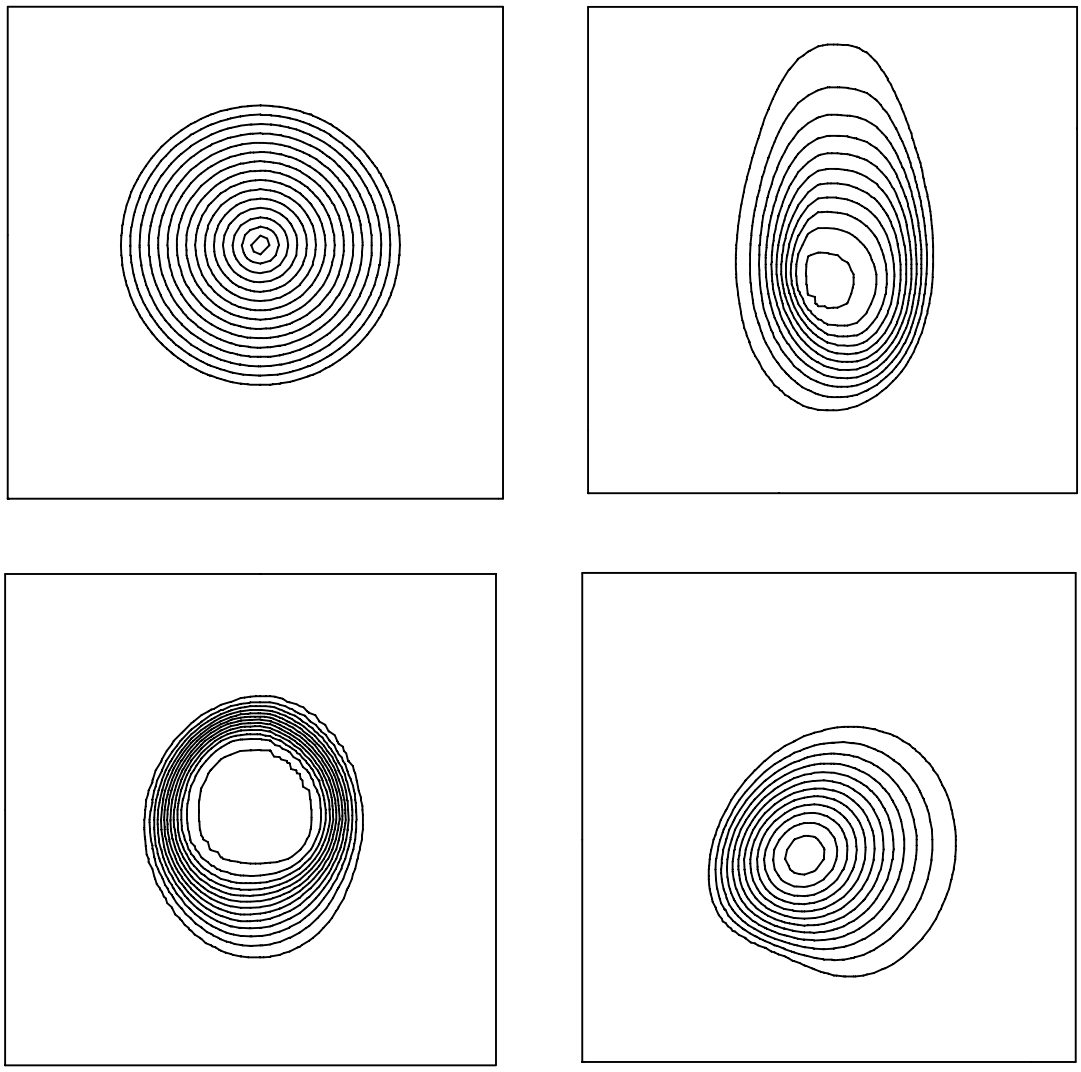

Figure 11: Isolines of a rotating cone (only a quarter of the domain is shown). The contour interval is 0.25 and minimum contour level, 1.0. Upper left plate: Exact solution. Upper right and lower left plates: van Leer with isotropic and Strang split remapping respectively. Lower right plate: Infinite Gauge MPDATA remapping.

Scheme	Maximum	Minimum
Exact	5.00	1.00
Basic MPDATA advection	3.55	0.86
Non-oscillatory MPDATA advection	3.53	1.00
Infinite Gauge MPDATA advection	4.25	1.00
Basic MPDATA remapping	3.36	0.86
Non-oscillatory MPDATA remapping	3.34	1.00
Infinite Gauge MPDATA remapping	4.14	1.00
Isotropic van Leer remapping	3.80	1.00
Strang split van Leer remapping	4.31	1.00

Table 1: Summary data for solid body rotation test case.

ping as illustrated in Table 2. The van Leer schemes deform the cone on finer meshes, with the Strang split convergence behaving erratically and the isotropic convergence deteriorating towards first-order. Conversely, the MPDATA scheme moves closer to second-order convergence (indicated by a value of four). Although the MPDATA remapping scheme does not fully attain second-order convergence, it should be noted that full second-order convergence has been documented for MPDATA advection [5]. This is indicative of small losses in accuracy introduced by both the FCT option, as discussed in [23], and the implementation of volume co-ordinates.

Overall, the MPDATA based remapping schemes retain the conical shape much more accurately than the van Leer based scheme due to the multidimensionality of the MPDATA scheme. The position of the cone is held well in both cases, and although the van Leer scheme maintains the level of the peak better than the basic and non-oscillatory option of MPDATA, the non-oscillatory infi-

Δx	Isotropic van Leer	Strang split van Leer	Infinite Gauge MPDATA
0.02	–	–	–
0.01	2.85	3.91	2.20
0.005	2.11	1.68	3.17
0.0025	2.20	3.03	3.37

Table 2: Asymptotic mesh convergence data for the solid body rotation remapping. The first column lists spatial resolutions Δx for consecutive meshes, the remaining columns list the corresponding ratios of the solution error norms for the remapping schemes.

nite gauge option gives the best result in terms of position, shape and maximum and minimum values. Due to the lack of monotonicity preservation in the basic MPDATA scheme only the non-oscillatory options represent acceptable solutions. The basic form of MPDATA will no longer be considered in further tests.

3.2 Prescribed Mesh Movement Test Cases

A key aspect of the ALE method is to remap the post-Lagrangian solution onto a relaxed grid which will have improved geometric properties. The prescribed mesh movement test cases proposed by Margolin and Shashkov [15, 16] are designed to test the performance of the remapping schemes for this purpose.

The following test cases remap initial distributions of a positive scalar field on to a series of meshes whose nodal positions are chosen to move in a defined manner. There is no associated velocity field which will move the nodes of the computational mesh. Instead the nodal positions for each intermediate mesh are known by a given function. The scalar field is then mapped from a mesh at time t^n to the prescribed mesh at time t^{n+1}, with the overlap volumes ΔV calculated

using the arbitrary polygon calculation (30) with the two nodal positions of a cell edge on the mesh at times t^n and t^{n+1}. The nodal positions are specified in such a way that the positions of each node on the subsequent grid do not exceed the adjacent cell. This ensures that the overlap volumes do not cover more than one element.

The mesh movement is defined by a tensor product motion. The tensor product grids are generated in the domain $[0,1] \times [0,1]$ using the functions

$$x(\xi,\eta,t) = (1-\alpha(t))\xi + \alpha(t)\xi^3, \quad y(\xi,\eta,t) = (1-\alpha(t))\eta + \alpha(t)\eta^2, \tag{81}$$

$$\alpha(t) = \frac{sin(4\pi t)}{2}, \tag{82}$$

with $0 \leq \xi \leq 1,\ \ 0 \leq \eta \leq 1,\ \ 0 \leq t \leq 1$.

The sequence of meshes $\left\{x_{i,j}^n\right\}$ is then given by

$$x_{i,j}^n = x(\xi_i,\eta_j,t^n), \qquad y_{i,j}^n = y(\xi_i,\eta_j,t^n), \tag{83}$$

with

$$\begin{aligned} t^n &= \tfrac{n}{n_{max}}, \quad n = 0,\ldots,n_{max}, \\ \xi_i &= \tfrac{i-1}{i_{max}-1}, \quad i = 1,\ldots,i_{max}, \\ \eta_j &= \tfrac{j-1}{j_{max}-1}, \quad j = 1,\ldots,j_{max}. \end{aligned}$$

The tensor product movement has the effect of skewing the mesh from an initially regular grid ($t = t^0 = 0, \alpha(t) = 0$) to one corner of the domain, back to the opposite corner and back to a final regular mesh ($t = t^n = 1, \alpha(t) = 0$). Two intermediate grids are shown in Fig. 12.

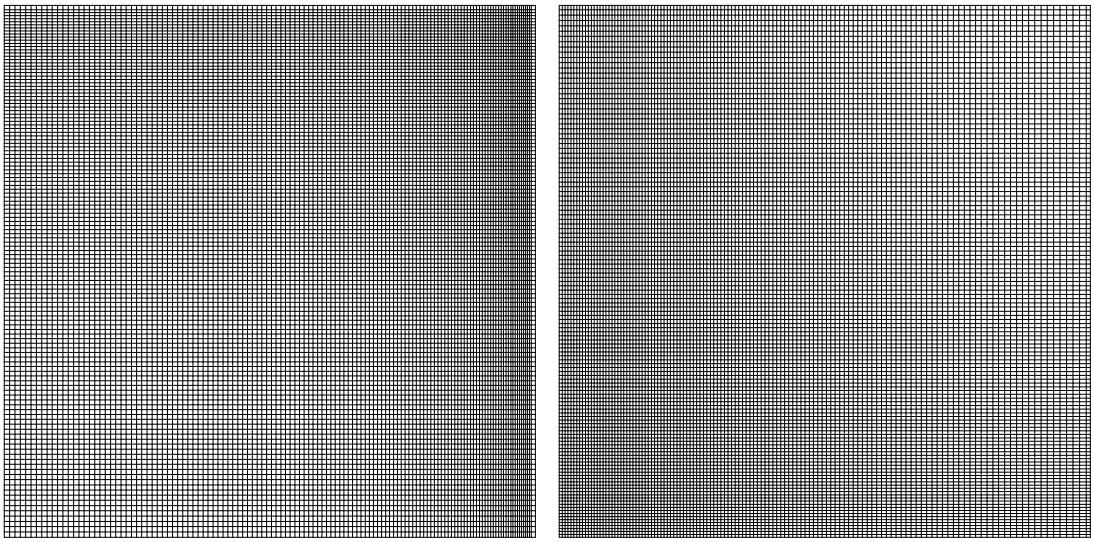

Figure 12: Intermediate tensor meshes. Left: $n = 128$, right: $n = 512$, $n_{max} = 640$.

3.2.1 Non-negative Scalar Tests

Utilising the prescribed grid motion, three non-negative scalar field distributions are remapped. The first distribution is a smooth function termed the 'sine' test.

$$\rho(x, y) = 1 + sin(2\pi x)sin(2\pi y). \tag{84}$$

The second distribution places a cone at the centre of the mesh termed the 'peak' test.

$$\rho(x, y) = \begin{cases} 0 & \text{if } r > 0.25, \\ max(0.001, 4(r - 0.25)) & \text{if } r \leq 0.25, \end{cases} \tag{85}$$

where $r = \sqrt{(x - 0.5)^2 + (y - 0.5)^2}$.

The final distribution is a discontinuous oblique shock function termed the

'shock' test.

$$\rho(x,y) = \begin{cases} 1 & \text{if } y > (x-0.4)/0.3, \\ 0 & \text{if } y \leq (x-0.4)/0.3. \end{cases} \tag{86}$$

The mapped distribution for each test on a grid specified by $i_{max} = j_{max} = 128$, $n_{max} = 640$ are shown for the isotropic van Leer, non-oscillatory and non-oscillatory infinite gauge options of MPDATA in Figs. 13-16.

It can be seen that both options of MPDATA perform comparably, giving results consistent with the exact values (84-86), and appear to improve on the MPDATA inspired Positivity-preserving Error Compensation Algorithm and the BarthJespersen solutions given in [15]. The vertex and base of the peak distribution retain a sharper definition with the non-oscillatory infinite gauge option. The oblique shock distribution clearly shows an advantage of the infinite gauge option. For this option, the gradient of the scalar distribution across the shock matches closely to the desired theoretical, discontinuous shock. The non-oscillatory option of MPDATA also successfully maps the oblique shock, however it can be seen that the mapped result contains more diffusion. The steep gradient featured in the remapped infinite gauge shock agrees with published results for shock treatment with the infinite gauge option, see [14].

The remapping results using the van Leer based scheme for all distributions exhibit erroneous ripples forming across the features. In each distribution the ripples appear diagonally through the domain. This would indicate that the primary cause of the ripples is due to a lack of information being passed between elements that only share a common node, i.e. corner transport. This is a feature of a one dimensional scheme being extended to further dimensions, with each one-dimensional sweep only taking in data from the sweep direction. The lack of these ripples in the MPDATA schemes is likely to be because of the designed

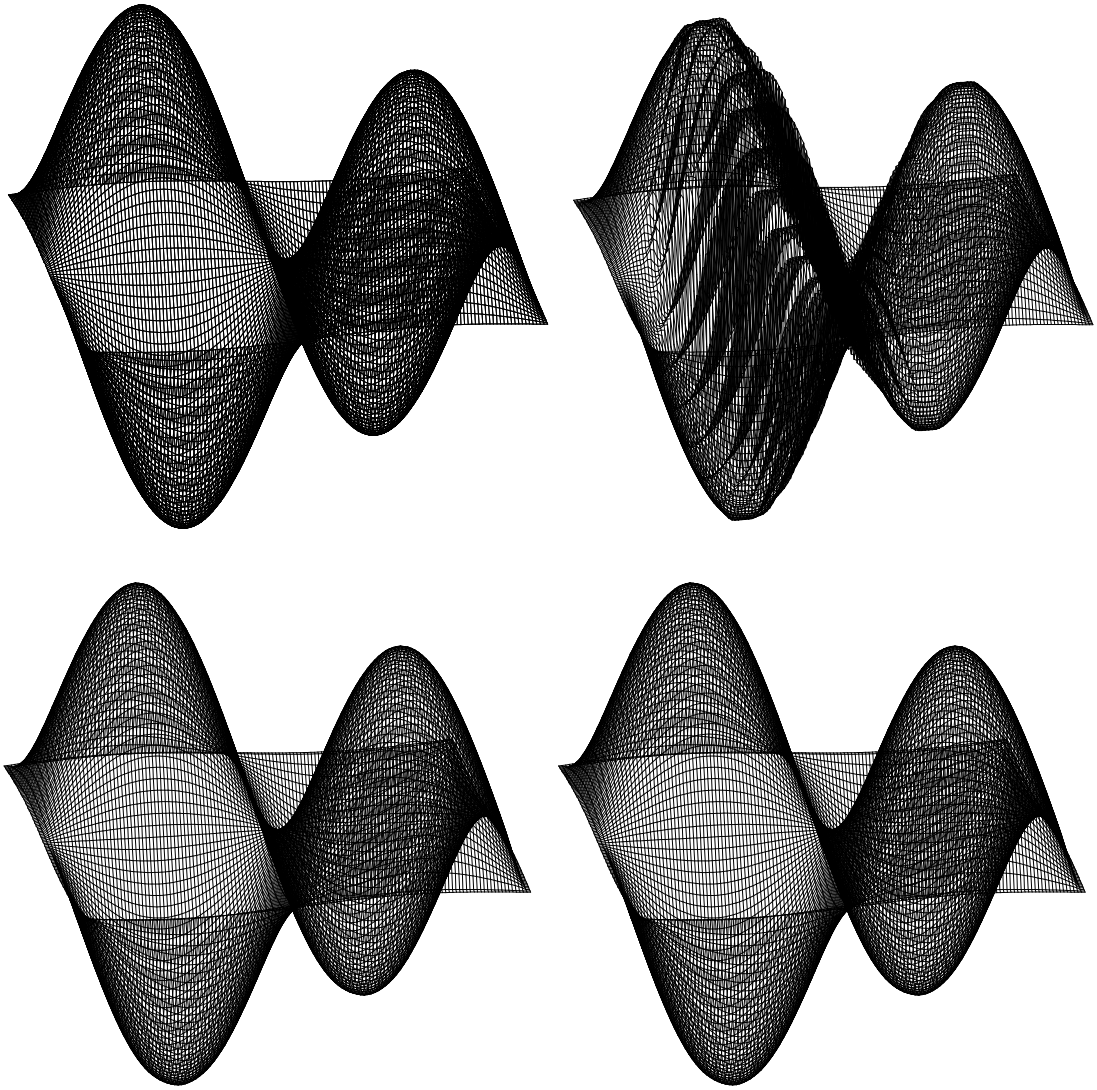

Figure 13: Prescribed mesh motion remapping with sine distribution. Top left: exact, top right: isotropic van Leer, bottom left: non-oscillatory MPDATA, bottom right: infinite gauge MPDATA.

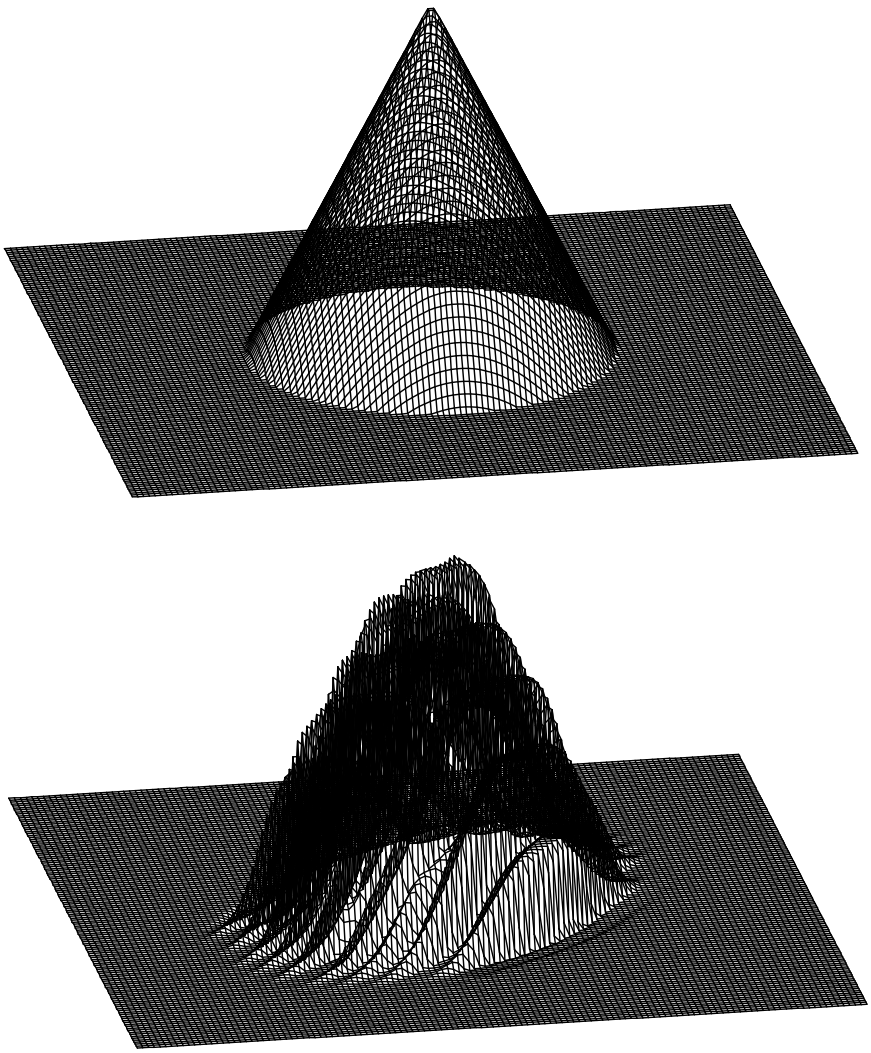

Figure 14: Prescribed mesh motion remapping with peak distribution. Top: exact, bottom: isotropic van Leer.

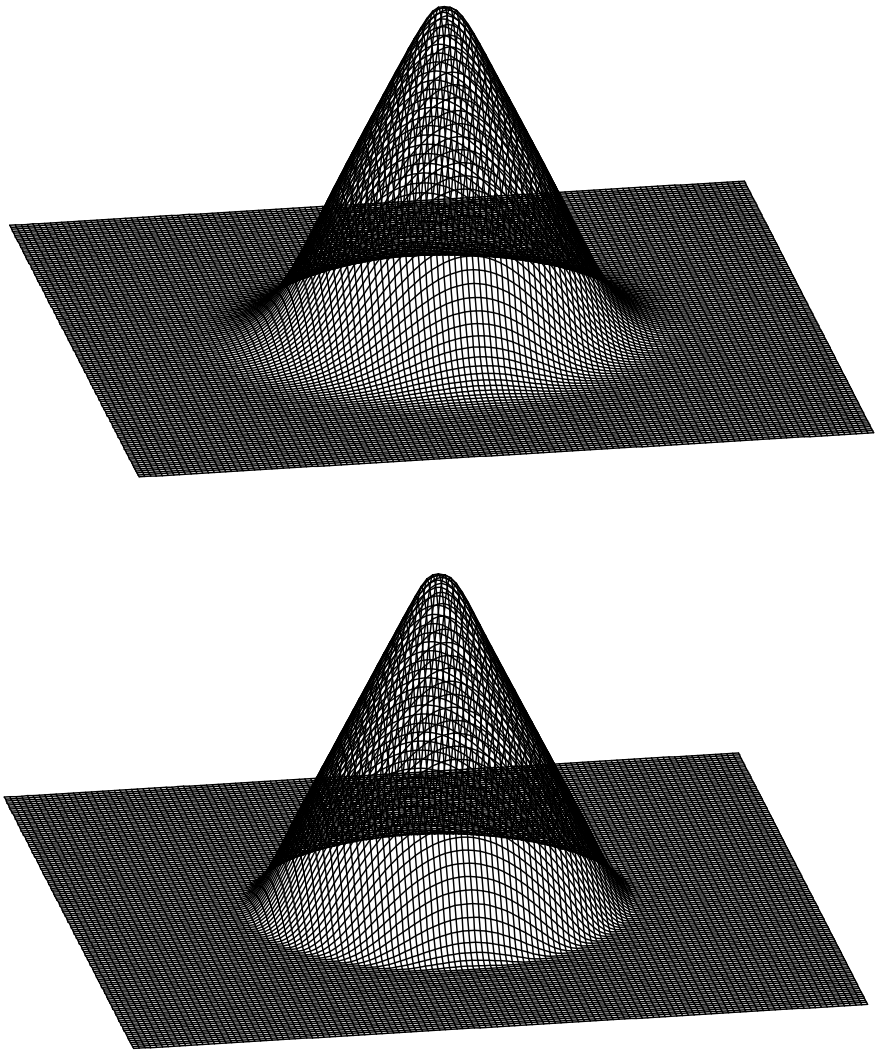

Figure 15: Prescribed mesh motion remapping with peak distribution. Top: non-oscillatory MPDATA, bottom: infinite gauge MPDATA.

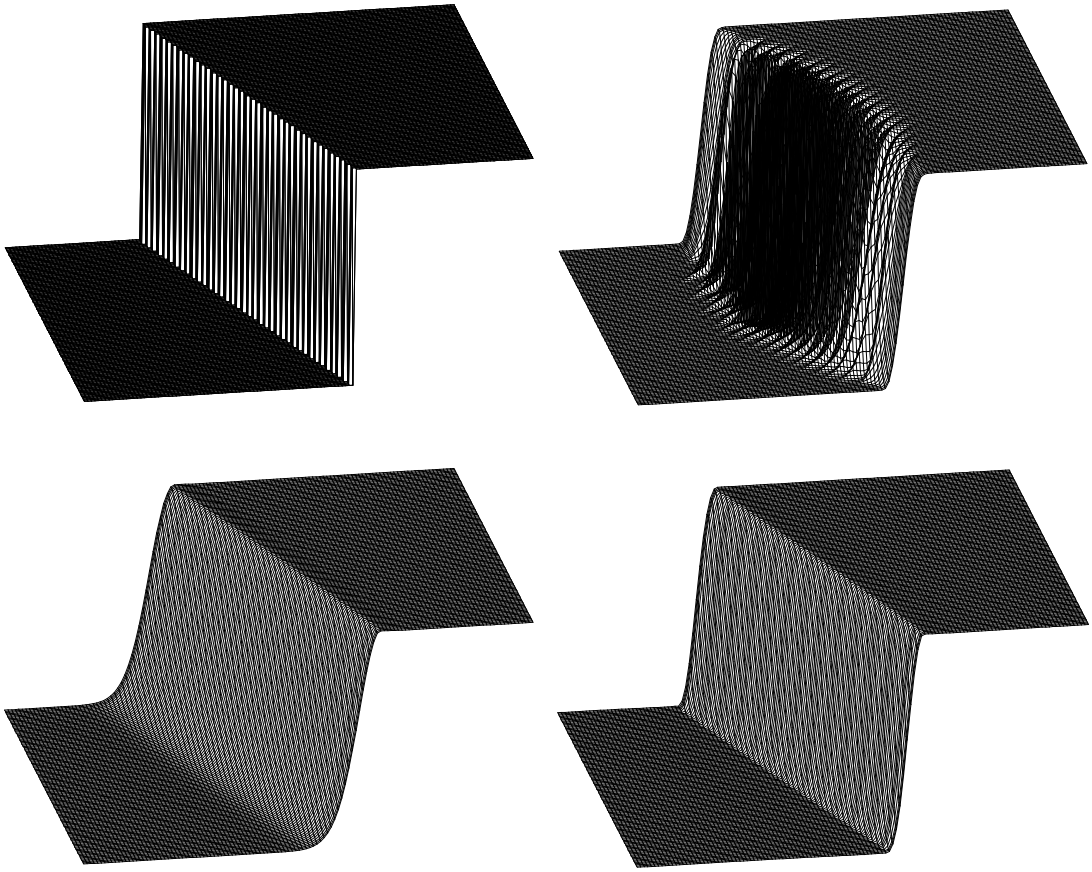

Figure 16: Prescribed mesh motion remapping with oblique shock distribution. Top left: exact, top right: isotropic van Leer, bottom left: non-oscillatory MPDATA, bottom right: infinite gauge MPDATA.

multidimensionality of the MPDATA scheme, with information being drawn upon both the normal and parallel directions when exchanging material across each element edge. This conclusion is supported by a modification to the oblique shock distribution. By aligning the shock to the underlying computational mesh, such that

$$\rho(x,y) = \begin{cases} 1 & \text{if } x > 0.5, \\ 0 & \text{if } x \leq 0.5. \end{cases} \tag{87}$$

corner transport is removed, and the van Leer remapping is able to produce the correct result. The exact, van Leer and infinite gauge solutions to the modified shock distribution is shown in Figure 17. The non-oscillatory MPDATA solution is omitted due to similarities with the infinite gauge solution.

3.2.2 Sign Changing Scalar Distribution

Although the non-oscillatory, and infinite gauge options of MPDATA perform comparably well in the preceding remapping tests, it can be seen that in both the prescribed mesh motion and fixed mesh test cases, the infinite gauge option consistently provides a more accurate solution. Further benefits of using the infinite gauge option can be seen by an modification of the 'sine' distribution (84), such that

$$\rho(x,y) = sin(2\pi x)sin(2\pi y), \tag{88}$$

now features a change in sign within the scalar distribution.

The significance of this modification relies upon the original derivation of MPDATA being aimed at non-negative scalar and vector fields. The algorithm was later extended to positive or negative fields by the use of absolute values in the calculations of derivatives used in the pseudo velocities, cf. Section 3.2

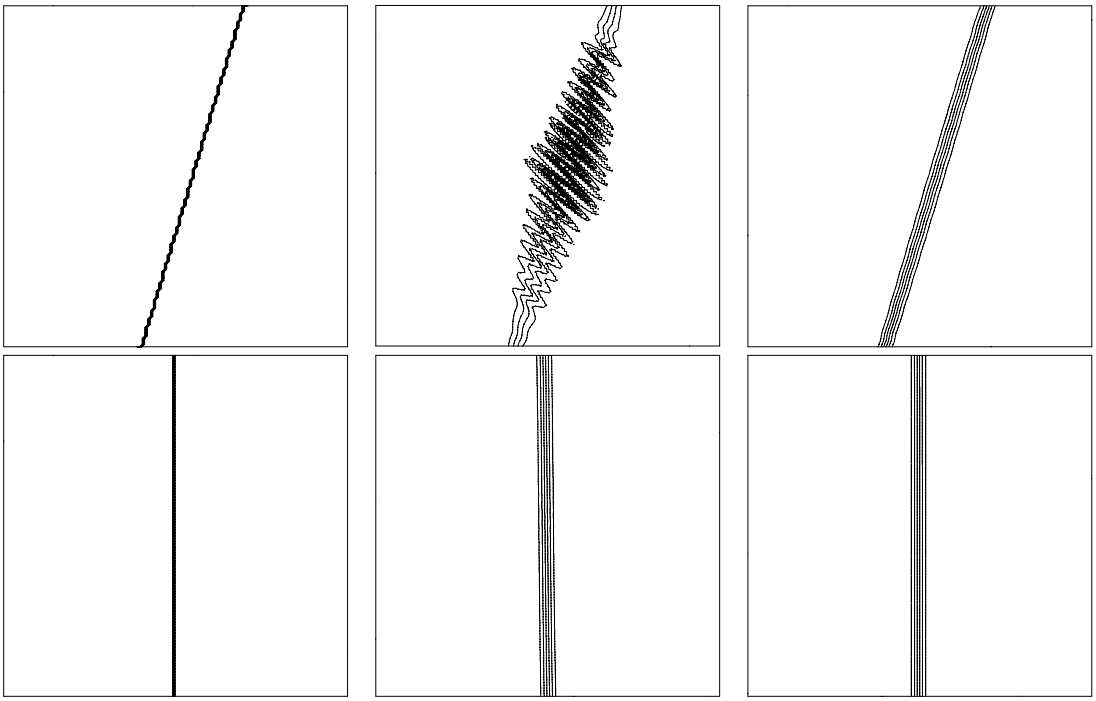

Figure 17: Prescribed mesh motion remapping with the oblique (top) and modified shock (bottom) distribution. Left: exact, centre: isotropic van Leer, right: infinite gauge MPDATA.

in [3]. However, when using absolute values in some test cases that feature fields of varying sign, aspects of the solution may not be accurate. For example, if $\rho_{i,j} \approx -\rho_{i+1,j}$ then $\partial\rho/\partial\mathbf{x} \rightarrow \pm\infty$ as $\rho_{i,j}$ increases in magnitude with $-\rho_{i+1,j}$, whereas $\partial\left|\rho\right|/\partial\mathbf{x} \rightarrow 0$.

The infinite gauge option of MPDATA however is generalised to fields of varying sign by linearising the algorithm around an arbitrarily large constant, as detailed in Section 2.5. As a result, the scalar or vector field is modified to be effectively non-negative, which in turn removes the need to exploit absolute values in derivatives.

Contours of the changing sign sine distribution are shown in Figure 18. It can be seen that the van Leer remapping scheme continues to introduce the undesired ripples into the solution, whereas the MPDATA based remapping schemes produce solutions that are close to the exact solution. The effect of using absolute values in the calculation of derivatives can be seen however, by an increase in the gap between the contours as the distribution crosses zero. This effect is highlighted by the profiles shown in Figure 19. It can be seen clearly that the non-oscillatory option reduces the gradient as a result of the expected behaviour of $\partial\left|\rho\right|/\partial\mathbf{x}$, whereas the infinite gauge option gives a solution which closely agrees with the exact solution throughout.

3.2.3 Conservation of Scalar Remapping

In addition to the desirable properties required for multidimensional remapping of arbitrary sign scalar fields, a remapping scheme must perform the remapping conservatively. Scalar conservation for the van Leer and infinite gauge MPDATA remapping of the changing sign sine distribution are shown in Figure 20. The

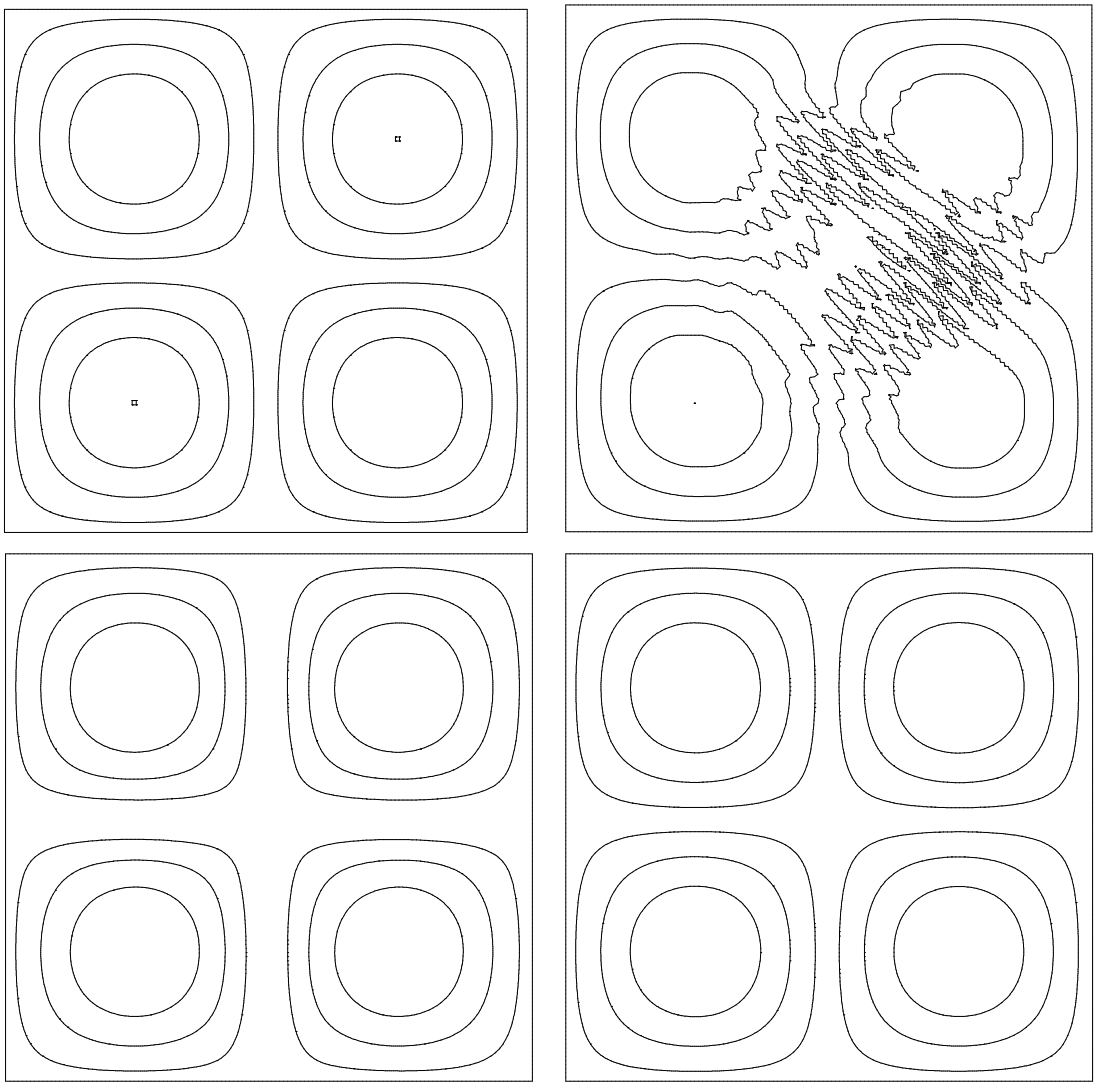

Figure 18: Prescribed mesh motion remapping with the changing sign sine distribution. Top left: exact, top right: van Leer, bottom left: non-oscillatory MPDATA, bottom right: infinite gauge MPDATA.

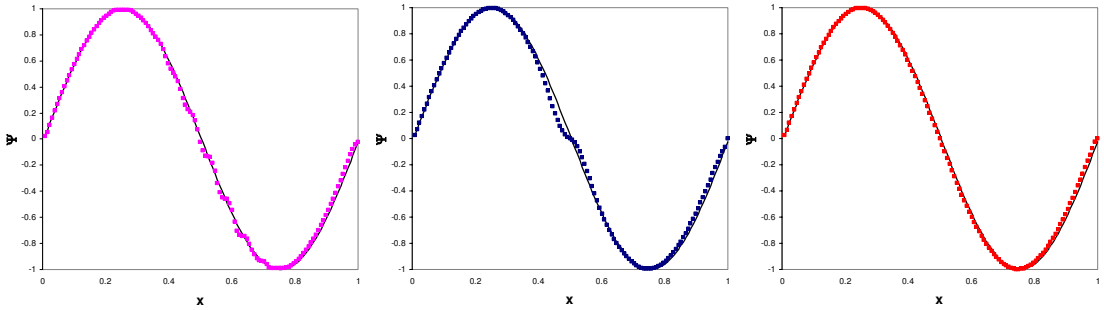

Figure 19: Profiles of the changing sign sine distribution. Left: van Leer, centre: non-oscillatory MPDATA, right: infinite gauge MPDATA. Solid lines show the exact solution.

temporal conservation error is calculated using the error norm

$$E = \frac{\sum_{i,j} \rho_{i,j}^{(+)} - \sum_{i,j} \rho_{i,j}^{(-)}}{\sum_{i,j} \rho_{i,j}^{(-)}}, \tag{89}$$

at each pseudo time step. It can be seen that both the van Leer and infinite gauge MPDATA schemes conserve the scalar. The non-oscillatory MPDATA conservation data is not shown due to similarities to the infinite gauge data.

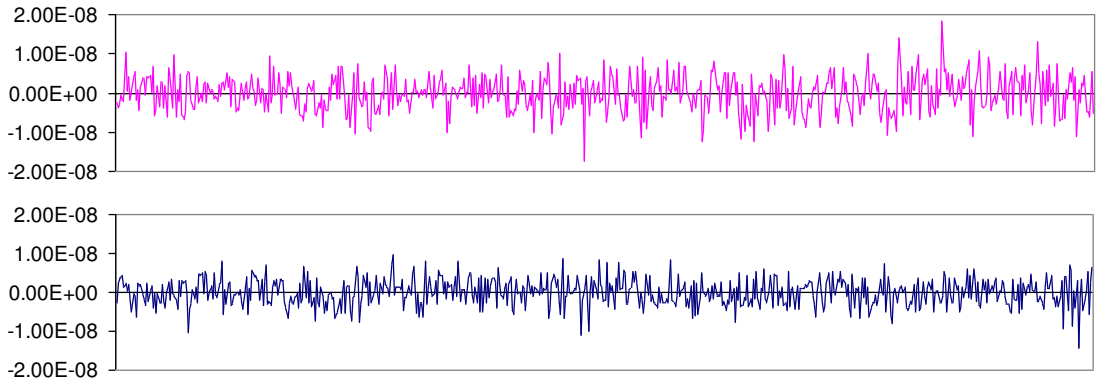

Figure 20: Temporal evolution of the conservation error for the remapping of the changing sign sine distribution. Top: van Leer, bottom: infinite gauge MPDATA.

4 ALE Hydrocodes

Hydrocodes are used to model high deformation simulations dealing with both solid and fluid materials. This is achieved by solving the underlying conservation laws to update values of transported variables associated with a material being modelled. Typically, the transported variables are mass, internal energy and momentum. Hydrocodes may solve the conservation laws in a Lagrangian frame of reference - where the computational mesh moves with the material, or in an Eulerian frame of reference - where the mesh remains fixed. Within the Lagrangian frame of reference, an arbitrary Lagrangian-Eulerian (ALE) scheme may be applied. In this case, the equations are solved as per the Lagrangian scheme, however the computational mesh allows an additional degree of freedom where the solution may be mapped to an arbitrary computational grid using an Eulerian remapping calculation. Furthermore, ALE hydrocodes may operate as purely Lagrangian, purely Eulerian, or essentially Lagrangian whereby the solution is only mapped onto another grid when required in order to keep the simulation running.

A brief description of Eulerian and Lagrangian schemes is given before looking at the benefits of an ALE approach. Following the introductory discussion, details of the Lagrangian calculations and the Eulerian remap are given. Test cases are presented in Section 5 to evaluate the capability of an MPDATA based remap step compared to the benchmark van Leer remapping method.

4.1 Eulerian Schemes

An Eulerian scheme (e.g. [28]) will retain the initially specified grid as the calculation progresses in time. The material that is being modelled will therefore be exchanged between cells of the grid as the simulation is advanced in time. Depending upon the conditions specified at the boundaries of the domain that is being modelled, it is possible that the material being transported may leave the domain that is of interest. In order to avoid such a situation, an Eulerian mesh must be prescribed with some consideration to the material geometry evolving beyond the initial conditions. This leads to a requirement that mesh points are defined at locations where material is not present in the initial state. Furthermore, the mesh must be defined over a large enough domain such that it covers all possible areas of interest as anticipated in future calculations. The requirement to define additional mesh points results in redundant calculations being computed, and requires additional computational resources for the model. However, because the mesh is defined as a constant feature, the geometry of the mesh only needs to be calculated once, and can be stored for convenience. This allows the spatial calculations in the scheme to be reused rather than recalculated at each iteration in time, improving computational efficiency.

In contrast to the Lagrangian approach which follows the behaviour of the material, the Eulerian scheme is largely unaffected by the behaviour of the material

flow - or the magnitude of deformations that arise in the material. This means that in the Eulerian approach the fixed mesh will not cause the calculations to fail as may happen when a moving mesh becomes too deformed. Furthermore, because the mesh does not change as the material evolves in time, the time step used in calculations will not reduce to compensate for changing mesh geometries. This allows a computationally efficient solution to be obtained. However, because of the fixed mesh, the accuracy in tracking the progression of deformations will not be as high as a Lagrangian approach which follows the material movement.

4.2 Lagrangian Schemes

In a Lagrangian scheme (e.g. [29]), the prescribed mesh will remain aligned to the underlying material. In this case, there is no exchange of material between cells. Instead, the nodes of a cell will move independently in space in order to retain the same amount of material that existed in the cell at the start of the simulation. Because the nodes move with the material, the initial mesh may be constructed to precisely match the initial geometry of the material with an optimum amount of nodes. Furthermore, there is no need to place nodes where there is no material in the initial state, as nodes defined in the computational mesh will continue to cover the material at later times. As a result, the Lagrangian scheme avoids the performance of redundant calculations which may occur in the Eulerian approach, however, the geometrical calculations used in the Lagrangian scheme will need to be repeatedly calculated for each node with each mesh movement. Furthermore, for complex physical geometries, a Lagrangian scheme provides a short term solution with good accuracy. This feature arises because the prescribed initial mesh can be mapped directly onto the initial geometry, and so interpolation errors are avoided. In addition, high resolution can be achieved by judicial placement of

an increased number of nodes in areas of interest, and fewer nodes used to model regular geometry. With each mesh movement occurring in the Lagrangian scheme, the mesh will then remain closely matched to the geometry of the material.

Problems arise for Lagrangian schemes during complex flows and high deformation models. The nodes of a cell move independently to follow the material. When the flow is simple, all nodes of a cell are likely to behave concurrently and accurately resolve material movement. This will avoid the situation where the mesh imprints upon the solution in the way an unsuitable Eulerian mesh may [2]. When the flow is turbulent each node may move with different velocities when compared to the other nodes of the same element. As a result, the element may become tangled. This will result in the introduction of inappropriate physical behaviour such as artificial stiffness, and difficulty in resolving geometrical calculations. Problems with geometrical calculations may at best introduce numerical error, or at worst result in the Lagrangian calculations failing. Furthermore, where a variable time step is utilised as a function of the cell size and material properties, as the mesh becomes highly deformed, the time step will reduce. This allows complex flows to be treated using more care, however will also mean that the execution time for the simulation will increase significantly. Such a feature is not experienced by Eulerian schemes, in this case the Eulerian scheme may be a preferable choice as the time step is more likely to remain at a level which will attain the final solution in a reasonably efficient time.

4.3 Arbitrary Lagrangian-Eulerian (ALE) schemes

An alternative execution of Eulerian schemes is to first perform the standard Lagrangian calculations, allowing the mesh to follow the transported material. An Eulerian solution is then recovered by interpolating the solution from the

deformed Lagrangian grid back to the original mesh. This process is known as remapping and is achieved by Eulerian advection - the process of advecting transported variables (mass, energy, momentum) between the cells of the Lagrangian grid, to the cells of the Eulerian grid. The Lagrangian-Eulerian scheme therefore results in an Eulerian solution as the mesh upon which the solution is viewed after each time step does not change. This approach is used by majority of the published Eulerian hydrocodes [30, 31, 32, 33, 34, 35, 36, 37]. The Lagrangian-Eulerian scheme may be further advanced by allowing the mesh to be defined as an independent variable [40]. In such a case, the scheme may be termed as an arbitrary Lagrangian-Eulerian (ALE) scheme (e.g. [7, 38, 39, 40, 41, 42, 43, 44]) because the choice of the mesh to which the Lagrangian solution is mapped onto by the Eulerian step does not depend upon the results of either step.

Within ALE schemes, the Eulerian remap step is not required after each iteration of the Lagrangian calculation. If the Lagrangian calculations are dealing with well behaved solutions, the ALE scheme may run as a pure Lagrangian scheme for a number of iterations. The remap calculation will then only be required after a number of iterations to remap the solution onto a relaxed grid. A relaxed grid will essentially be of the same form as the Lagrangian grid, however the general structure of the relaxed grid will be specified with improved geometric properties in order to maximise the computational time step and avoid impinging upon the calculations used to obtain the solution [2].

The process of defining the nodal position of the relaxed grid, i.e. locations that will theoretically improve the Lagrangian calculations, is termed as rezoning. Remapping after a series of Lagrangian iterations is termed “periodic rezoning”. Alternatively, an Eulerian remap may be performed in each iteration. In this situation, remapping is termed “continual rezoning”. The relaxed grid is generated by reducing the individual spatial movement of each node as determined by the

Lagrangian calculations, i.e. only moving the nodes by a smaller amount than a pure Lagrangian scheme would. In addition, the relaxed mesh may be defined through the use of weights to ensure nodes remain aligned to material interfaces or to the flow of material through the mesh. This results in the nodes moving in the direction determined by the Lagrangian step, however the deformations in the grid will not grow as significantly in each step, and the cumulative effect of deformations is reduced resulting in a well behaved solution that has the benefits of a Lagrangian scheme.

While either choice for mesh rezoning is acceptable for most hydrocode problems, the computational cost of performing small continual rezones is often less than that of performing periodic rezones where the geometry of the mesh may need to be significantly redefined [2]. Furthermore, either rezone strategy has the benefit of not requiring user intervention to rezone the locations of the nodes, which may be required for deformation issues with the Lagrangian scheme. Indeed, for high deformation problems in a pure Lagrangian scheme, a manual rezone may be required after each iteration. This issue is redundant within an ALE scheme, with the continuous rezone strategy better suited to ensure that the solution does not approach a highly deformed state.

Depending upon the behaviour of the ALE model it is possible to divide the domain of interest to create regions within the mesh. Each region may then be considered individually, and treated as either pure Lagrangian, pure Eulerian or as ALE. A continual rezone strategy may again be a better choice in such cases. Although the subdivision will be initially prescribed by the user, as the solution advances in time, the region may not remain suitable for exclusive treatment as prescribed. The continual rezone strategy will ensure that a Lagrangian mesh remains well behaved throughout the domain. This allows the computational benefits of the Lagrangian scheme to be fully exploited without the need for any

user intervention.

4.4 Hydrocode Implementation

The Atomic Weapons Establishment (AWE) have provided an extensive sample package for single material ALE simulations. It is in this package that the MPDATA based remap schemes will be implemented.

The supplied AWE package [45] is a full ALE hydrocode capable of running simulations over multiple regions. The package may be split into three sections; initialisation, a Lagrangian step and a remapping step. Initialisation consists of mesh generation for each region whereby the nodes and elements are created. Connectivity is then established relating node to node, element to element and node to element. Boundary nodes and elements are identified for special treatment within the package. Regions allow distinct mesh designs to be utilised in different areas of the domain being modelled. Regions also allow more than one material to be modelled in a single code, however the considerations of a fully multi-material code are not included (as described in Section 6). The adjacent regions are then joined together by establishing node-to-node and element-to-element connectivity across the shared boundary of each region. Finally the initial conditions of the problem are mapped onto the domain. At this stage the components of the velocity field and physical variables (density, ρ, and pressure, p) to be transported are quantified. The solution is advanced in time by iterating over the Lagrangian and remapping steps. Test cases in Section 5 utilise only one region.

4.4.1 The Lagrangian Step

Once the mesh and initial condition are provided, the Lagrangian step is executed. Following the description given in [2], this step solves the evolution laws for mass, energy and momentum:

$$\frac{D\rho}{Dt} = -\rho\nabla\cdot\mathbf{v}, \tag{90}$$

$$\rho\frac{De}{Dt} = -p\nabla\cdot\mathbf{v}, \tag{91}$$

$$\rho\frac{D\mathbf{v}}{Dt} = -\nabla p, \tag{92}$$

where ρ denotes density, $\mathbf{v}$, velocity, p pressure and e internal energy, and the Lagrangian derivative is given by

$$\frac{D}{Dt} = \frac{\partial}{\partial t} + \mathbf{v}\cdot\nabla. \tag{93}$$

These laws form a system of coupled partial differential equations. The system is closed with the addition of an equation of state, giving the pressure:

$$p = p(\rho, e). \tag{94}$$

However, this form of the evolution laws is not suitable for discontinuous shock problems. Therefore an artificial viscosity term is introduced [46]. Artificial viscosity allows shock discontinuities to be replaced by a sharp but smooth distribution, spread over numerous cells. The artificial viscosity, $\mathbf{q} \sim \nabla\mathbf{v}$, is included in the pressure term so that (92) becomes

$$\rho\frac{D\mathbf{v}}{Dt} = -\nabla(p+\mathbf{q}), \tag{95}$$

$$\rho\frac{De}{Dt} = -(p+\mathbf{q})\nabla\cdot\mathbf{v}. \tag{96}$$

Equations (92), (94), (95), and (96) are then solved by sequentially calculating the required terms. The first step is the specification of isoparametric finite elements used for spatial discretisations. Once the element dimensions are determined, a stable time step is calculated. The ALE scheme allows a variable time step to be employed so that in cases where the computational mesh is well formed, the time step may be maximised in order to reduce the time required to perform a simulation. However, when the mesh becomes heavily distorted, the time step may also be reduced to ensure stability. The time step is controlled by the Courant-Friedrichs-Lewy (CFL) condition, however to allow a direct comparison between remapping methods, a fixed stable time step is predetermined in test cases in Section 5.

The next step calculates the artificial viscosity and divergence terms, followed by determining updates of the scalar variables. This is achieved by first determining the values at a half time step. The nodes of the computational mesh are therefore moved with their associated acceleration to the half time step position. Updates of the finite elements, and scalar variables are then calculated. The Lagrangian step is completed by moving the nodal positions for a further half-time step, now using the temporal mean velocity for the node from time steps t^n and $t^{n+1/2}$. The final step provides the finite elements and scalar variables at the time t^{n+1}.

4.4.2 The Rezone Step

Once the Lagrangian step has been performed, the scalar variables are remapped to either a relaxed grid, or back to the initial grid. When remapping back to the initial grid, the velocities utilised in the Lagrangian step are used, taken with the opposite sign. When remapping to a relaxed grid, the Winslow equipotential

rezone strategy is employed [47]. The Winslow rezone strategy inverts the Laplace equation to form a logically regular mesh built with lines of equal potential [1]. Following [1], the logical mesh directions are ϕ and θ, with the inverse of the Laplace equation given as

$$\begin{aligned} \alpha x_{\phi,\phi} - 2\beta x_{\phi,\theta} + \gamma x_{\theta,\theta} = 0, \\ \alpha y_{\phi,\phi} - 2\beta y_{\phi,\theta} + \gamma y_{\theta,\theta} = 0, \end{aligned} \tag{97}$$

with

$$\begin{aligned} \alpha = x_\theta^2 + y_\theta^2, \\ \beta = x_\phi x_\theta + y_\phi y_\theta, x_\phi^2 + y_\phi^2, \end{aligned} \tag{98}$$

and

$$\begin{aligned} x_\phi = \frac{1}{2}\left(x_{i,j+1} - x_{i,j-1}\right), \qquad x_\theta = \frac{1}{2}\left(x_{i+1,j} - x_{i-1,j}\right), \\ x_{\phi,\phi} = x_{i,j+1} - 2x_{i,j} + x_{i,j-1}, \qquad x_{\theta,\theta} = x_{i+1,j} - 2x_{i,j} + x_{i-1,j}, \\ x_{\phi,\theta} = \frac{1}{4}\left(x_{i+1,j+1} - x_{i-1,j+1} + x_{i-1,j-1} - x_{i+1,j-1}\right). \end{aligned} \tag{99}$$

Corresponding stencils for y are obtained by substituting y for x in the above definitions.

The rezoned coordinates of cell centres are then obtained by substituting (98-99) into (97) so that

$$\begin{aligned} x_{i,j} = \frac{1}{2(\alpha+\gamma)}\left(\alpha\left(x_{i,j+1} + x_{i,j-1}\right) + \gamma\left(x_{i+1,j} + x_{i-1,j}\right)\right. \\ \left. -\frac{\beta}{2}\left(x_{i+1,j+1} - x_{i-1,j+1} + x_{i-1,j-1} - x_{i+1,j-1}\right)\right), \end{aligned} \tag{100}$$

$$\begin{aligned} y_{i,j} = \frac{1}{2(\alpha+\gamma)}\left(\alpha\left(y_{i,j+1} + y_{i,j-1}\right) + \gamma\left(y_{i+1,j} + y_{i-1,j}\right)\right. \\ \left. -\frac{\beta}{2}\left(y_{i+1,j+1} - y_{i-1,j+1} + y_{i-1,j-1} - y_{i+1,j-1}\right)\right). \end{aligned} \tag{101}$$

With either rezone strategy, the remap step doesn't evolve the solution in time, as discussed in Section 2. The remap step in the ALE scheme simply alters the computational mesh and values of each scalar variable in the elements of the relaxed mesh.

4.4.3 The Remap Step

In order to perform the update of the mesh and the scalar variables, the subject of the Lagrangian derivative (93) in Equations (92) will replace ψ in the van Leer scheme, and Ψ in the MPDATA based remap schemes detailed in Section 2. Pressure is updated after the scalar variables are remapped using the equation of state as per the Lagrangian step.

The ALE hydrocode utilises a staggered mesh structure, with the scalar variables ρ, e, p being stored at the element centres, and the velocity components stored at the nodes. The remapping methods detailed in Section 2 are specified for variables stored at element centres so that ρ and ρe may replace Ψ directly. However momentum, $\rho\mathbf{v}$, requires construction of a dual grid to correctly align the nodal variables. Therefore, before the components of momentum may be remapped, a nodal density and volume must be determined conservatively. Within this hydrocode, regular Cartesian grids are used, so each element is rectangular. Therefore a nodal volume is obtained by the summation of quarter volumes surrounding the node, for example:

$$V_{i+1/2,j+1/2} = \frac{1}{4}\left(V_{i,j} + V_{i+1,j} + V_{i,j+1} + V_{i+1,j+1}\right) \tag{102}$$

The nodal density is obtained in the same manner due to the assumption of a mean distribution in each element:

$$\rho_{i+1/2,j+1/2} = \frac{1}{4}\left(\rho_{i,j} + \rho_{i+1,j} + \rho_{i,j+1} + \rho_{i+1,j+1}\right). \tag{103}$$

This approach is conservative, and is compatible with the deBar consistency condition [37].

5 ALE Test Cases

5.1 Sod's Shock Tube

Sod's shock tube problem [48] allows an investigation into the ability of a scheme to model a shock, contact discontinuity and a rarefaction wave. The test case is defined by two regions of gas with different densities and pressures over the domain $[0,1]\times[0,0.1]$ separated by a thin film at $x = 0.5$. The regions are initially at rest and the film is instantaneously removed, bearing no further influence to the simulation. The regions utilise ideal gas equations of state with the ratio of specific heats in both regions taken as $\gamma = 1.4$. The density and pressure are defined as:

$$\rho = \begin{cases} 1 & \text{if } x \leq 0.5, \\ 0.125 & \text{if } x > 0.5 \end{cases} \qquad p = \begin{cases} 1 & \text{if } x \leq 0.5, \\ 0.1 & \text{if } x > 0.5 \end{cases}$$

Once the simulation is started, a shock is formed at the contact discontinuity which travels away from the region with higher pressure - termed the driver - to the region with lower pressure - termed the test gas. At the same time, a rarefaction wave propagates away from the test gas. The pressure and velocity are continuous across the contact discontinuity, however the density and specific internal energy are not. All variables are discontinuous over the shock wave.

The simulation is run with a constant time step of $\delta t = 0.001$ on a grid with uniform resolution $\delta x = \delta y = 0.01$ halted at $t = 0.15$ so that the shock and rarefaction waves do not reach the boundaries of the computational domain. Figure 21 shows the density, energy, pressure and velocity profiles for the van Leer (red), non-oscillatory MPDATA (green) and non-oscillatory infinite gauge MPDATA (black) ALE schemes.

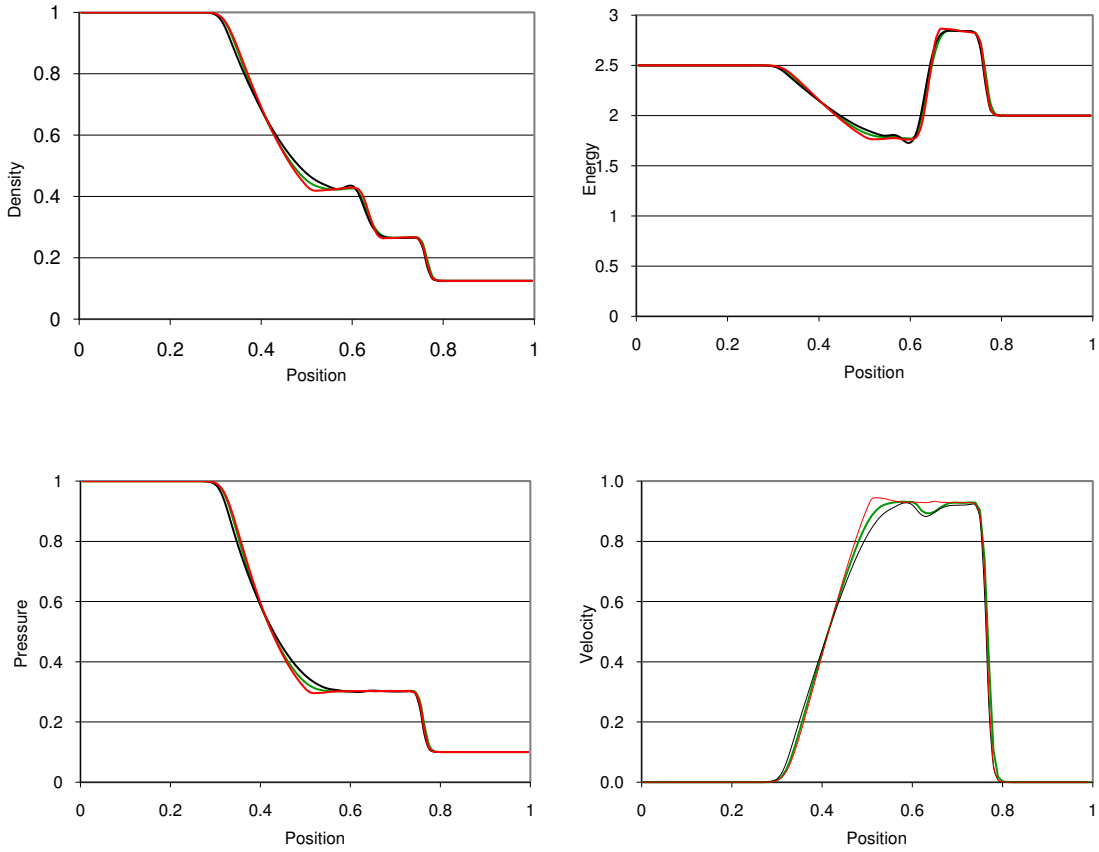

Figure 21: Comparison of density (top left), internal energy (top right), pressure (bottom left) and velocity (bottom right) profiles along $y = 0.05$. Red: isotropic van Leer, green: non-oscillatory MPDATA, black: non-oscillatory infinite gauge MPDATA

It can be seen from Fig. 21 that all three schemes model the shock front ($x \approx 0.75$) and contact discontinuity ($x \approx 0.6$) with comparable performance. The rarefaction ($x \approx 0.5$) however is modelled significantly better by the van Leer based scheme, with the MPDATA based schemes exhibiting greater diffusion at each end of the rarefaction wave. Similar performance can also be seen with the pressure and energy distributions. A significant error appears in the MPDATA based schemes, where an erroneous dip is introduced into the velocity profile corresponding the contact discontinuity. It may be expected that the one-dimensional van Leer based scheme performs better within a one-dimensional test case. Strang split van Leer results are not shown due to the one-dimensional nature of the test case.

5.2 The Explosion Problem

The Explosion problem [49] is essentially an axisymmetric two-dimensional extension to Sod's shock tube benchmark. The domain is filled with an ideal gas with specific heat ratio coefficient $\gamma = 1.4$. A circular region of radius $r = 0.4$ is centred at the origin of a $[-1, 1] \times [-1, 1]$ domain with higher density, ρ, and pressure, p, compared to the rest of the domain.

$$\rho = \begin{cases} 1 & \text{if } |r| \leq 0.4, \\ 0.125 & \text{if } |r| > 0.4. \end{cases} \qquad p = \begin{cases} 1 & \text{if } |r| \leq 0.4, \\ 0.1 & \text{if } |r| > 0.4. \end{cases}$$

The gas is initially at rest so that a contact discontinuity, shock and rarefaction wave are formed radially as the simulation progresses. The computations are conducted on $\delta x = \delta y = 0.01$ and $\delta x = \delta y = 0.005$ Cartesian grids. The geometry of the Cartesian grid is mismatched with the radial initial conditions which may evoke perturbations at the interface between regions of high and low

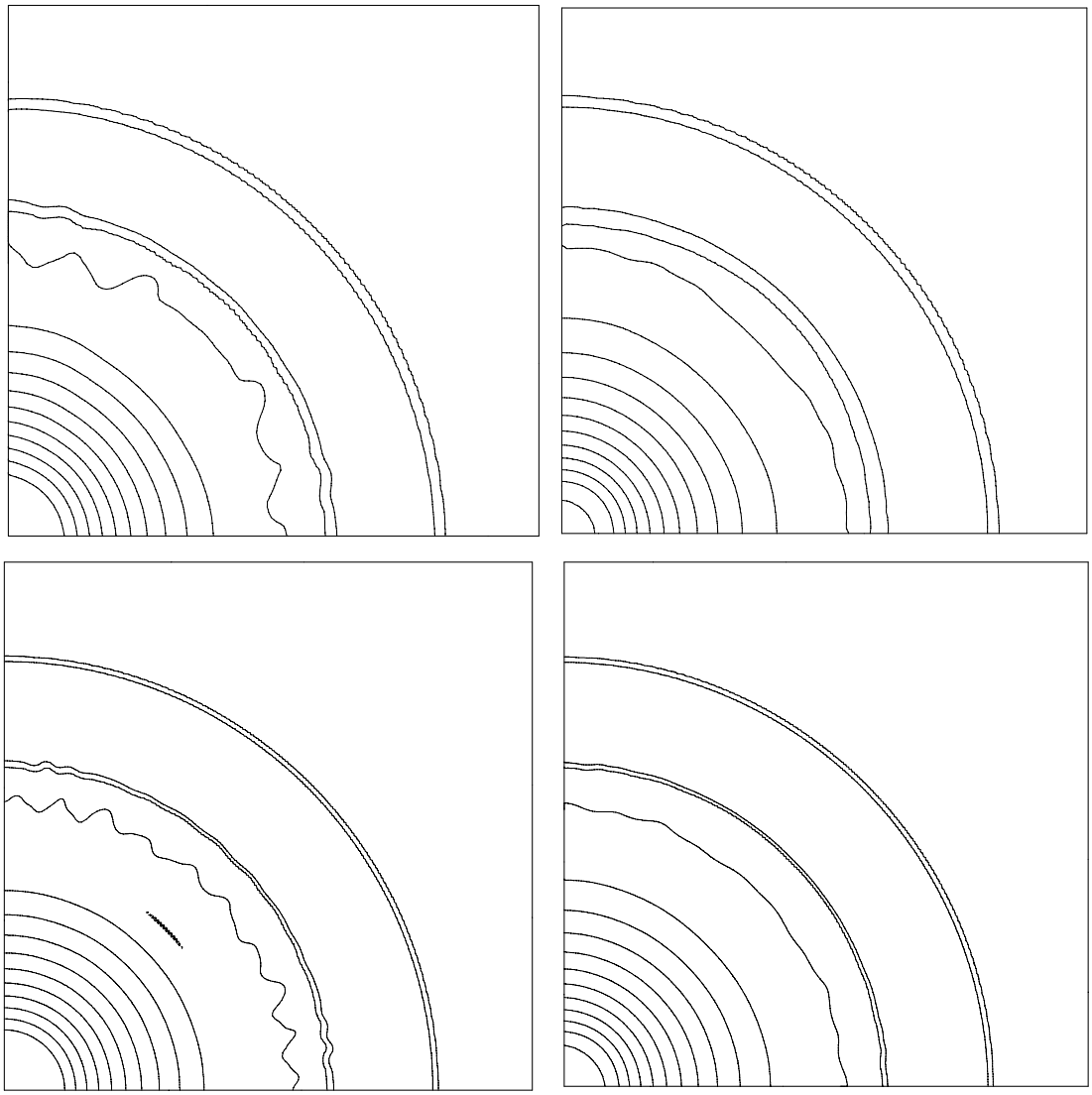

Figure 22: Density contours at $t = 0.25$ for the Explosion problem with Eulerian and Winslow mesh rezoning; the isotropic van Leer scheme is shown in the top, and the MPDATA scheme in the bottom row. The left column shows the Eulerian solutions, the right column shows the Winslow solutions. The contour interval is 0.066, minimum contour level, $\rho = 0.125$.

densities and pressures. The Explosion problem is usually simulated up to $t = 3.2$ [50]. At this time, the shock wave reflects back into the contact discontinuity. In order to compare the explosion problem with the one-dimensional Sod's problem it is treated as a two-dimensional Sod's problem in this work. Therefore, the simulation is run until $t = 0.25$

A comparison of the resulting density contours at $t = 0.25$ is shown in Fig. 22 employing both Eulerian and Winslow mesh rezoning. A considerable error is visible in the rarefaction wave of the van Leer solution using isotropic remapping. Indeed, this arises due to the castellated interface between material properties where the lack of true multidimensionality highlights corner coupling errors. Significantly, the errors seeded at the initial material interface are impinging upon the radial position of the contact discontinuity. This has the result of damaging the required symmetry in the simulation. The infinite gauge MPDATA based scheme however, does not exhibit the same behaviour at the material interface, with the castellation effect being suppressed due to the utilisation of information from all directions in the remapping. Preservation of symmetry is therefore stronger in the MPDATA scheme. Such a mismatch of geometries may be reduced by smoothing the interface using area weighting in the cells which are intersected by the circle. The initial castellated interface is retained however to provide a challenge when studying properties of remapping. As seen in Fig. 22, the solutions obtained on both mesh sizes retain their characteristic features with the results from the refined mesh being less diffusive. The computations were repeated with the van Leer implementation using Strang splitting with Eulerian rezoning. The corresponding contour plots are not shown because their departure from the MPDATA results (Eulerian rezoning) is insignificant.

The density, energy, pressure and velocity profiles representing a cut through the $\delta x = \delta y = 0.005$ mesh at 45° are shown in Fig. 23. Due to the circular

symmetry of the problem, only the positive quadrant is modelled. Both methods perform comparably in each of the profiles, and conform to results in the literature such as the high order one-dimensional solution of Toro (Fig. 17.4 in [49]). It can be seen that the isotropic remapping van Leer scheme introduces an overshoot in the velocity profile in the region surrounding $r = 0.4$ which is linked to a dip at the base of the rarefaction wave of the density profile. This feature is not physical, and is not present in the MPDATA solution. Small inaccuracies at the contact discontinuity and shock are present within the profiles for both solutions. The van Leer solution using Strang splitting appears to be more diffusive in the regions of discontinuities, however, a rigorous comparison of this result is impeded by differences in the implementation of the routines used in ALE (detailed in Section 6.2).

The Explosion problem also allows an examination of the conservation properties of MPDATA. Figure 24 shows conservation of the transported variables mass, internal energy and the components of momentum. The temporal evolution of the conservation is measured according to the norm (89) where each ρ is replaced by mass M, Me, Mu or Mv and u and v are components of velocity in the x and y directions respectively.

5.3 Noh's Problem

The Noh problem [51] consists of a cold, ideal gas with density $\rho = 1.0$, internal energy $e = 0.0$, ratio of specific heat $\gamma = \frac{5}{3}$ and uniform velocity $\|\mathbf{v}\| = -1.0$ forcing the gas into a rigid wall. An infinite strength shock is generated at the wall boundary and travels in the opposite direction to the gas flow. The simulation of the planar case (rigid wall along $x = 0.0$) is carried out on a $[0, 1] \times [0, 0.2]$ domain, discretised with a series of uniform resolution grids. The simulation of

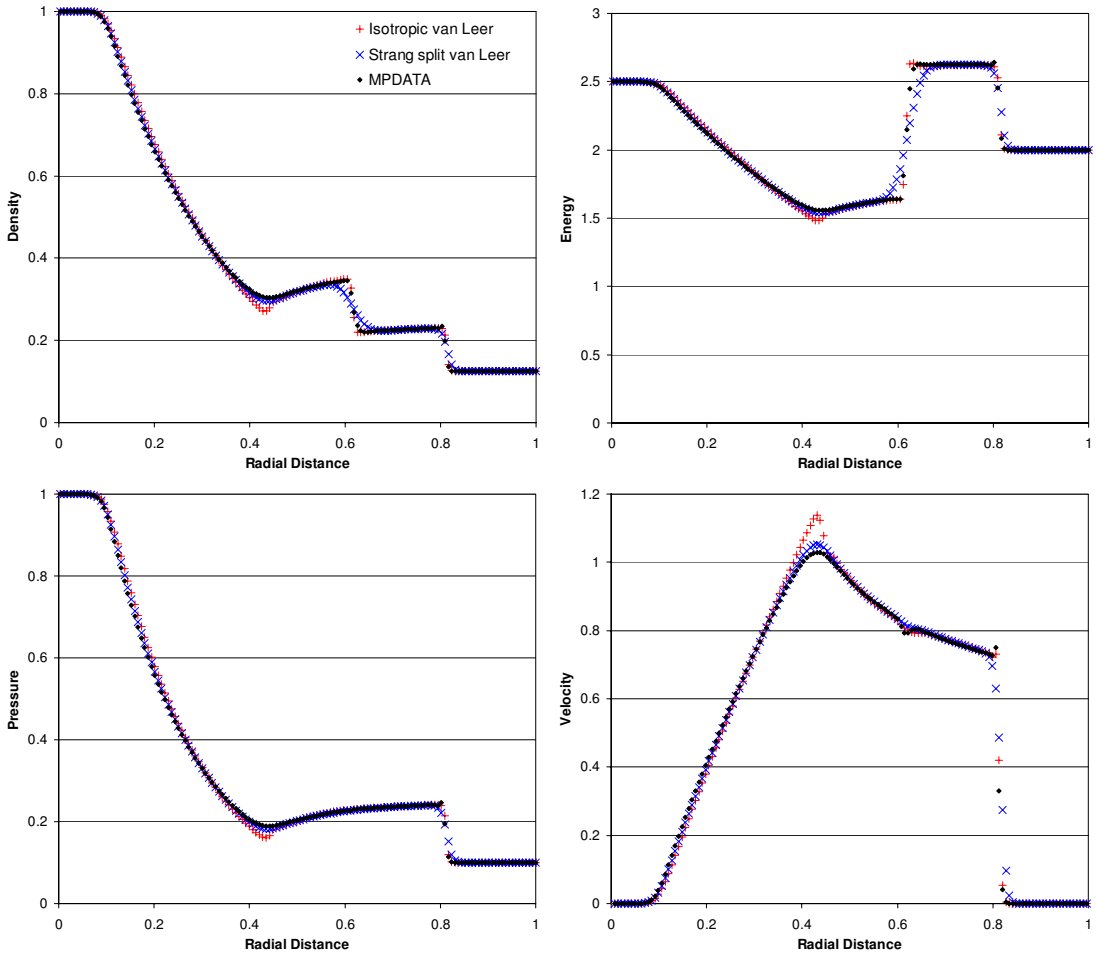

Figure 23: Density, energy, pressure and velocity profiles of the Explosion problem with Eulerian rezoning.

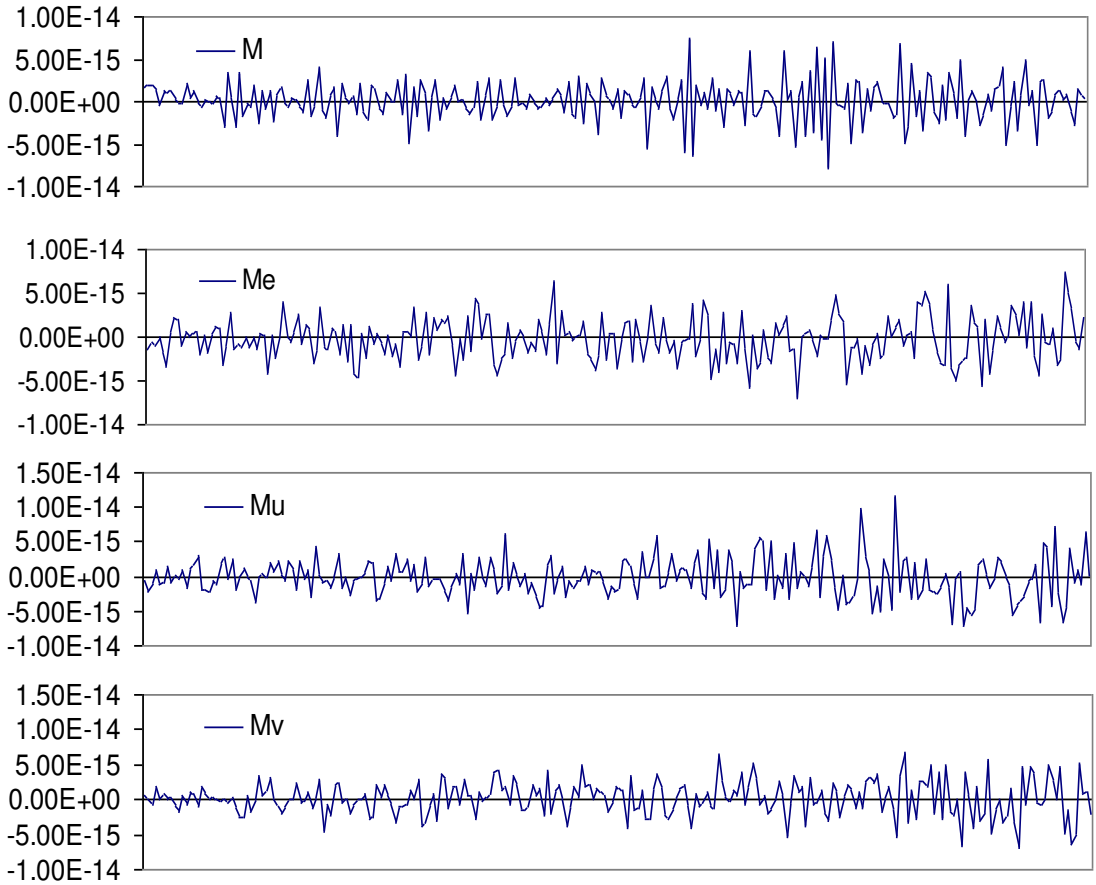

Figure 24: Density, energy, pressure and velocity profiles of the Explosion problem with Eulerian rezoning.

the cylindrical case (wall at $(x, y) = (0, 0)$) is performed on a Cartesian mesh on a $[0, 1] \times [0, 1]$ domain, with $\delta x = \delta y = 0.005$ and $\Delta t = 0.0005$. Exact values are used on inflow boundaries, with symmetry utilised on boundaries $x = 0$ and $y = 0$ in the cylindrical case. Both planar and cylindrical cases use a constant time step, terminating at time $t = 0.6$.

Due to the nature of the Noh problem, wall heating errors are introduced at the wall boundary. The strong shock stagnates at the impermeable wall. At this stage, elements near the boundary experience large compression so that the added artificial viscosity is not dissipated sufficiently, manifesting itself as unphysical heating. This generates a build up of energy at the wall boundary which in turn forces a drop in the density as the equation of state establishes the correct pressure level. The wall heating error in the Noh problem arises in the Lagrangian solution of unsteady wave propagation and is related to factors such as the application of artificial viscosity, phase errors, wave speed or changes in mesh resolution travelling with the shock. A thorough analysis of the sources of wall heating is provided in Reference [52].

5.3.1 Planar Case

The planar Noh problem, executed on a $\delta x = \delta y = 0.01$ grid with $\delta t = 0.001$ is shown in Figure 25. It can be seen in this diagram that the MPDATA result is correctly aligned to the exact solution in terms of the shock position and the level of post-shock density accumulation, whereas the van Leer scheme incorrectly aligns both features in a manner consistent with results shown in [52] for Eulerian calculations using internal energy. Of particular interest, it can be seen that the van Leer scheme has masked the wall heating error. This feature has arisen due to the van Leer scheme being forced to give a first-order accurate solution at

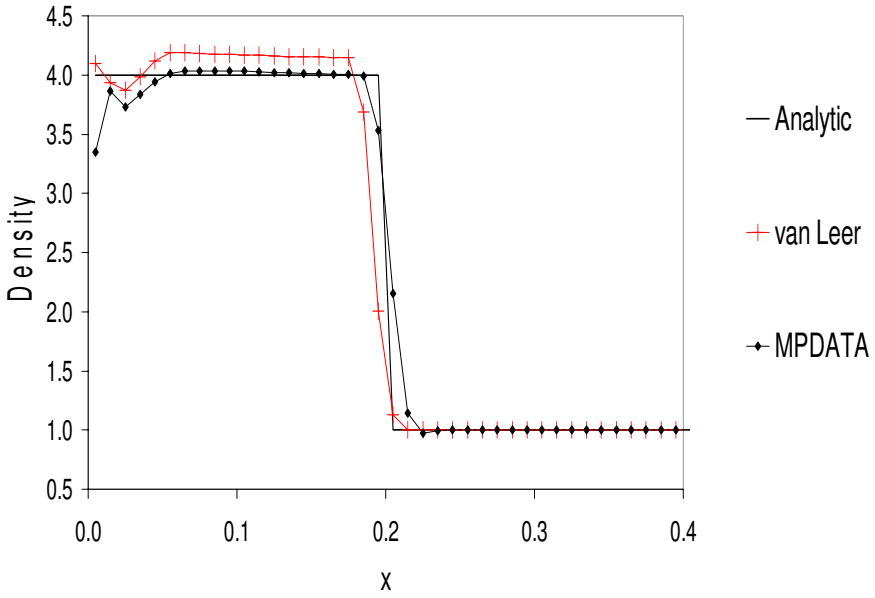

Figure 25: Density profiles of the planar case of the Noh problem.

the wall elements because the larger stencil required to construct the monotonic piecewise linear distribution of the transported variables is not available at the boundary. The infinite gauge MPDATA based scheme has accurately remapped the Lagrangian wall heating features, which are unphysical, near the boundary at $x = 0.0$. Although the behaviour of the van Leer scheme with regard to the wall heating errors is undesired in a remapping scheme in general, the additional diffusion introduced by a reduction in the order of remapping accuracy is beneficial in this particular test case.

The MPDATA method allows oscillations, in this case due to the wall heating errors, to be reduced readily by applying a controlled reduction of the antidiffusive fluxes in the corrective pass (39), c.f. [53]. Uncommonly, reducing the compensating terms in MPDATA does not deteriorate the stability of the algorithm. The procedure is equivalent to adding a small amount of $\mathcal{O}(\delta x)$ artificial

viscosity, while avoiding costs incurred by computing viscous terms.

This feature is especially useful in this test case as it can be seen that the first-order solution at the boundary in the van Leer remapping gives a value which is greater than the exact solution. Obtaining accuracy which is between first- and second-order at the boundary can give a value of density which lies closer to the exact solution. Implementation of such a treatment may be made by adding a coefficient κ to each of the fluxes in the second pass of the basic or infinite gauge MPDATA schemes. The second pass may then be written as

$$\begin{aligned}\Psi^{(+)}_{i,j} = \Psi^{(1)}_{i,j} - \; & [\kappa_1 F(\Psi^{(1)}_{i,j}, \Psi^{(1)}_{i+1,j}, C^{(1)}_{i+1/2,j}) - \\ & \kappa_1 F(\Psi^{(1)}_{i-1,j}, \Psi^{(1)}_{i,j}, C^{(1)}_{i-1/2,j})] \\ - \; & [\kappa_2 F(\Psi^{(1)}_{i,j}, \Psi^{(1)}_{i,j+1}, C^{(1)}_{i,j+1/2}) - \\ & \kappa_2 F(\Psi^{(1)}_{i,j-1}, \Psi^{(1)}_{i,j}, C^{(1)}_{i,j-1/2})]. \end{aligned} \tag{104}$$

An anisotropic reduction in compensation, applied in the x-direction with $\kappa_1 = 0.25$, $\kappa_2 = 1$ in (104) of the wall boundary elements is shown in Figure 26. This treatment within the region near the wall boundary, results in the first-order-accurate solution not being fully corrected to second-order, whereas second-order accuracy ($\kappa_1 = \kappa_2 = 1$) is retained elsewhere. Figure 26 shows that the effective wall heating error is reduced. It should be noted that κ was chosen empirically, however, the value used may be automated based on an inspection of the gradient of the density or energy field in the region near the boundary.

The illustrated reduced compensation procedure shows that the addition of diffusion in the elements exhibiting wall heating errors is beneficial, but such an approach cannot entirely remove the wall heating errors because oscillations are present also in the first-order solution. In this case, the second-order filtering option detailed in Section 2.6 is particularly suitable.

The second-order filtering option adds a small amount of diffusion to the first-

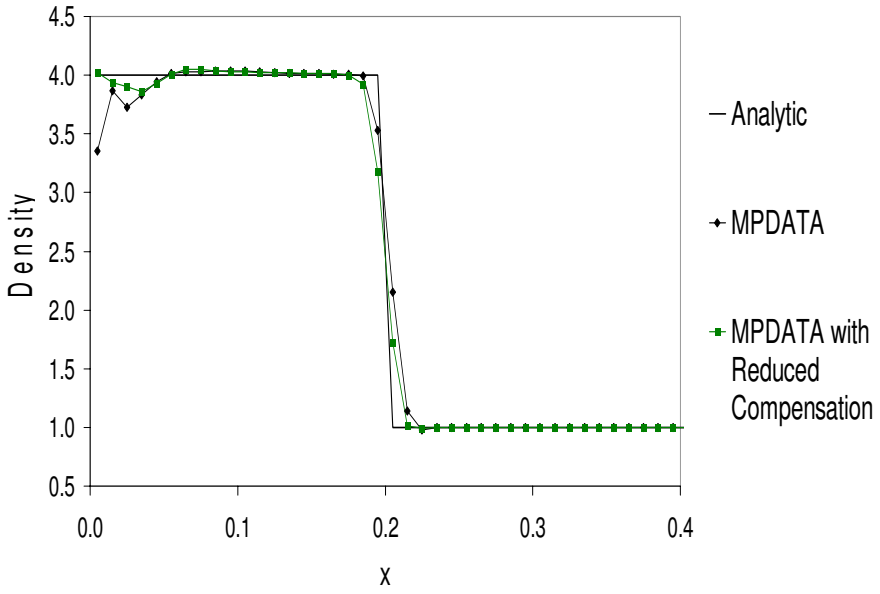

Figure 26: Infinite gauge MPDATA density profiles with locally reduced compensation of Noh's problem.

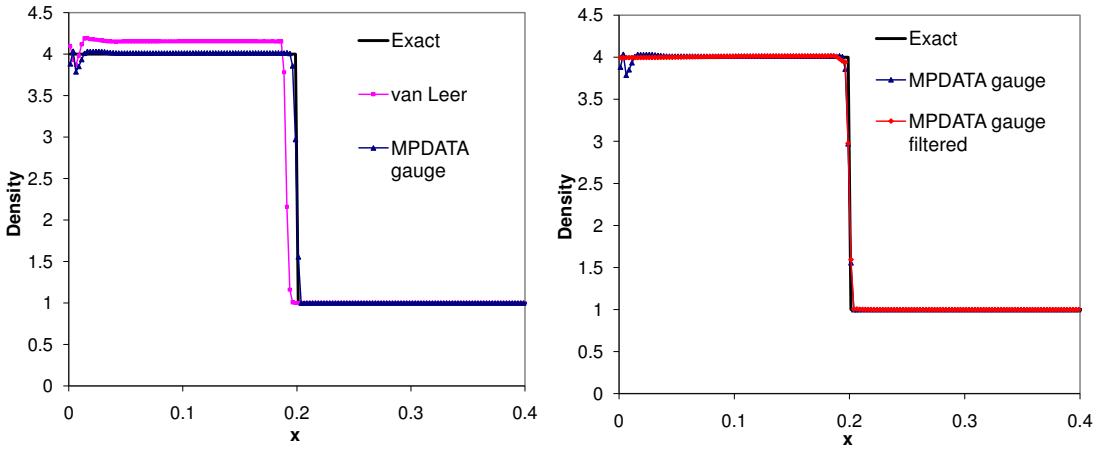

Figure 27: Density profiles of the planar case of the Noh problem. Left: infinite gauge MPDATA and van Leer solutions, right: infinite gauge MPDATA with and without second-order filtering. $\delta x = \delta y = 0.0025$, $\delta t = 0.00025$.

order pass. This has the effect of removing oscillations occurring in the first-order pass. Once the added diffusion is compensated by the second-order pass, the oscillations will no longer be present. Furthermore, unlike the reduced compensation treatment, the second-order filtering option requires no user intervention, and so calibrating an effective value of κ is not required. The effect of the second-order filtering option is shown in Figure 27. In this case, the simulation is executed with $\delta x = \delta y = 0.0025$ and $\delta t = 0.00025$, highlighting the consistency of the MPDATA solution across mesh resolutions.

As for the solutions on the coarser grid, the MPDATA result is correctly aligned to the exact solution in terms of the shock position ($x = 0.19958$ using linear interpolation for $\rho = 2.5$) and the level of post-shock density accumulation, whereas the van Leer scheme again incorrectly aligns both features (shock at $x = 0.19073$). The filtering option of MPDATA is applied anisotropically in the direction of flow at all element edges except those where a shock has been

	Grid	Density	I.E.	T.E.	Pressure	Velocity
van Leer	100×20	0.105941	0.148222	0.148211	0.186724	0.079659
	200×20	0.126266	0.188564	0.188557	0.203178	0.094454
	400×20	0.139633	0.208208	0.208204	0.212429	0.102806
Infinite	100×20	0.058166	0.064287	0.064252	0.074276	0.035359
gauge	200×20	0.040818	0.043834	0.043832	0.058089	0.025558
MPDATA	400×20	0.030565	0.035261	0.035260	0.053451	0.021844
MPDATA	100×20	0.056939	0.061482	0.061475	0.075888	0.035611
gauge	200×20	0.039963	0.042083	0.042081	0.057768	0.025556
filtered	400×20	0.029813	0.033872	0.033871	0.053052	0.021781

Table 3: L_2 error data for planar Noh problem with increasing mesh resolution in the direction of flow. I.E. denotes internal energy; T.E., total energy.

detected. Therefore, the filtering does not smear the shock any further than has been done so with the application of artificial viscosity in the Lagrangian phase, and gives a more accurate shock position ($x = 0.19961$). The shock is detected automatically by examination of pressure gradients. The exclusion of the shock from the filtering is not essential, but provides a modest enhancement.

The departures from the exact solutions are reflected by Table 3 which gives L_2 error data for the $\delta x = \delta y = 0.01$, $\delta x = \delta y = 0.005$ and $\delta x = \delta y = 0.0025$ meshes. These norm values show consistently higher errors in all variables for the van Leer scheme compared to the MPDATA based scheme. Due to the presence of a shock, the treatment of inflow boundaries and other factors, Table 3 is not suitable for an assessment of asymptotic mesh convergence.

The above simulations are calculated with conservation of internal energy rather than total energy. Such solutions depend upon the level of entropy pro-

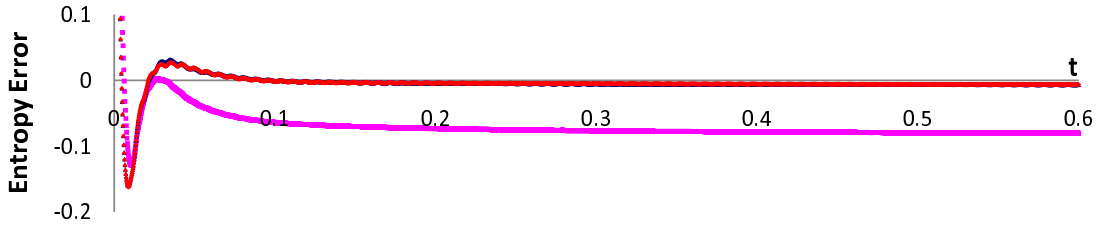

Figure 28: Entropy errors for the planar Noh Problem ($\delta x = \delta y = 0.0025, \Delta t = 0.00025$). van Leer (pink square), infinite gauge MPDATA (blue triangle), MPDATA gauge filtered (red diamond).

duction. Fig. 28 shows the ratio of entropy error for each method, defined as

$$E = \frac{\sum_i \delta x_i p_i \rho_i^{(1-\gamma)} - 2^{2/3} t/9}{2^{2/3} t/9}. \tag{105}$$

See [52] for further discussion on entropy errors. All methods have large start up errors (maximum entropy error for the van Leer scheme is 1.652, MPDATA based schemes, 1.655), however the van Leer scheme stabilises to a level significantly below the correct production level so that the incorrect features are evident. The MPDATA solutions attain more accurate levels of entropy production, however it can be seen that the start up errors and the conservation of internal energy rather than total energy, cf. [25, 52], are still affecting the solutions. This is seen by the MPDATA-based remapping entropy errors asymptotically approaching a negative value (-0.006 at $t = 0.6$).

5.3.2 Cylindrical Case

The cylindrical case of the Noh problem allows the wall heating error to be examined under amplified conditions due to the nature of the velocity field. The multidimensional nature of the problem also allows an examination of the capabilities to preserve symmetry. The symmetry preservation requirement in this

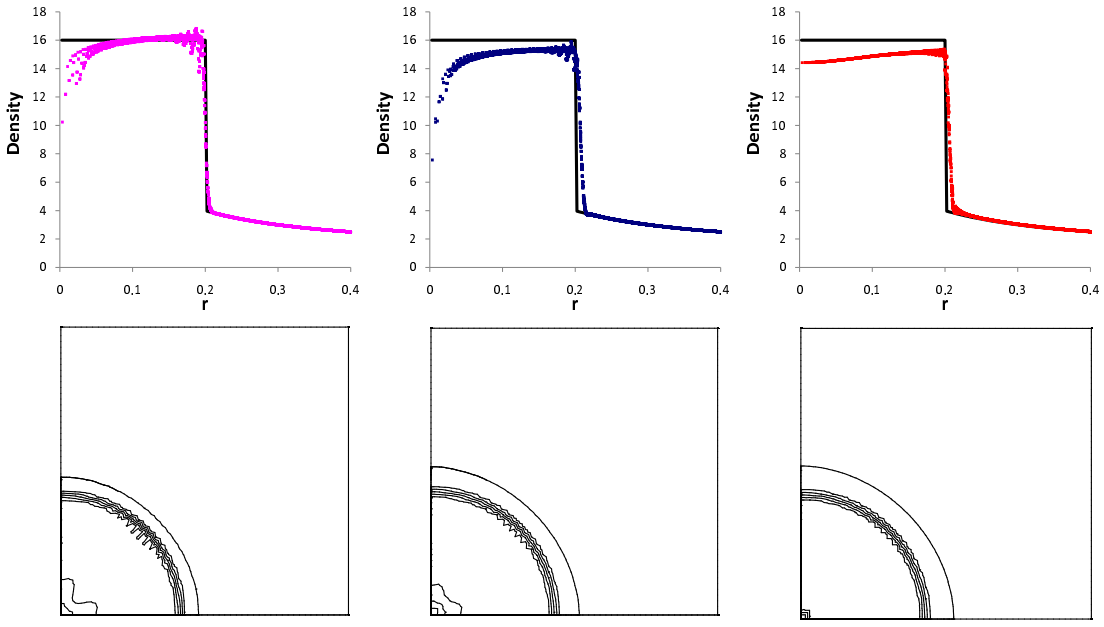

Figure 29: Upper row: Density plotted against radius for the cylindrical case of the Noh problem (Cartesian mesh). Left: van Leer, centre: MPDATA gauge, right: MPDATA gauge with second order filtering. Lower row: Corresponding density contours (quarter of the domain shown), minimum value $\rho = 2.0$, contour interval, 1.0.

test case is particularly challenging due to the use of a Cartesian grid to model a radially symmetric problem.

Figure 29 shows the density distributions obtained on a $\delta x = \delta y = 0.005$ Cartesian mesh at $t = 0.6$ ($\Delta t = 0.0005$). The van Leer based scheme is extended to two-dimensions by isotropic remapping. In this case corner coupling errors dominate the van Leer solution with a loss of symmetry, and significant errors along the cut $x = y$ (linearly interpolated shock position along for $\rho = 10$ at $r = 0.19932$). As in the planar case, the method features a first-order solution

at the "wall" (origin), however in this case the first-order solution does not mask the wall heating errors. The MPDATA gauge solution features an incorrect shock position ($r = 0.20646$) because of the wall heating errors. This in turn leads to an under evaluation of post-shock density accumulation. The multidimensional nature of MPDATA provides greater preservation of symmetry, with a significant reduction in errors along the cut $x = y$, as highlighted in the contour plots of Fig. 29.

The symmetry preservation errors shown in the van Leer solution arise for any isotropic extension of any one-dimensional scheme to multidimensions. A scheme in which a one-dimensional version of MPDATA was employed isotropically in place of the van Leer scheme produced results (not shown) very close to those in the left panel of Fig. 29.

Applying the second-order filtering with MPDATA gauge significantly reduces the wall heating errors, and improves the preservation of symmetry. However, the effect of filtering is ultimately limited by the underlying Lagrange and MPDATA gauge solution, so that the shock position ($r = 0.20544$) and post-shock density accumulation are improved, but not fully regulated to the correct levels. The key result from the second-order filtering solution in the axisymmetric case is the marked improvement in symmetry.

Christensen [54] monotonic artificial viscosity is used in Lagrangian phase of the simulations with coefficients $c_q = 0.75$ and $c_l = 0.5$. The c_l coefficient determines the diffusivity of the artificial viscosity. A reduction of this coefficient results in oscillations along the post shock density accumulation, and is therefore not appropriate for unfiltered methods. The filtering option however, introduces a small amount of diffusion in the remapping phase, and in this case c_l may be reduced, with c_q remaining unchanged (not shown). In the planar case, this permits very low wall heating errors on coarse meshes. In the axisymmetric case,

greater symmetry preservation is provided due to a reduction of oscillations in the post-shock region near the jump in density, particularly along the cut $x = y$.

6 Multimaterial ALE Hydrocodes

Hydrocodes may model more than one material in a given simulation. Depending upon whether a hydrocode permits more than one material to be present in a single element determines if it is termed a Simple ALE (SALE) scheme or a multi-material ALE (MMALE) scheme. A SALE hydrocode will only allow one material to be present in each cell of the computational mesh. In simulations featuring turbulence, the material interface can quickly become distorted and this restriction will lead to a reduction in accuracy. Permitting cells to contain more than one material, as is the case in an MMALE hydrocode, will allow the flow of material to be modelled more accurately, although this approach will introduce a computational overhead and presents several issues which will be addressed in the discussion.

6.1 Overview

Lagrangian schemes dealing with multiple materials allow material interfaces to be computed effectively. The computational mesh may be defined accurately for the geometry of each material, with nodes aligning correctly with material interfaces. Alternatively, a number of meshes may be defined for each material, with a natural mesh boundary inherently defined. Boundary conditions where multiple meshes meet will then control the interaction of energy and momentum across the boundary, yet ensuring that mass is not transferred between materials, and that those materials behave appropriately. When dealing with a solid-gas interface, it is physically inaccurate for the materials to mix, whereas an atmospheric model featuring multiple gases would be free to mix. Pressure relaxation treatments [2] and additional physics of the boundary can be included in this situation. For example, the opening and closure of voids, and friction arising due to the materi-

als sliding against each other will be handled by two or more boundaries moving independently at an interface. Again, if the Lagrangian mesh material interfaces become highly distorted the solution may fail, in which case the Eulerian scheme may be more suitable as it is not affected by such deformations.

Multimaterial Eulerian schemes [28] will not keep track of the precise locations of interfaces as a result of the fixed nature of the mesh. Early Eulerian schemes have previously been considered as the last resort when dealing with multiple materials experiencing high deformations because the choice of Eulerian grid will impinge upon the solution at some future time iteration. However, with the development of interface tracking algorithms, the performance of Eulerian schemes is improved. Interface tracking algorithms such as [55, 56] allow the interface location to be followed, however because interfaces are modelled upon the fixed mesh, nodes are not free to move and follow material interfaces. Consequentially, the Eulerian scheme in this case will not provide as good a solution as the Lagrangian schemes may provide by exactly aligning to the material interface.

Many ALE schemes dealing with multiple materials are classed as Simple ALE (SALE). In SALE schemes, individual elements only contain one material. This allows the material interfaces to remain purely Lagrangian, avoiding problems associated with advection occurring between different materials. Interfaces may then be tracked by defining separate meshes for each material and connecting the boundary nodes where required.

A less restrictive approach to multiple materials in ALE schemes allows individual elements to contain more than one material (i.e. MMALE). This is important for cases where the material experiences deformation, or with turbulent flow acting upon the materials. The purpose of ALE schemes is to avoid situations where the mesh becomes tangled by relaxing the mesh after the Lagrangian step. However, if material interfaces are forced to remain fully Lagrangian, the

mesh will not be able to be fully relaxed, resulting in the Lagrangian boundaries becoming tangled and may result in the failure of the simulation, or a significant reduction in computational time step. In the MMALE case, as for Eulerian schemes, interface reconstruction algorithms are required.

This issue has recently been addressed by Barlow [2] whereby an adaptive treatment of interfaces is utilised. While the flow is stable and the mesh is not distorted, interfaces are treated as in the SALE methods. However, once retaining the complete Lagrangian interface is not practical due to mesh distortions, a Volume of Fluid (VOF) [57] method is employed utilising Simple Line Interface Calculation (SLIC) [58, 59]. VOF methods reconstruct material boundaries by estimating how much of each material is present in an element and representing it as a fraction of the volume of an element. This allows any number of materials to be present in an element and requires the summation of material volume fractions λ_m to equal unity. The SLIC algorithm is then used to reconstruct the boundary by constructing straight lines within the element which are parallel or normal to the advection direction. The directions of the lines are determined by the presence of each material on each side of the element. For example, given an orthogonal mesh, this approach results in the element containing a series of rectangles, with the size of the rectangles determined by the fractions calculated by the VOF method.

Greater accuracy methods such as Youngs' algorithm [60, 61], and Moment of Fluid (MOF) [62, 63] are also available. Youngs' algorithm reconstructs the material interface, for example between two materials (material 1 and material 2), by utilising volume fractions of the two materials, and an inward pointing normal from material 1. In two dimensions, this information is used to approximate the material interface by a straight line. A multidimensional trace around the neighbouring elements is used to determine the material normal. The normal is

then moved through the element to match the volume fractions. See [60, 61, 64] for a more detailed explanation.

MOF [65, 66] allows material interfaces to be reconstructed by minimising the error between actual material volume centroids and the calculated material centroids. In this way, only information available within the element in which the reconstruction is taking place is utilised. Although the reduction of computational stencil is desirable, particularly for parallelisation of codes, the method requires additional data (material centroids) to be advected or remapped between elements, and two minimisation procedures to be performed so that additional computational cost is incurred.

The interface reconstruction algorithms are extended to more than two materials per element by nested dissection. Nested dissection is achieved by repeated calculations of the interface reconstruction. For example, in a three material case, with materials m_1, m_2 and m_3 the algorithm is first employed between Ω_1 and Ω_2 where $\Omega_1 = m_1 \cup m_2$, $\Omega_2 = m_3$. The volume fraction for Ω_1 must be calculated first as $\lambda_{\Omega_1} = \lambda_1 + \lambda_2$. Once the first application of the algorithm is performed, the algorithm is then repeated using $\Omega_3 = m_1$ and $\Omega_4 = m_2$ with $\lambda_{\Omega_3} = \lambda_1/\lambda_{\Omega_1}$ and $\lambda_{\Omega_4} = \lambda_2/\lambda_{\Omega_1}$. Care must be taken when defining the material ordering for the nested dissection approach because combined final material interfaces will depend upon the chosen order. See [65] for cases where the behaviour of the interface when different material ordering are used for the same volume fraction data.

6.2 MMALE Algorithm

The MMALE algorithm used in this work [64] operates as an Eulerian code, whereby after each Lagrangian step, the solution is remapped back to the initial

grid. A staggered mesh arrangement is employed. Within the Lagrangian step, new values of density, internal energy and pressure for each material are calculated as per the method detailed in Section 4.4.1, with equal volumetric strain pressure relaxation used so that volume fractions, λ_m, for all materials present in an mixed element expand or contract equally in proportion to the element volume [2]. As a result of the equal volumetric strain method, volume fractions are not updated in the Lagrangian step. Components of velocity are updated according to the values of total mass within an element. The general method of updating velocity components is therefore not altered from the SALE approach discussed in Section 4, however the calculation of total density, $\rho = \sum \lambda_m \rho_m$, is required prior to the generation of nodal values for the dual grid.

An Eulerian rezone step is implied due to the Eulerian nature of the code. The remapping step is then required to interpolate density and internal energy, as well as volume fractions for all materials. Velocity components are again remapped with total mass, and so remapping may be performed as detailed in Section 4.4.3. Multidimensionality of remapping is achieved via Strang splitting. Overlap volumes are therefore defined by the average normal displacement method.

6.3 Remapping in MMALE Schemes

Material properties must be remapped according to the associated material volumes so that, for example, within Upwind remapping, equation (5) becomes

$$\lambda_m^{(+)} V^{(+)} = \lambda_m^{(-)} V^{(-)} - \Sigma_{k=1}^{n} \left(\Delta V_k\right)_m . \tag{106}$$

The quantities $\left(\Delta V_k\right)_m$ for the k^{th} face of the element are the volume of material m present in the overlap volume ΔV_k. This volume is determined by the calculation of a flux volume fraction, λ_m^f. To obtain the flux volume fraction, the material

interface is reconstructed in the donor cell (the cell which the ΔV_k overlaps). In this work, Youngs' algorithm [60] is employed in all examples. Once the interface is constructed, the intersection of the overlap volume and the donor cell is calculated. The intersection of the volumes and position of the interface within the donor cell then determines the volume of each material inside the overlap volume to define the flux volume fraction. Finally, the flux for each material is specified as $(\Delta V_k)_m = \lambda_m^f \Delta V_k$.

The intersection of the overlap volumes and donor cells with defined material interfaces allows $(\Delta V_k)_m$ to be zero when ΔV_k may be non-zero. As such, fluxing will not occur when material m is present in the donor cell, but not connected to the acceptor cell. Such a situation may arise when thin films of a material become sandwiched between another material in high deformation flows.

Volume fractions for the Eulerian grid are recovered by dividing (106) by $V^{(+)}$ and applying a scaling check to ensure $\sum \lambda_m^{(+)} = 1.0$. In a similar fashion, the scalar update equation (6) will then become

$$\lambda_m^{(+)}\Psi_m^{(+)} = \lambda_m^{(-)}\Psi_m^{(-)} - \Sigma_{k=1}^{n} (\Delta V_k)_m \left(\Psi_k^{(-)}\right)_m , \tag{107}$$

The scalar $\psi_m^{(+)}$ is recovered by dividing (107) by $V^{(+)}\lambda_m^{(+)}$.

Remapping in regions where only one material is present, i.e. all elements required by the remapping calculation have a volume fraction equal to one (pure cells) for the material being remapped, may be remapped as per the single material case. When $\lambda_m = 1$ for the material present in the pure cell, the volume and scalar updates (106)-(107) reduce back to (5) and (6), respectively. Van Leer and MPDATA multimaterial remapping extensions follow logically from the extension of upwind to multiple materials, however considerations must be given to the behaviour of the higher order schemes at the material interfaces, indicated by volume fractions or flux volume fractions not being equal to unity (mixed

cells). The scalar update for material properties remapped in mass co-ordinates rather than volume co-ordinates follows by replacing each cell volume in (107) by material masses $M_m = \rho_m V$.

Van Leer remapping with multiple materials extends from the considerations regarding material volumes and material properties rather than element volumes and element material properties set out for equations (106)-(107). The multi-material MPDATA based scheme is obtained in a similar manner, with (34)-(39) updated by altering the definition of the transported variable to $\Psi = \psi_m \lambda_m V$, and the Courant number akin quantity C being scaled such that

$$C = \frac{\lambda_m^f \Delta V}{\lambda_m V^{(-)}}. \tag{108}$$

6.3.1 Material Interfaces with van Leer based Remapping

The van Leer MUSCL approach used in this work as a benchmark identifies the donor cell, and then utilises a stencil of three adjacent elements centred on the donor cell to construct a second-order monotonic estimate of the distribution of the scalar or vector variable being remapped, as detailed in Section 2.2. In single material simulations, the large stencil poses a problem at the domain boundaries where the required elements are not available. This issue is also present at material interfaces. In this case, although the required elements exist, the volume fractions or flux volume fractions of the particular material is zero, so that an incorrect approximation of the scalar distribution would be obtained if the algorithm were performed without consideration of this issue.

To deal with the volume fraction data equalling zero at the material interface, a number of approaches are available. The presence of a mixed cell, or a pure cell which does not contain the material being remapped, will clearly impact calculations of derivatives and limiters in higher order methods in general, therefore

the most common approach is to use first-order remapping at material interfaces. This approach is used by the benchmark van Leer based multimaterial remapping. However, as in the single material case, the first-order Upwind scheme introduces additional diffusion. Rider [67] examines a number of van Leer type methods with varying levels of dissipation, concluding that an adaptive mixed cell approach is more beneficial such that upon the detection of mixed cells, the scheme evaluates one sided derivatives with monotonicity ensured by more dissipative limiting criteria.

The adaptive mixed cell approach has been shown to be a more accurate and computationally efficient approach than simply resorting to the first-order Upwind scheme [67]. However, such an approach is still inherently one-dimensional, and does not have optimal accuracy due to the monotonicity constraints being specified with more dissipative limits than the single material case. The multimaterial van Leer scheme used in this work automatically reduces to first-order accuracy in all test cases shown.

6.3.2 Material Interfaces with MPDATA based Remapping

The nature of MPDATA, i.e. iterations of the first-order Upwind scheme, allows for the potential retention of second-order accuracy at material interfaces. In one-dimensional flows, or multidimensional planar flows where the material interface is aligned with the computational grid, the cross terms utilised in the evaluation of derivatives in (35), for example, disappear so that MPDATA uses the same stencil as the first-order Upwind scheme. In this case, when the calculated flux volume fraction is non-zero, the upwind iteration of MPDATA is permissible, and consequently, the antidiffusive upwind pass of MPDATA is also permissible. Unlike van Leer therefore, all steps of the MPDATA may still be

calculated at material boundaries, so that there is no restriction on potential accuracy at material interfaces. Furthermore, in this case, values required for the monotonicity preservation also exist, and so the standard limiting procedure may be used. This behaviour is illustrated by the untreated MPDATA solutions in Section 5.3. The wall boundary of the domain in the Noh problem replicates a material boundary because in both cases, fluxes across the boundary are forced to zero. It is seen in Section 5.3 that the untreated MPDATA solutions correctly remap the Lagrangian errors, whereas the van Leer scheme which is forced to first-order accuracy is unable to do so.

In multidimensional flows, the orientation of the material interface may pose an issue to the retention of second order accuracy within the MPDATA scheme on the material boundaries. The cross terms of the pseudo Courant number calculation, i.e. (35), will be active in multidimensional simulations, and include an estimation of the gradient in the direction parallel to the face, (23). The material interface may intersect any of the elements in this calculation, so that some, all, or none of the elements contain the material being updated. In this case, a number of approaches are possible.

For simplicity, when a complex material interface is detected by the absence of a number of the elements required for a sound approximation of the derivative, a reduction to first-order accuracy may be a sensible and robust approach. At such a complex material interface, the required information for a monotonic second-order scheme may not be sufficiently available or reliable, with spurious oscillations being incorrectly introduced into the solution. This approach will lead to the same issues raised by the van Leer approach, in that an over diffused solution will be obtained at the material interfaces, however the approach may be deemed the most reliable in terms of completing a simulation.

An alternative approach, only available to the MPDATA method, would be

to disable cross terms whenever a material interface is detected. The pseudo Courant number calculation, (35), for example, would then become

$$C^{(1)}_{i+1/2,j} \equiv \left|C_{i+1/2,j}\right| \left(1 - \left|C_{i+1/2,j}\right|\right) A^{(1)}. \tag{109}$$

This would allow a second-order solution to be interpolated, within the same stencil size as the Upwind scheme because $A^{(1)}$ includes a forward difference approximation of the derivatives on the elements used in the Upwind calculation. However, a key strength of the MPDATA remapping - multidimensionality - would be lost. Furthermore, this approach would disregard information which is potentially available when the material interface is not complex.

Rather than reducing to a one-dimensional form of MPDATA, or to an Upwind calculation as standard, and in the spirit of Rider [67], an adaptive mixed cell approach utilising alternate approximations of the derivatives is proposed. Currently, the $B^{(1)}$ term, (23) takes the mean of central difference approximations in the appropriate direction using values of the scalar or vector field surrounding the edge upon which the flux is calculated. In the case that one or more of the required values does not exist due to the orientation of the material interface, the central difference approximation may be substituted by a forward difference approximation. Although this will reduce the order of accuracy of the derivative used in the cross term, the cross terms will still be active, and so multidimensionality at the material interface will be retained.

The stencil used in the calculation of $A^{(1)}$ and $B^{(1)}$ ((22) and (23)) for the right face of a quadrilateral element is shown in Figure 30 including significant cases affecting the approximation of derivatives in a two material case. The presence of the material being remapped is tested by a non-zero flux volume fraction for that material. Therefore the cases detailed are valid for an arbitrary number of materials.

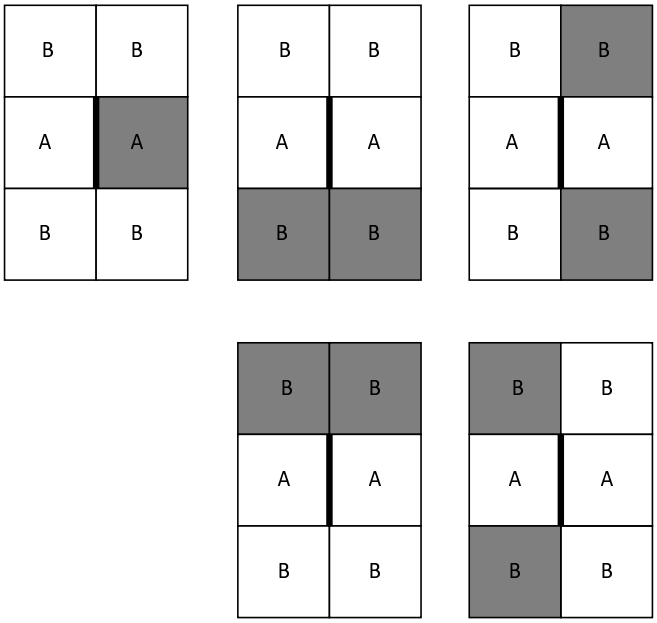

Figure 30: Multimaterial stencils for derivative calculations. Elements required for $A^{(1)}$ and $B^{(1)}$ are denoted A and B respectively. Significant material interface cases between a dark and light material are shown; left column, case (a); upper centre, case (b), lower centre case (c); upper right, case (d), lower right, case (e).

In case (a), shown in Figure 30, the light material is not present in element $i+1, j$. When this element is the donor cell for the transport of the light material, the light material is required to be present for any flux to be non-zero. This is because $C_{i+1/2,j} = \lambda_m^f \Delta V_{i+1/2,j}/\lambda_m V^{(-)}$, and with $\lambda_m^f = 0$ for the light material, $C_{i+1/2,j} = 0$. Therefore there is no initial first-order pass to compensate an error for. Furthermore, when the light material in element $i+1, j$ occupies a very small portion of the element such that $\lambda_m^f \approx 0$, the calculation of

$$C^{(1)}_{i+1/2,j} \equiv \left|C_{i+1/2,j}\right| (1 - \left|C_{i+1/2,j}\right|) A^{(1)} - 2f\bar{C}_{i,j+1/2} C_{i+1/2,j} B^{(1)}$$

goes to zero because $C_{i+1/2,j} \approx 0$ is present in both terms on the right hand side.

Cases (b) and (c) represent the situation where the calculation of (23) is not possible in the current form. An alternative approximation may still be made however, by updating the approximation of $\partial\psi/\partial y$ in (23). This may be achieved by replacing the central difference approximation by a one sided difference approximation utilising the elements where the light material is present. In this way, (23) becomes

$$B^{(1)} \equiv \frac{\left|\Psi^{(1)}_{i+1,j+1}\right| + \left|\Psi^{(1)}_{i,j+1}\right| - \left|\Psi^{(1)}_{i+1,j}\right| - \left|\Psi^{(1)}_{i,j}\right|}{\left|\Psi^{(1)}_{i+1,j+1}\right| + \left|\Psi^{(1)}_{i,j+1}\right| + \left|\Psi^{(1)}_{i+1,j}\right| + \left|\Psi^{(1)}_{i,j}\right|}, \tag{110}$$

for case (b), and

$$B^{(1)} \equiv \frac{\left|\Psi^{(1)}_{i+1,j}\right| + \left|\Psi^{(1)}_{i,j}\right| - \left|\Psi^{(1)}_{i+1,j-1}\right| - \left|\Psi^{(1)}_{i,j-1}\right|}{\left|\Psi^{(1)}_{i+1,j}\right| + \left|\Psi^{(1)}_{i,j}\right| + \left|\Psi^{(1)}_{i+1,j-1}\right| + \left|\Psi^{(1)}_{i,j-1}\right|}, \tag{111}$$

for case (c).

Cases (d) and (e) also represent situations where (23) cannot be calculated as normal. In these cases, $\partial\psi/\partial y$ in (23) may be approximated by taking only the

central difference approximation of elements $i, j+1$ and $i, j-1$ in case (d), or elements $i+1, j=1$ and $i+1, j-1$ in case (e). Equation (23) then becomes

$$B^{(1)} \equiv \frac{\left|\Psi^{(1)}_{i,j+1}\right| - \left|\Psi^{(1)}_{i,j-1}\right|}{\left|\Psi^{(1)}_{i,j+1}\right| + \left|\Psi^{(1)}_{i,j-1}\right|}, \tag{112}$$

for case (d), and

$$B^{(1)} \equiv \frac{\left|\Psi^{(1)}_{i+1,j+1}\right| - \left|\Psi^{(1)}_{i+1,j-1}\right|}{\left|\Psi^{(1)}_{i+1,j+1}\right| + \left|\Psi^{(1)}_{i+1,j-1}\right|}, \tag{113}$$

for case (e).

Degenerative cases of these situations may also be identified and (23) updated accordingly, for example, in case (b) the light material may not be present only in element $i, j+1$ or $i, j-1$. In this case, the derivative calculation would become a combination of cases (b) and (d) or (e).

Correct limiting must also be considered to avoid over diffusion being introduced by monotonicity constraints in a similar way reported by [67]. Limiting for MPDATA at the material interfaces is updated so that values of Ψ are only included in the Ψ^{MAX} and Ψ^{MIN} quantities in (62) and (63) when the appropriate flux volume fractions λ^f_m are non-zero. Fluxes in the denominators of (62) and (63) are also only included when the flux volume fractions are non-zero due to the inclusion of λ^f_m in each F_k. Finally, the ξ values in (69):

$$\begin{aligned}
\widehat{C}^{(1)}_{i+1/2,j} = \quad & \left[C^{(1)}_{i+1/2}\right]^+ \left(min(1, \xi^{IN}_{i+1,j}, \xi^{OUT}_{i,j}) \left[sgn(\Psi^{(1)}_{i,j})\right]^+ \right. \\
+ \quad & \left. min(1, \xi^{OUT}_{i+1,j}, \xi^{IN}_{i,j}) \left[sgn(-\Psi^{(1)}_{i,j})\right]^+ \right) \\
+ \quad & \left[C^{(1)}_{i+1/2,j}\right]^- \left(min(1, \xi^{OUT}_{i+1,j}, \xi^{IN}_{i,j}) \left[sgn(\Psi^{(1)}_{i+1,j})\right]^+ \right. \\
+ \quad & \left. min(1, \xi^{IN}_{i+1,j}, \xi^{OUT}_{i,j}) \left[sgn(-\psi^{(1)}_{i+1,j})\right]^+ \right)
\end{aligned}$$

are also only considered if λ_m^f for the appropriate edge is non-zero. When $\lambda_m^f = 0$, the minimum value is taken from the available quantities rather than introducing a zero value for the unavailable quantity. Introducing a zero value would force the limiting to restore the first order solution. In this way, the inherent beneficial properties of MPDATA would be cancelled out by the monotonicity condition.

7 Multimaterial Test Cases

7.1 Artificial Interface Test Cases

In order to identify the behaviour of the various remapping approaches at material interfaces available to the MPDATA based remapping, test cases featuring artificial material interfaces are examined. The artificial interfaces are created by defining two materials which have the same physical properties, however the associated material volume fractions are distinct so that fluxing across the artificial material interface is not permitted. In this situation, the solution would be expected to be similar to the single material solution if the remapping of each material at interfaces has the same order of accuracy as the purely single material remapping.

7.1.1 Sod's Shock Tube with Artificial Interface

The Sods Shock Tube is defined as per Section 5.1, however an artificial interface is inserted into the driver section such that

$$\lambda_1 = \begin{cases} 1 & \text{if } x \leq 0.4, \\ 0 & \text{if } x > 0.4 \end{cases} \qquad \lambda_2 \begin{cases} 0 & \text{if } x \leq 0.4. \\ 1 & \text{if } x > 0.4 \end{cases}$$

The test is carried out with a variable time step on a Cartesian computational grid with $\Delta x = \Delta y = 0.01$.

At the end of the simulation the artificial interface will introduce a perturbation in the rarefaction wave at $x = 0.41$. Figure 31 shows the single material and artificial interface solutions for the van Leer, non-oscillatory MPDATA and infinite gauge MPDATA based schemes. All schemes show the desired minor deviation from the single material case, however, a magnified view of the interface highlights the differences between the schemes in Figure 32.

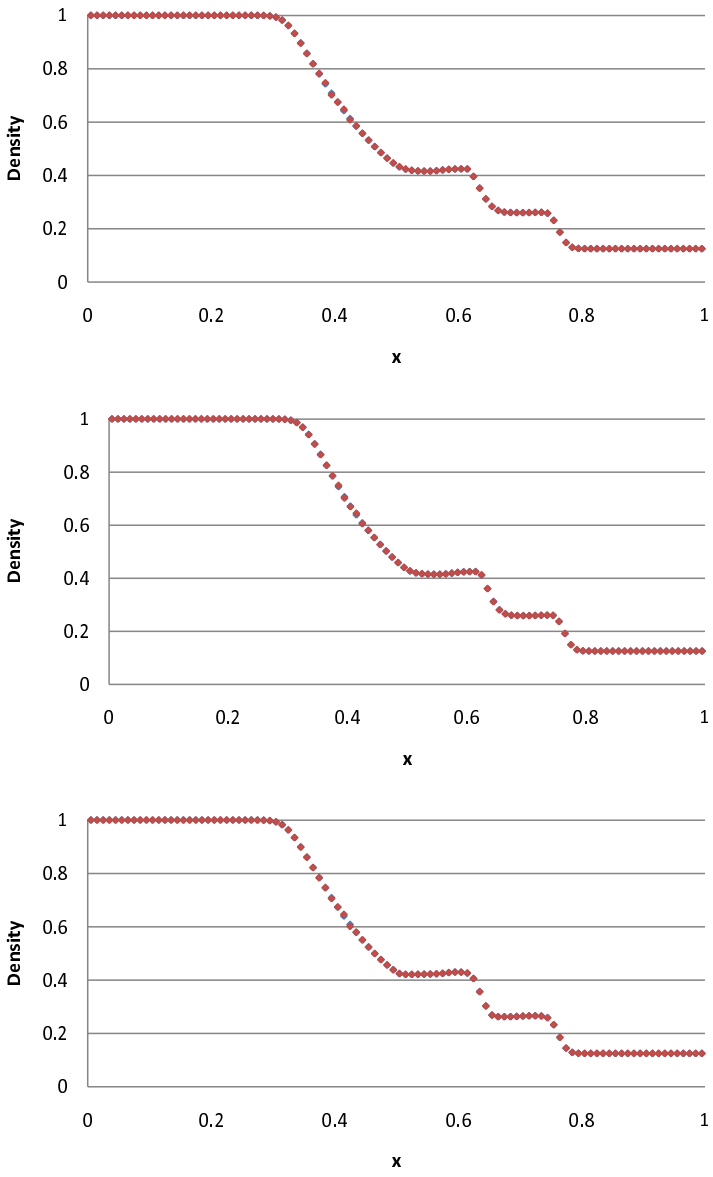

Figure 31: Artificial interface Sod's shock. Single material solutions shown in blue, artificial interface solutions shown in red. Top, van Leer; centre, MPDATA; bottom, MPDATA gauge.

All schemes show a kink in the density profile, which is expected due to the treatment of the artificial interface in the Lagrangian phase. The equal volumetric strain pressure relaxation method employed in the simulation is known to introduce some error in the Lagrangian phase, cf. Barlow [2]. The Lagrangian error will in turn be interpolated back to the Eulerian grid by the remapping phase, as exposed by the solutions of the Noh problem shown in Section 5.3. The remapping treatment utilised at material interfaces should then minimise the growth of the error exhibited at the artificial interface by retaining as high an order of accuracy as possible.

Comparing the MPDATA solutions (basic and infinite gauge option), as shown in Figure 32, with the van Leer solution it can be seen that both MPDATA options give solutions closer to their corresponding single material solution. Table 4 details the L_1 errors in the remapping methods in the elements surrounding the artificial interface. The van Leer solution reduces to first-order accuracy in the elements where a second-order solution cannot be obtained. This is shown in Figure 32 by the over accumulation of density to the left of the artificial interface, and under accumulation to the right of the interface, indicating increased diffusion, and a jump in the gradient across the interface. The MPDATA solutions exhibit similar behaviour to a decreased extent, as shown by a lower error seen in Table 4. This is expected due to the smaller stencil utilised in the MPDATA calculations, so that the MPDATA solutions are not restricted, and may theoretically obtain second-order accuracy at the boundary. To highlight this behaviour, MPDATA solutions which are forced to revert to the first-order Upwind scheme at the interface are also shown in Figure 32, with Table 4 showing the expected increase is errors in the elements surrounding the interface.

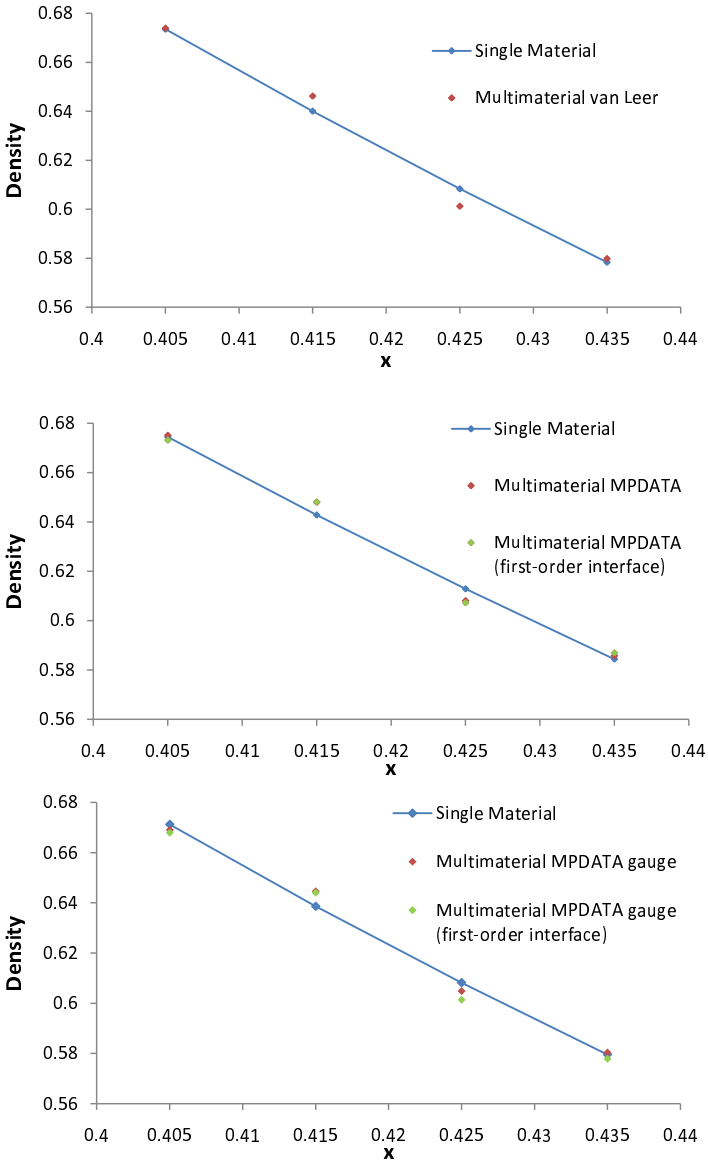

Figure 32: Magnified view of artificial interface. Top, van Leer; centre, MPDATA; bottom, MPDATA gauge. MPDATA based solutions are shown with the adaptive mixed cell approach, and the reduced accuracy approach used in the van Leer scheme.

Scheme	$x = 0.415$	$x = 0.425$
van Leer	0.00617	-0.00701
MPDATA adaptive mixed cell	0.00521	-0.00482
MPDATA first-order mixed cell	0.00528	-0.00565
MPDATA gauge adaptive mixed cell	0.00601	0.00333
MPDATA gauge first-order mixed cell	0.00551	-0.00676

Table 4: L_1 errors between the single material and artificial interface Sod's shock tube.

7.1.2 Explosion Problem with Artificial Interface

The previous test case is one-dimensional, and so does not expose complex material interface issues that are present when the cross terms in the pseudo Courant number calculation are not equal to zero. Therefore the Explosion problem, as defined in Section 5.2, is also examined with an artificial material interface defined as

$$\lambda_1 = \begin{cases} 1 & \text{if } |r| \leq 0.35, \\ 0 & \text{if } |r| > 0.35 \end{cases} \qquad \lambda_2 = \begin{cases} 0 & \text{if } |r| \leq 0.35, \\ 1 & \text{if } |r| > 0.35 \end{cases}$$

with elements intersected by the artificial material interface having $0 < \lambda_1, \lambda_2 < 1, \lambda_1 + \lambda_2 = 1$. The test is performed with a variable time step on a Cartesian computational grid with $\Delta x = \Delta y = 0.01$.

In this case, the more complex material interface situations detailed in Section 6.3.2 may be addressed. As for the one-dimensional artificial Sod's shock tube example, the deviations between artificial interface and single material solutions are relatively minor. The complete density profiles are therefore not shown. Magnified views of the artificial interface are shown in Figure 33, with density

plotted against the radius for all elements surrounding the artificial interface at $r \approx 0.255$.

It can be seen that the van Leer solution at the artificial interface results in a pronounced deviation from the single material solution which is spread over a much larger radial segment compared to the MPDATA based solutions. The non-oscillatory MPDATA solution uses the adaptive mixed cell approach detailed in Section 6.3.2, and gives a solution which appears to be closer to the single material case on the whole. A deviation from the single material solution is still visible however. The infinite gauge MPDATA solution is able to keep a profile much closer to the single material case with low errors associated with the presence of the artificial interface. The overall solution however suffers from reduced preservation of symmetry compared to the non-oscillatory MPDATA solution. The complexity of the flow arising due to a mismatch between the Cartesian grid and the radial nature of the test case is likely to amplify the errors to which the infinite gauge option will be sensitive to. In this case, synchronisation is employed within the monotonicity limits. A synchronisation approach, as detailed in [68] is employed in the solutions shown in Figure 33. The synchronisation is achieved by adding a condition such that each ξ value ((62), (63)) for energy are taken as the minimum of the energy and density ξ values in each element. MPDATA based solutions for the artificial interface employing the first-order Upwind approach at the material interface are not shown. As for the artificial interface Sod's shock test case, the first-order approach damages the solution.

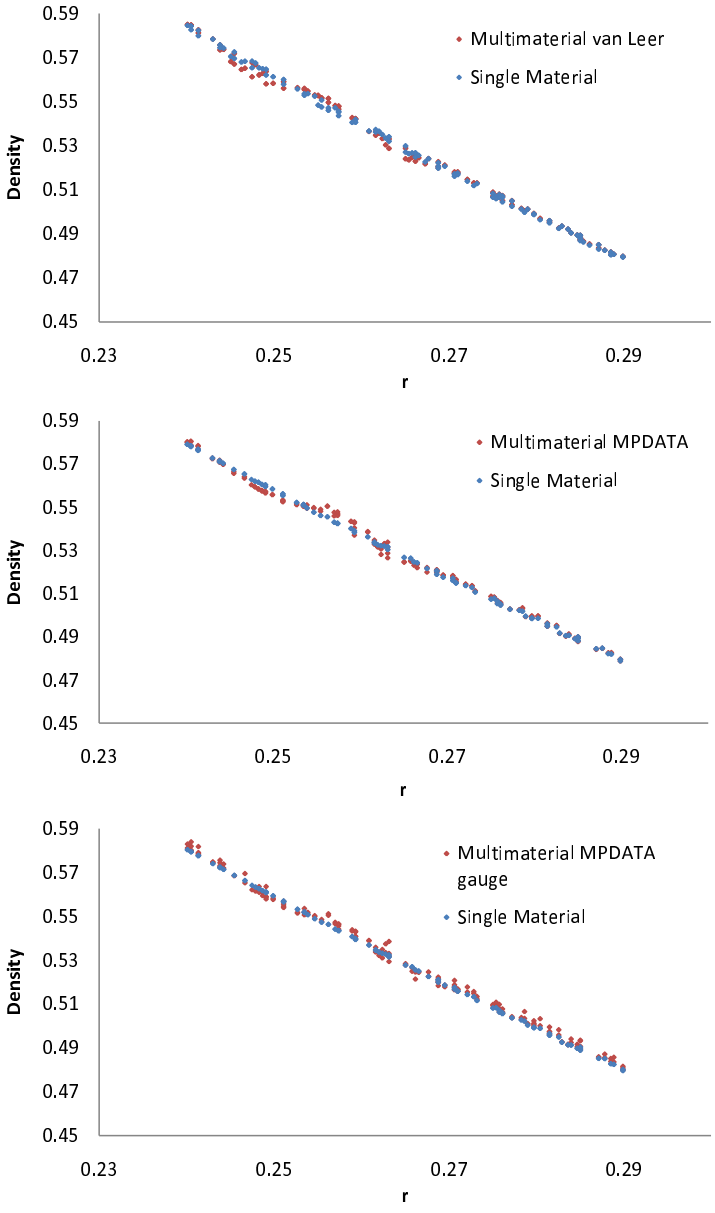

Figure 33: Magnified view of artificial interface. Top, van Leer; centre, MPDATA; bottom, MPDATA gauge. MPDATA based solutions are shown with the adaptive mixed cell approach.

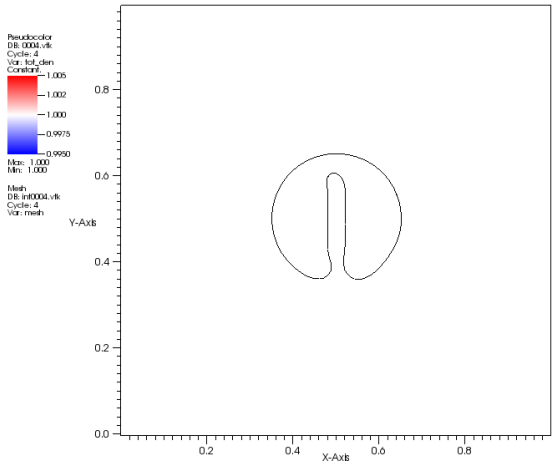

Figure 34: Distribution of ψ for the Notched circle test with Strang split van Leer remapping. Maximum value, $\psi = 1.005$, minimum value $\psi = 0.995$.

7.2 Multimaterial Remapping Test Cases

7.2.1 The Notched Circle

The notched circle test case is a two material advection problem [22, 69]. The circle with radius 0.15 is centred at $(x, y) = (0.5, 0.5)$, on a $[0, 1] \times [0, 1]$ domain. The notch is cut from the circle, passing through the centre of the circle between $y = 0.6$ and $y = 0.35$, with width 0.05 equally proportioned either side of the circle centre. The notched circle is then rotated for one revolution about the point $(x_0, y_0) = (0.5, 0.4)$ with velocity components $(u, v) = -\omega\,(y - y_0, x - x_0)$, $\omega = 0.1$. Material 1 is located inside the notched circle, and material 2 representing the background through which the circle will pass. In both materials, the scalar $\psi = 1.0$, with interface reconstruction utilised to ensure a smooth material boundary in the initial conditions so that $\lambda_1 = 1.0, \lambda_2 = 0.0$ inside the notched circle, and $\lambda_1 = 0.0, \lambda_2 = 1.0$ outside, and $0 \leq \lambda_m \leq 1$, $\lambda_1 + \lambda_2 = 1.0$ in cells intersected by the material interface. The domain is covered by 100×100 cells, with $\Delta t = 0.001$,

and final time $t = 62.8$.

The test case is primarily a test of interface reconstruction methods, and the ability of such methods to retain the initial material interface after the revolution. Only Youngs' algorithm is used in this case, with the purpose of the test being to examine the performance of the remapping schemes at material boundaries. The scalar $\psi = \lambda_1\psi_1 + \lambda_2\psi_2$ should equal unity throughout the domain. The prescribed velocity field should not create vortices or similar features that may break up the material interface, so that the material interface is expected to be identical for all remapping schemes used. See [64] for an examination of issues related to interface reconstruction, and references therein.

Figure 34 shows the material interface (solid line) and the values of the scalar ψ for the Strang split van Leer remapping after one revolution. In this case, the scalar field has a uniform distribution, with no under- or over-evaluations of the scalar values at the material interface. This result corresponds to the initial conditions, with the material boundary matching the results shown in [64]. Figure 35 shows the non-oscillatory MPDATA based remapping solutions with the adaptive mixed cell and enforced first-order approaches at the material interface. Errors in the distribution can be seen with the adaptive mixed cell approach, however such errors are insignificant (maximum 0.3 percentage error in over estimates). In cases where such errors are not tolerable, enforcing first-order accuracy at material interfaces may be used, removing such errors as shown in the bottom row of Figure 35. However, when remapping non-uniform distributions, the use of enforced first-order accuracy at material interfaces will introduce errors seen in Section 7.1.1, which may be more detrimental to the solution. Similar behaviour is seen in the infinite gauge MPDATA solutions in Figure 36. The maximum percentage error of over estimates in this case is 0.9 per cent, with the enforced first-order approach unable to remove the errors (maximum percentage

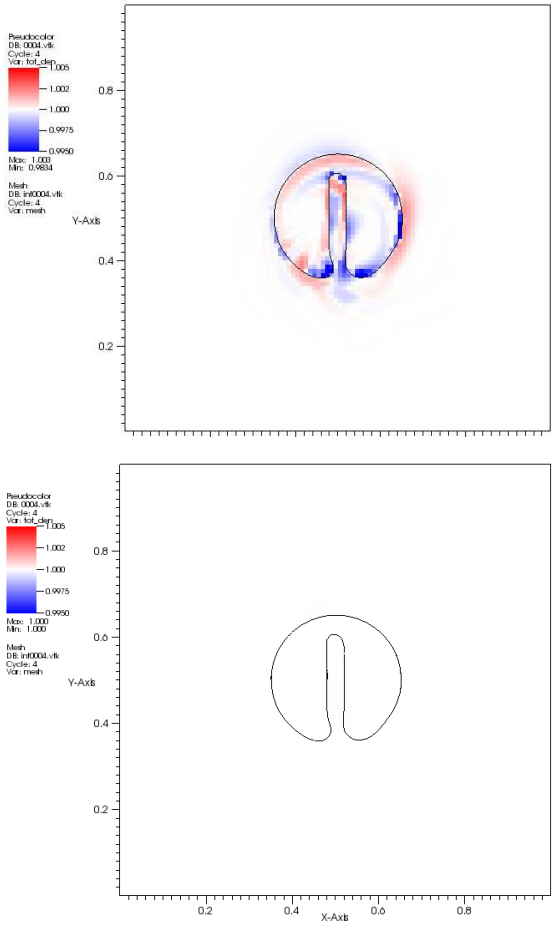

Figure 35: Distribution of ψ for the Notched circle remapping test with non-oscillatory MPDATA remapping. Top: adaptive mixed cell approach, bottom: enforced first-order approach. Maximum value, $\psi = 1.005$, minimum value $\psi = 0.995$.

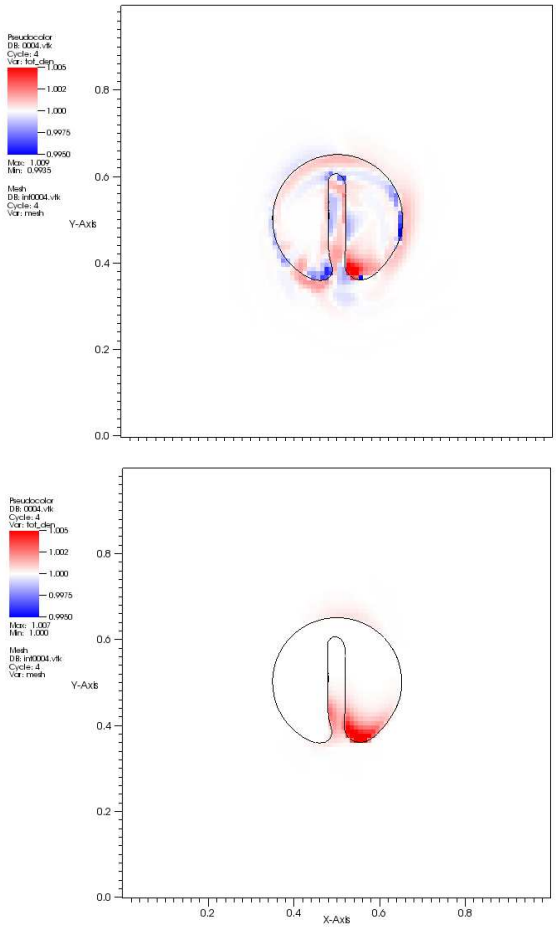

Figure 36: Distribution of ψ for the Notched circle remapping test with infinite gauge MPDATA remapping. Top: adaptive mixed cell approach, bottom: enforced first-order approach. Maximum value, $\psi = 1.005$, minimum value $\psi = 0.995$.

error of over estimates reduced to 0.7 per cent). This behaviour echoes that shown in Section 7.1.2 which shows that the infinite gauge MPDATA is more sensitive to the material interface. The minor errors introduced at the material interfaces by the MPDATA based schemes employing the adaptive mixed cell approach are also shown in [67] for schemes which aim at greater than first-order accuracy at the material interface.

7.2.2 The Vortex Problem

The Vortex problem [70, 71] is a two material advection problem designed to introduce breakup of materials due to the behaviour of the prescribed velocity field. A circle with radius 0.15 is centred at $(x, y) = (0.5, 0.75)$ on a $[0, 1] \times [0, 1]$ domain. Material 1 is located inside the circle, and material 2 outside the circle. Both materials have scalar $\psi_m = 1.0$. Interface reconstruction is used to define a smooth material interface on the computational mesh (defined by 128×128 cells) in the initial conditions such that $\lambda_1 = 1.0, \lambda_2 = 0.0$ inside the circle, and $\lambda_1 = 0.0, \lambda_2 = 1.0$ outside, and $0 \leq \lambda_m \leq 1$, $\lambda_1 + \lambda_2 = 1.0$ in cells covered by the material interface.

A vortex is defined in the velocity field with stream function

$$\vartheta = \frac{1}{\pi} sin^2 (\pi x) \, sin^2 (\pi y) \,, \tag{114}$$

with

$$u = -\frac{\partial \vartheta}{\partial y}; \qquad v = \frac{\partial \vartheta}{\partial x}. \tag{115}$$

The circle is returned to the initial state by applying a cosinusoidal time dependence to the velocity field, see [72]. In this way, with $\Delta t = 0.001$ and final time $T = 8$, the circle is stretched into a spiral as the solution approaches $t = 4$. At this time, the velocity field reduces in magnitude, before reversing and

gradually returning to the initial circle. Velocity components with cosinusoidal time dependence are given as

$$\begin{aligned} u_{i,j} &= -sin^2(\pi x_{i,j})\, sin(2\pi y_{i,j})\, cos(\pi t/T), \\ v_{i,j} &= sin^2(\pi y_{i,j})\, sin(2\pi x_{i,j})\, cos(\pi t/T). \end{aligned} \tag{116}$$

As the extent of the spiral formation develops, with the width of the spiral approaching the width of the computational cell, it is expected that the interface reconstruction algorithm will introduce a breakup of the material. In this case, the remapping scheme used, and in particular, the approach employed to deal with cells around the material interface, may affect the behaviour and amount of breakup experienced. Furthermore, as the vortex is reversed, the disjoint pieces will begin to accumulate into larger pieces, and ultimately should return to a single piece representing all of the material initially present in the circle. Again, the remapping method, and treatment of material interfaces may affect the material interface of the overall solution. As with the notched circle test case, the distribution of $\psi = \lambda_1\psi_1 + \lambda_2\psi_2$ is examined in this test case.

Figure 37 shows the solutions of the vortex test at the half period stage when the maximum extent of the spiral is attained. At this stage, breakup is exhibited as expected, however it can be seen that the MPDATA based methods do not induce breakup to the same extent as the van Leer based scheme, with the break up pieces remaining larger, and fewer in number. In this case, it is noted that the reduction in breakup is dependent upon the multidimensionality of MPDATA, with the enforced first-order material interface approach also achieving the same reduction in breakup, seen in the top row of Figure 39.

The full period results are shown in Figure 38, and in the bottom row of Figure 39. The shape of the final material interface is comparable between all methods, and agrees well with the results shown in [64] using Youngs' algorithm.

Results regarding the use of the adaptive mixed cell and enforced first order-accuracy approaches echo the Notched Circle test case, and the issues raised therein. The key result in this test case is the reduction in breakup shown by the multidimensional MPDATA approach.

7.3 Multimaterial ALE Test Cases

7.3.1 Multimaterial Sods Shock Tube

The multimaterial Sods shock tube is defined in Section 5.1, with the additional specification that

$$\lambda_1 = \begin{cases} 1.0 & \text{if } x \leq 0.5, \\ 0.0 & \text{if } x > 0.5 \end{cases}; \; \lambda_2 = \begin{cases} 0.0 & \text{if } x \leq 0.5, \\ 1.0 & \text{if } x > 0.5. \end{cases}$$

The inclusion of a material boundary is expected to replace the diffused contact discontinuity featured in the single material case, with a genuine discontinuity that arises due to the inability of the two gases to mix at the material interface.

Figure 40 shows the density profiles of the van Leer and infinite gauge MPDATA based solutions (the non-oscillatory MPDATA profile is not shown due to insignificant departures from the infinite gauge MPDATA profile). It can be seen that both approaches correctly resolve the density levels either side of the material interface, however the MPDATA based solutions feature a more consistent level of density in the elements immediately surrounding both sides of the interface. This replicates the behaviour shown in Section 5.3, in that the MPDATA retains close to second-order accuracy at the material interface, whereas the effects of dropping to first-order accuracy at the interface with the van Leer based scheme result in a slight increase of diffusion at this point.

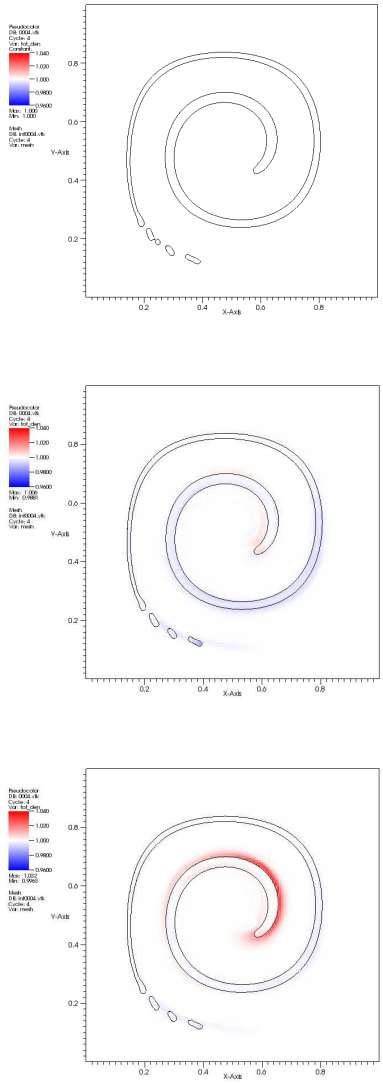

Figure 37: Distribution of ψ for the Vortex remapping test at the half period stage, $t = 4$. Top: van Leer, centre: non-oscillatory MPDATA, bottom: infinite gauge MPDATA. Both MPDATA based methods employ the adaptive mixed cell approach at material interfaces. Maximum value $\psi = 1.04$, minimum value $\psi = 0.96$.

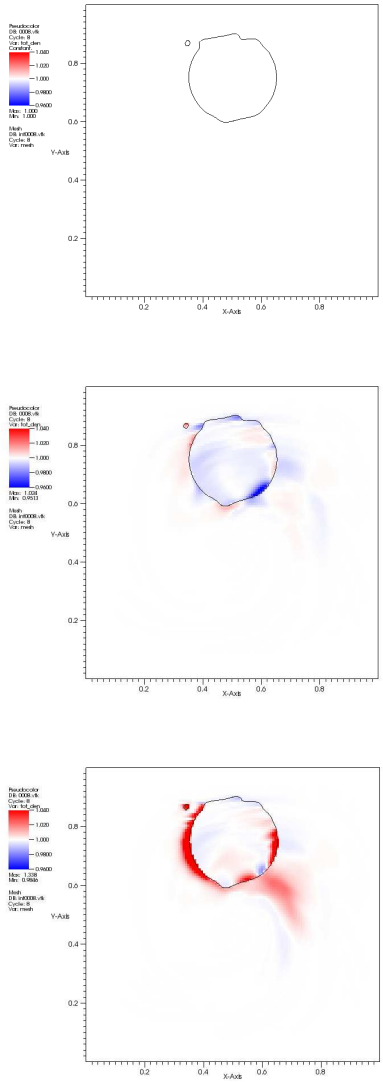

Figure 38: Distribution of ψ for the Vortex remapping test at the full period stage, $t = 8$. Top: van Leer, centre: non-oscillatory MPDATA, bottom: infinite gauge MPDATA. Both MPDATA based methods employ the adaptive mixed cell approach at material interfaces. Maximum value $\psi = 1.04$, minimum value $\psi = 0.96$.

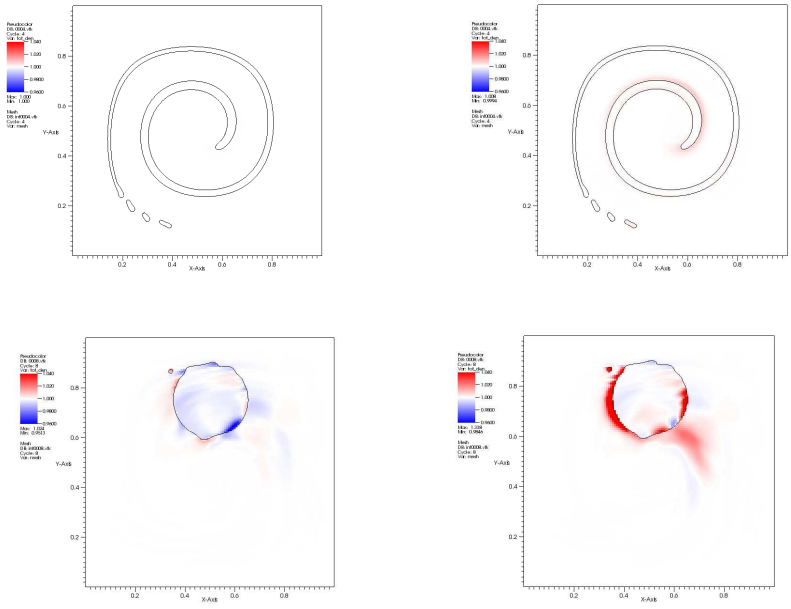

Figure 39: Distribution of ψ for the Vortex remapping test for the MPDATA based schemes employing the enforced first order accuracy approach at material interfaces. Top row: $t = 4$, bottom row: $t = 8$. Left column: non-oscillatory MPDATA, right column: infinite gauge MPDATA. Maximum value $\psi = 1.04$, minimum value $\psi = 0.96$.

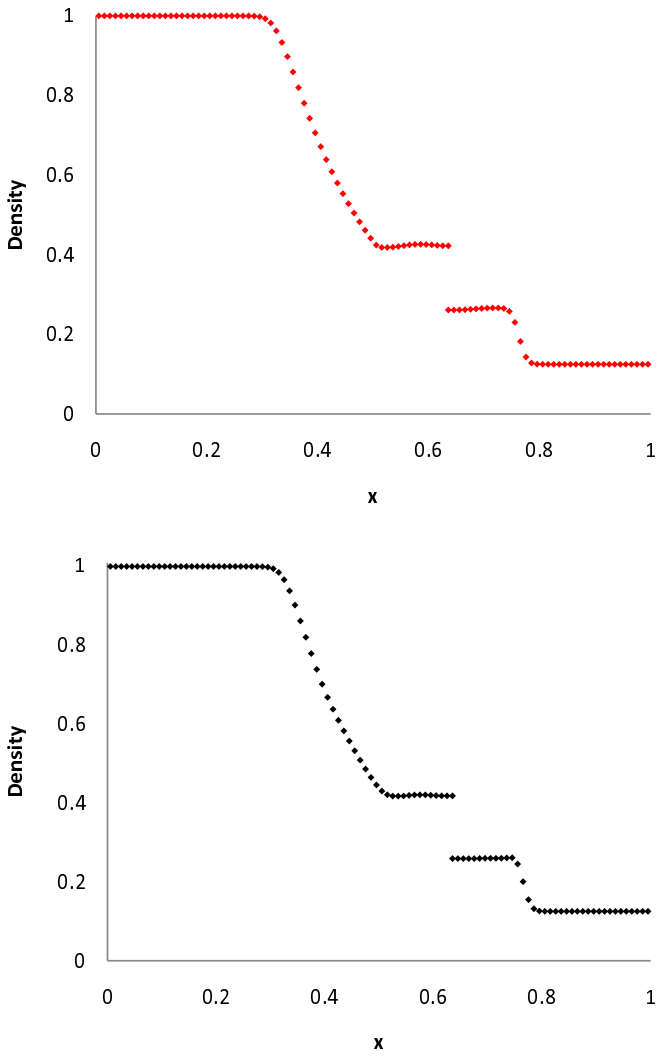

Figure 40: Density profiles of the multimaterial Sod's Shock tube. Top: van Leer, bottom: infinite gauge MPDATA.

7.3.2 Multimaterial Explosion Problem

The multimaterial Explosion problem follows the definition given in Section 5.2, with the addition of the specification of volume fractions given as

$$\lambda_1 = \begin{cases} 1 & \text{if } |r| \leq 0.4, \\ 0 & \text{if } |r| > 0.4 \end{cases} \qquad \lambda_2 = \begin{cases} 0 & \text{if } |r| \leq 0.4, \\ 1 & \text{if } |r| > 0.4, \end{cases}$$

with interface reconstruction defining a smooth material interface along $r = 0.4$, such that in cells intersected by the interface, $0 \leq \lambda_m \leq 1$ and $\lambda_1 + \lambda_2 = 1.0$.

Distributions of the material densities for both the Strang split van Leer and infinite gauge MPDATA based methods are shown in Figure 41. Both methods show good preservation of symmetry, with the van Leer scheme benefitting from the Strang split extension to multidimensions. Figure 42 replicates the conclusions of Section 7.3.1 regarding the benefit of MPDATA allowing a potentially second-order accurate solution at the material interface. The density profile either side of the material interface is much flatter in the infinite gauge MPDATA case, which matches the behaviour of the exact solution (not shown).

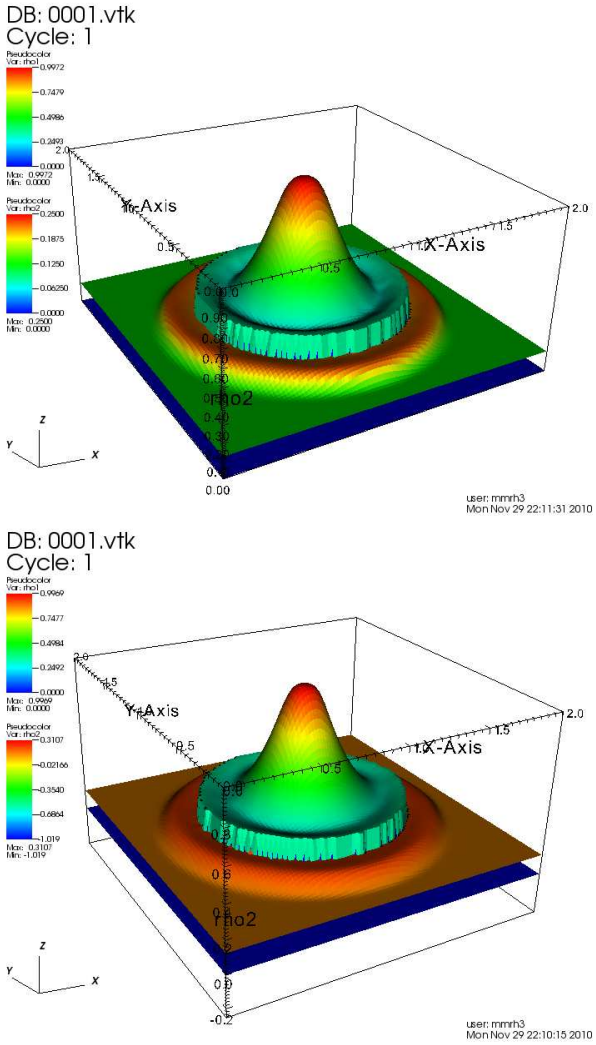

Figure 41: Material density distributions of the multimaterial Explosion problem. Top: Strang split van Leer, bottom: infinite gauge MPDATA.

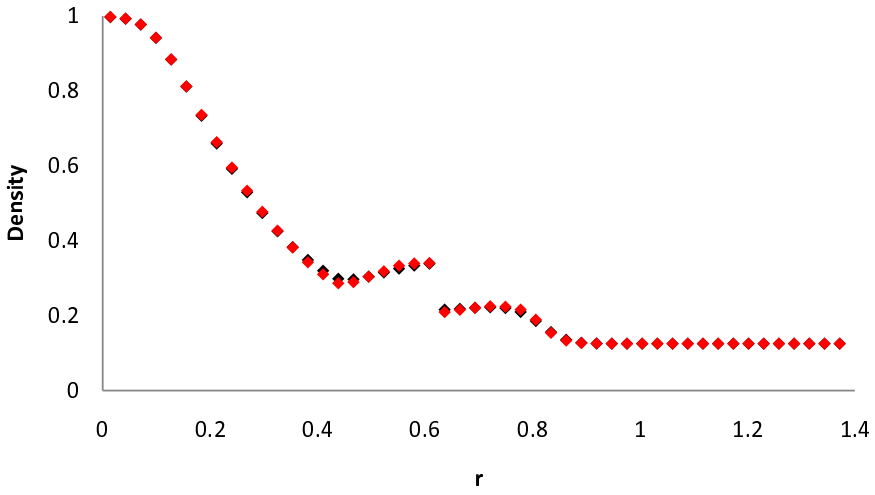

Figure 42: Density profiles of the multimaterial Explosion problem. Red: Strang split van Leer, black: infinite gauge MPDATA.

8 Conclusions

A volume co-ordinate framework has been developed for the MPDATA advection scheme which allows the MPDATA advection methods to be employed as a remapping tool within the ALE scheme. Basic non-oscillatory and non-oscillatory infinite gauge options of MPDATA have also been formulated for the volume co-ordinate framework. This work progresses initial work done at the Los Alamos National Laboratory (LANL) where a scheme based upon the underlying ideas of the basic form of MPDATA to remap a single positive scalar field was developed. However, for the first time, MPDATA has fully been used within an ALE hydrocode. The full MPDATA remapping scheme developed in this research is also non-oscillatory and applicable to numerous scalar fields of variable sign that are transported in an ALE scheme. The MPDATA remapping scheme is extended to the interpolation of both element centred and node centred variables.

Initial test cases for the MPDATA remapping scheme based upon fixed meshes agree quantitatively with the published results for advection only methods. It is seen that alterations required for volume co-ordinates - particularly in the calculation of fluxes by the swept region method - introduce additional smoothing, however such impacts are minimal and will also affect other advection schemes extended to remapping. The multidimensional properties of MPDATA are highlighted in the solid body rotation test case, with the one-dimensional van Leer scheme showing erroneous results with both the isotropic and Strang split extensions to multiple dimensions - highlighting the benefits of a truly multidimensional scheme such as MPDATA. The prescribed mesh movement test cases also show comparable results to the published methods. Again, the van Leer method produces incorrect features in the remapped scalar distributions for cases where the features do not follow the underlying geometry.

Single material ALE test cases have shown significant improvements in the preservation of symmetry with MPDATA based schemes compared to the one-dimensional van Leer based scheme in both Lagrangian-Eulerian and arbitrary Lagrangian-Eulerian modes. The Noh problem has highlighted the ability of the MPDATA based remapping to retain second-order accuracy at wall boundaries. The inherent properties of the MPDATA have been exploited to improve accuracy of solutions via both the reduced compensation and second-order filtering options.

The infinite gauge option has been shown to correctly deal with distributions containing a change in sign. This property affirms conclusions consistently made for all test cases shown such that the infinite gauge option offers greater accuracy and flexibility compared to the basic MPDATA for remapping. Conservativity of the proposed scheme is shown for both single scalar remapping and ALE calculations featuring several remapped quantities on a staggered mesh.

The multimaterial ALE tests corroborate the findings of the single material

test cases in terms of preservation of symmetry and retention of second-order accuracy at boundaries. This is particularly beneficial for remapping at material interfaces, where the reduced computational stencil utilised by the MPDATA does not force a reduction in accuracy at the boundary or interface elements. An adaptive mixed cell approach to material interface remapping is proposed such that all available data is utilised, allowing the retention of second-order accuracy and multidimensionality. Minor variations in the scalar distribution are introduced, however such errors have been shown to be insignificant compared with the values of the background distribution. The use of the adaptive mixed cell approach has been shown to improve the accuracy in values of the distribution in the region of the material interface in multimaterial test cases via the artificial interface test cases. The multidimensionality of MPDATA also improves the performance of interface reconstruction whereby the utilisation of data from more than one dimension allows turbulent flows to reduce break up of individual materials.

Further improvements may be made to the material interface treatment used by MPDATA. Here, the second-order filtering option has the potential to repair any discrepancies introduced either by the Lagrangian treatment of material interfaces, or the remapping at the interfaces. Such a property has been shown to be highly successful for domain boundaries. The issues facing remapping at domain boundaries are identical to those faced at material interfaces, however material interfaces are dynamic and move through elements as solutions progress. In this case, the level of filtering will depend upon the volume fractions associated to the material being remapped, and would need to be properly regulated to ensure stability.

A References

References

[1] D.J. Benson. Computational methods in Lagrangian and Eulerian hydrocodes, *Comp. Meth. App. Mech. Engng.*, 99, 235-394, 1992.

[2] A. Barlow. An adaptive multi-material Arbitrary Lagrangian Eulerian Algorithm for computational shock hydrodynamics. Ph.D. Thesis, University of Swansea, 2002.

[3] P.K. Smolarkiewicz and L.G. Margolin. MPDATA: A finite-difference solver for Geophysical Flows, *J. Comp. Phys.*, 140, 459-480, 1998.

[4] R. Courant, E. Isaacson, and M. Rees. On the solution of non-linear hyperbolic differential equations by finite differences, *Comm. Pure Appl. Math.*, 5, 243-255, 1952.

[5] P.K. Smolarkiewicz and J. Szmelter. MPDATA: An edge based unstructured-grid formulation, *J. Comp. Phys.*, 206, 624-649, 2005.

[6] P.K. Smolarkiewicz. Multidimensional Positive Definite Advection Transport Algorithm: An Overview, *Intl. J. Numer. Meth. Fluids*, 2006.

[7] D.J. Benson. An efficient, accurate Simple ALE method for nonlinear Finite Element Programs, *Comp. Meth. App. Mech. Engng.*, 72, 305-350, 1989.

[8] D.J. Benson. Momentum advection on unstructured staggered quadrilateral meshes, *Int. J. Numer. Meth. Engng*, 75, 1549-1580, 2008.

[9] B. van Leer. Towards the ultimate conservative difference scheme. IV. A new approach to numerical convection, *J. Comp. Phys.*, 23, 276-299, 1977.

[10] P. Collela. Multidimensional upwind methods for hyperbolic conservation laws, *J. Comp. Phys.*, 87, 171-209, 1990.

[11] W.G. Strang. On the construction and comparison of difference schemes, *SIAM J. Numer. Anal.*, 5, 506-517, 1968.

[12] P.K. Smolarkiewicz. A Simple Positive Definite Advection Scheme with Small Implicit Diffusion, *Mon. Weather Rev.*, 111, 479-486, 1983.

[13] P.K. Smolarkiewicz. A fully multidimensional positive definite advection transport algorithm with small implicit diffusion, *J. Comp. Phys.*, 54, 325-362, 1984.

[14] P.K. Smolarkiewicz and T.L. Clark. The multidimensional positive definite advection transport algorithm: Further development and applications, *J. Comp. Phys.*, 67, 396-438, 1986.

[15] L.G. Margolin and Mikhail Shashkov. Second order sign preserving remapping on general grids, Technical Report LA-UR-02-525, Los Alamos National Laboratory.

[16] L.G. Margolin and Mikhail Shashkov. Second-order sign-preserving conservative interpolation (remapping) on general grids. *J. Comp. Phys.*, 184, 266-298, 2003.

[17] L.G. Margolin and P.K. Smolarkiewicz. Anitdiffusive velocities for multipass donor cell advection, Technical Report, Lawrence Livermore National Laboratory, 1989.

[18] R.N. Hill and J. Szmelter. A multidimensional positive definite remapping algorithm for arbitrary LagrangianEulerian methods, *Int. J. Numer. Meth. Fluids*, in press, DOI: 10.1002/fld.2351.

[19] J.P. Boris and D.L. Book. Flux Corrected Transport I: SHASTA, a fluid transport algorithm that works, *J. Comp. Phys.*, 11, 38-69, 1973.

[20] J.P. Boris and D.L. Book. Flux Corrected Transport II: Generalisation of the method, *J. Comp. Phys.*, 18, 248-283, 1974.

[21] J.P. Boris and D.L. Book. Flux Corrected Transport III: Minimal Error FCT Methods, *J. Comp. Phys.*, 20, 397-431, 1976.

[22] S. Zalesak. A Fully Multidimensional flux-corrected transport algorithm for fluids, *J. Comp. Phys.*, 31, 335-362, 1979.

[23] P.K. Smolarkiewicz and W.W. Grabowski. The Multidimensional Positive Definite Advection Transport Algorithm: Nonoscillatory Option, *J. Comp. Phys.*, 86, 355-375, 1990.

[24] R.N. Hill and J. Szmelter. A multidimensional positive definite remapping for Lagrangian solutions of the Noh problem. *Comp. Fluids*, in press, doi:10.1016/j.compfluid.2010.09.007.

[25] P.K. Smolarkiewicz and J. Szmelter. Iterated upwind Schemes for Gas Dynamics, *J. Comp. Phys.*, 228, 33–54, 2009.

[26] L.G. Margolin, P.K. Smolarkiewicz. Antidiffusive velocities for multipass donor cell advection, *J. Sci. Comput.*, 20, 907-929, 1998.

[27] P.K. Smolarkiewicz, L.G. Margolin. MPDATA: a finite difference solver for geophysical flows, *J. Comput. Phys.*, 140, 459- 480, 1998.

[28] L.J. Hageman, D.E. Wilkins, R.T. Sedgewick and J.L. Waddell. HELP, a multimaterial Eulerian program for compressible fluid and elastic-plastic flows in two space dimensions and time, *System, Science and Software*, 1975

[29] W.G. Sutcliffe. BBC Hydrodynamics, Lawrence Livermore National Laboratory, UCIR-716, 1973.

[30] R.D. Krieg and S.W. Key. Implementation of a time dependent plasticity theory into structural programs, *Comp. and Engng. Aspects*, 20, 125-137, 1976.

[31] W.F. Noh. CEL: A time-dependent two-dimensional coupled Eulerian-Lagrange code, *Methods in Comp. Phys.*, 3, 117-179, 1964

[32] R. Couch, E. Albright and N. Alexander. The JOY computer code, Technical Report UCID-19688, Lawrence Livermore National Laboratory, 1983.

[33] S. Hancock. PISCES 2DELK Theoretical Manual, *Phys. Intl.*, 1985

[34] S.L. Thompson. CSQ - A two dimensional hydrodynamic program with energy flow and material strength, Sandia Laboratories, SAND74-0122, 1975.

[35] J.M. McGlaun, S.L. Thompson and M.G. Elrick. CTH: A three dimensional shock wave physics code, *Hypervelocity Impact Symp.*, 1989.

[36] K.S. Holian, D.A. Mandell, T.F. Adams, F.L. Adessio, J.R. Baumgardner and S.J. Mosso. MESA: A 3D computer code for armor/anti-armor applications, *Proc. Supercomputing World Conference*, 1989.

[37] R.B. DeBar. Fundamentals of the KRAKEN code, Lawrence Livermore Laboratory, UCIR-760, 1974.

[38] A.A. Amsden and C.W. Hirt. YAQUI: An Arbitrary Lagrangian-Eulerian computer program for fluid flow at all speeds, Technical Report LA-5100, Los Alamos National Laboratory, 1973.

[39] C.W. Hirt, A.A. Ammsden and J.L. Cook. An Arbitrary Lagrangian-Eulerian computing method for all flow speeds, *J. Comp. Phys.*, 14, 227-253, 1974.

[40] A.A. Amsden, H.M. Ruppel and C.W. Hirt. SALE: A Simplified ALE computer code for fluid flow at all speeds, Technical Report, Los Alamos National Laboratory, 1980.

[41] A.A. Amsden and H.M. Ruppel. SALE-3D: A Simplified ALE computer code for calculating three dimensional fluid flow, Technical Report, Los Alamos National Laboratory, 1981.

[42] R.W. Sharp and R.T. Barton. HEMP advection model, Technical Report UCID-17809, Lawrence Livermore National Laboratory, 1981.

[43] R.B. Demuth, L.G. Margolin, B.D. Nichols, T.F. Adams and B.W. Smith. SHALE: A computer code for solid dynamics, Technical Report, Los Alamos National Laboratory, 1985.

[44] F.L. Addessio, D.E. Carroll, J.K. Dukowicz, F.H. Harlow, J.N. Johnson, B.A. Kaskiwa, M.E. Maltrud and H.M. Ruppel. CAVEAT: A computer code for fluid dynamics problems with large distortion and internal slip, Technical Report, Los Alamos National Laboratory, 1988.

[45] A. J. Barlow, A compatible finite element multi-material ALE hydrodynamics algorithm, *Int. J. Numer. Meth. Fluids*, 56, 953-964, 2008.

[46] J. von Neumann and R.D. Richtmeyer. A method for the numerical calculations of Hydrodynamical Shocks, *J. App. Phys.*, 21, 1950.

[47] A.M. Winslow, Equipotential zoning of two-dimensional meshes, Lawrence Radiation Laboratory, UCRL-7312, 1963.

[48] G.A. Sod. A survey of Several Different Methods for Systems of Nonlinear Hyperbolic Conservation Laws, *J. Comp. Phys.*, 27, 1-31, 1978.

[49] E.F. Toro. Riemann Solvers and Numerical Methods for Fluid Dynamics, ISBN 3-540-65966-8.

[50] R. Liska and B. Wendroff. Comparison of Several Difference Schemes on 1D and 2D Test Problems for the Euler Equations, *SIAM Journal on Scientific Computing*, 25 (3), 2003.

[51] W.F. Noh. Errors for calculations of strong shocks using artificial viscosity and an artificial heat flux, *J. Comp. Phys.*, 72, 78-120, 1987.

[52] W.J. Rider. Revisiting Wall heating, *J. Comp. Phys.* 162, 395-410, 2000.

[53] Szmelter J, Smolarkiewicz PK. MPDATA Error Estimator for Mesh Adaptivity. *Int. J. Numer. Meth. Fluids* 2006; **50**:1269–1293.

[54] R.B. Christensen. Godunov methods on a staggered mesh - an improved artificial viscosity, Technical Report UCRL-JC-105269, Lawrence Livermore National Laboratory, 1990.

[55] J.M. Hyman. Numerical methods for tracking interfaces, *Physica D.*, 12, 396-407, 1984.

[56] E.S. Oran and J.P. Boris. Numerical simulation of reactive flow, Elsevier, New York, 1987.

[57] C.W. Hirt and B.D. Nichols. Volume of Fluid (VOF) method for the dynamics of free boundaries, *J. Comp. Phys.*, 39, 201-225, 1981.

[58] W.F. Noh and P. Woodward. SLIC (Simple Line Interface Calculation), *Lecture Notes in Physics*, 59, 1976.

[59] W.F. Noh and P. Woodward. SLIC (Simple Line Interface Calculation), Technical Report UCRL-52111, Lawrence Livermore National Laboratory, 1976.

[60] D. Youngs. Numerical Methods for Fluid Dynamics, chapter - Time dependent multi-material flow with large fluid distortion, pages 273-285. Academic Press, 1982.

[61] D. Youngs. An Interface Tracking Method for a 3D Eulerian Hydrodynamics Code. Technical Report AWRE/44/92/35, Atomic Weapons Research Establishment, 1987.

[62] V. Dyadechko and M. Shashkov. Reconstruction of Multi-material Interfaces from Moment Data. *J. Comput. Phys.*, 2008, doi:10.1016/j.jcp.2007.12.029.

[63] V. Dyadechko and M. Shashkov. Moment-of-Fluid Interface Reconstruction, LA-UR-05-7571, LANL Report.

[64] R. Kevis, Non-linear MHD simulations of Solar Coronal structures. Ph.D. Thesis, University of St Andrews, 2005.

[65] H. Ahn, M. Shashkov. Multi-material Interface Reconstruction on Generalized Polyhedral Meshes, LANL Report, LA-UR-07-0656.

[66] H. Ahn, M. Shashkov and M.A. Christon. The Moment-of-Fluid Method in Action , LA-UR-07-6854, Los Alamos National Laboratory, 2007.

[67] W.J. Rider, E. Strack, M. Wong, S. Petney, D. Labreche. An Adaptive Multimaterial Remap Method with Awareness of the Material Interface, in conference proceedings Multimat09, Pavia, Italy, Sept. 2009

[68] C. Schar, P.K. Smolarkiewicz. A Synchronous and Iterative Flux-Correction Formalism for Coupled Transport Equations, *J. Comput. Phys.*, 128, 101-120, 1996.

[69] J. Pilliod and E. Puckett. Second-Order Accurate Volume-of-Fluid Algorithms for Tracking Material Interfaces, *J. Comput. Phys*, 199, 465-502, 1999.

[70] W. Rider and D. Kothe. Stretching and Tearing Interface Tracking Methods. In The 12th AIAA CFD Conference, San Diego, June 20, 1995, AIAA-95-1717.

[71] W. Rider and D. Kothe. Reconstructing Volume Tracking. *J. Comput. Phys*, 141, 112-152, 1998.

[72] R.J. LeVeque, Numerical Methods for Conservation Laws, *Birkhuser Verlag*, p214, 1992.